

**UNIVERSITY OF SOUTHAMPTON**

**Applications of Microfluidics in Nuclear  
Magnetic Resonance**

by

William G Hale

A thesis submitted in partial fulfillment for the  
degree of Doctor of Philosophy

in the  
Faculty of Engineering and Physical Sciences  
School of Chemistry

16/06/2019

UNIVERSITY OF SOUTHAMPTON

ABSTRACT

FACULTY OF ENGINEERING AND PHYSICAL SCIENCES  
SCHOOL OF CHEMISTRY

Doctor of Philosophy

by William G Hale

Microfluidics is a constantly growing field of research, finding applications in a diverse range of subjects such as materials science, chemistry and across the life sciences. This expansion is due to many advantageous attributes: small sample volumes which contribute to waste reduction and reduced cost of experimentation; highly controllable local environments that enable very precise investigation of changes in systems to stimuli; rapid prototyping techniques that mean make, test, tweak cycles can be run more than once in a typical day; ease of parallelisation makes gathering statistically significant data much easier without the need to repeat experiments for days at a time; and ease of automation increases precision and repeatability.

Nuclear magnetic resonance (NMR) spectroscopy is a widely applied technique in chemistry and the life sciences. Its non-invasive and non-destructive nature makes NMR ideal to study living, or mass limited samples. NMR, however, requires an extremely homogenous magnetic field to enable molecular structure determination and can be limited by the inherent low sensitivities possible in a typical experiment.

This thesis describes methods for integrating these two fields. Some NMR experiments being ‘miniaturised’ to be performed ‘on-chip’ as well as microfluidic concepts that have been engineered to be compatible with NMR techniques. These techniques do not seek to replace established methods of microfluidic analysis such as mass spectrometry or fluorescence spectroscopy but could be used to compliment these techniques as an additional method of extracting data from a system.

# Contents

<b>Nomenclature</b>	<b>vi</b>
<b>Acknowledgements</b>	<b>ix</b>
<b>1 Introduction</b>	<b>1</b>
<b>2 Background</b>	<b>3</b>
2.1 Microfluidics . . . . .	3
2.1.1 History to present day . . . . .	3
2.2 Quantum Theory of Nuclear Magnetic Resonance . . . . .	12
2.2.1 Nuclear Spin . . . . .	12
2.2.2 Spin Systems . . . . .	13
2.2.3 Pauli matrices and more operators . . . . .	15
2.2.4 Density Operator . . . . .	18
2.2.5 The Hamiltonian . . . . .	20
2.2.5.1 Spins in a magnetic field . . . . .	21
2.2.6 Spin precession . . . . .	23
2.2.7 Rotating Frame . . . . .	24
2.2.7.1 Precession in the rotating frame . . . . .	24
2.2.8 Radio Frequency Pulses . . . . .	25
2.2.8.1 $x$ -pulse . . . . .	26
2.2.8.2 Pulse of general phase . . . . .	27
2.2.8.3 Off-resonance effects . . . . .	28
2.2.9 The Density operator revisited . . . . .	29
2.2.9.1 Magnetization vector . . . . .	30
2.2.9.2 Density operator under pulses . . . . .	31
2.2.10 Free evolution with relaxation . . . . .	32
2.2.10.1 Transverse relaxation . . . . .	32
2.2.10.2 Longitudinal relaxation . . . . .	34
2.2.11 NMR signal and detection . . . . .	34
2.2.11.1 Quadrature detection . . . . .	36
2.2.11.2 Signal after a pulse . . . . .	38
2.2.11.3 Chemical Shift and J-coupling . . . . .	39
2.3 Micro-NMR . . . . .	41
2.3.1 Sensitivity . . . . .	41
2.3.1.1 Signal to noise ratio . . . . .	41
2.3.2 Signal Averaging . . . . .	43

2.3.3	Limit of Detection . . . . .	45
2.3.4	Concentration limit of detection . . . . .	45
2.3.5	Transmission line probe . . . . .	46
<b>3</b>	<b>Microfluidic Droplet NMR</b>	<b>49</b>
3.1	Synopsis . . . . .	49
3.2	Introduction . . . . .	49
3.2.1	Susceptibility . . . . .	51
3.2.2	Matching susceptibilities . . . . .	53
3.3	Materials and Methods . . . . .	56
3.4	Results and Discussion . . . . .	58
3.5	Conclusion . . . . .	64
<b>4</b>	<b>Parahydrogen induced polarization on a chip</b>	<b>66</b>
4.1	Synopsis . . . . .	66
4.2	Introduction . . . . .	67
4.3	Hyperpolarization . . . . .	69
4.3.1	Sensitivity . . . . .	69
4.3.2	Hyperpolarization . . . . .	69
4.3.3	Techniques . . . . .	70
4.3.3.1	Brute Force . . . . .	70
4.3.3.2	Dynamic Nuclear polarization . . . . .	70
4.4	Parahydrogen Induced polarization - PHIP . . . . .	71
4.4.1	Parahydrogen . . . . .	71
4.4.2	PASADENA and ALTADENA . . . . .	74
4.4.2.1	Spin Physics . . . . .	75
4.5	Materials and methods . . . . .	79
4.6	Results and Discussion . . . . .	81
4.6.1	Parahydrogen relaxation in PDMS . . . . .	81
4.6.2	Reaction Scheme . . . . .	82
4.6.3	ALTADENA . . . . .	82
4.6.4	PASADENA . . . . .	84
4.6.5	Signal Analysis . . . . .	86
4.6.6	Hydrogen Transport . . . . .	88
4.6.7	Sensitivity and Limit of Detection . . . . .	89
4.6.8	2D NMR . . . . .	93
4.7	Conclusions . . . . .	96
<b>5</b>	<b>An NMR compatible on-chip Peristaltic Pump</b>	<b>98</b>
5.1	Introduction . . . . .	98
5.1.1	Materials and Methods . . . . .	105
5.2	Results and Discussion . . . . .	107
5.2.1	Characterisation of flow . . . . .	107
5.2.2	<i>In situ</i> operation of the device . . . . .	108
5.3	Conclusions . . . . .	110
<b>6</b>	<b>Conclusions</b>	<b>111</b>

<b>A Appendix</b>	<b>113</b>
A.1 2D Pulse sequences for PH-TOCSY and PH-HMQC . . . . .	113
A.2 Arduino Firmware . . . . .	113

## Abbreviations

Acronym	Definition
cLOD	Concentration Limit of Detection
dDNP	dissolution Dynamic Nuclear Polarization
DNP	Dynamic Nuclear Polarization
DTPA	Diethylenetriaminepentaacetic Acid
EMF	Electromotive Force
FCC	Face-Centred Cubic
FID	Free Induction Decay
HMQC	Heteronuclear Multiple Quantum Coherence
LIF	Laser Induced Fluorescence
LoC	Lab-on-a-chip
MAS	Magic Angle Spinning
MR	Magnetic Resonance
MRI	Magnetic Resonance Imaging
nLOD	Mass Limit of Detection
NMR	Nuclear Magnetic Resonance
OTC	Oxytetracycline
PDMS	Poly(dimethylsiloxane)
PHIP	Parahydrogen Induced Polarization
PMMA	Poly(methylmethacrylate)
ppm	Parts Per Million
PTFE	PolyTetraFluoroEthylene
r.f.	Radio Frequency
RF	Radio Frequency
RMS	Root Mean Square
SABRE	Signal Enhancement By Reversible Exchange
SNR	Signal to Noise Ratio
SPR	Surface Plasmon Resonance
TLP	Transmission Line Probe
TOCSY	Total Correlation Spectroscopy
UV-light	Ultraviolet-light
2D	Two Dimensional
3D	Three Dimensional
µTAS	Micro Total Analysis System

# Nomenclature

$a$	The signal amplitude
$\mathbb{B}$	The Boltzmann factor
$B_0$	The external magnetic field
$B_1$	The magnetic field produced by an NMR coil
$c_s$	The concentration of spins in a sample
$C$	A constant in SNR
$d$	The coil diameter
$F$	The noise factor from the spectrometer
$\mathbf{H}$	The magnetic field
$h$	Planck's constant
$\hbar$	The reduced Planck constant
$\hat{H}$	The Hamiltonian operator in natural units
$I$	The spin quantum number
$\hat{I}$	The spin angular momentum operator
$i_c$	The current
$J$	The rotational quantum number
$k_0$	A constant that accounts for spatial inhomogeneities in the $B_1$ field
$k_B$	The Boltzmann constant
$l$	The length of a coil
$M_0$	The net magnetisation
$M_a$	The magnetisation vector component along the $a$ -axis
$\mathbf{M}$	The magnetisation
$n_s$	The number of spins in a sample
$\check{\mathbf{n}}$	The surface normal
$p$	The polarisation of a spin system
$P_\alpha$	The population of the $\alpha$ state
$R_{\text{noise}}$	The dissipative loses
$\hat{R}$	The rotation operator
$S(t)$	The signal in the time domain
$S(\Omega)$	The signal in the frequency domain
$T$	The absolute temperature
$T_s$	the singlet relaxation time constant

---

$T_1$	The longitudinal relaxation time constant
$T_2$	The transverse relaxation time constant
$U$	The scalar magnetic potential
$V_s$	The sample volume
$V'_s$	The product of $k_0$ and $V_s$ that is the volume is within 10% of maximum
$\mathbb{1}$	The identity matrix
$\alpha_F$	The filling factor
$\beta_p$	The tilt of the roatation axis from $z$ for an off-resonance pulse
$\gamma_j$	The gyromagnetic ratio for a nucleus, $j$
$\delta$	The chemical shift
$\delta_{\text{RF}}$	The RF current penetration depth
$\Delta f$	The spectral bandwidth
$\epsilon$	The enhancement factor
$\theta$	The tilt angle of magentisation
$\theta_{\text{RF}}$	The angle between the r.f. coil and $B_0$
$\lambda_l$	The decay constant of a spin $l$
$\mu$	The reduced mass
$\mu_0$	The vacuum permeability
$\hat{\mu}$	The magnetic dipole moment operator
$\xi$	The emf
$\rho_r$	The resistivity
$\hat{\rho}$	The density operator
$\sigma$	The chemical shielding factor
$\phi_p$	The phase of an r.f. pulse
$\phi_{\text{ref}}$	The phase shift in the rotating frame
$\Phi$	The angle that connects the static to rotating frame
$\chi_V$	The Magnetic susceptibility
$\omega_j^0$	The larmour frequency for a nucleus, $j$
$\omega_{\text{nut}}$	The nutation frequency
$\omega_{\text{ref}}$	The rotating frame frequency
$\Omega^0$	The and rotating frame frequency offset

**Declaration of Authorship**

This thesis is the result of work done wholly while I was in registered candidature for a Ph.D. degree at the University of Southampton. The material presented here is based on work mostly done by myself. Where the work was carried out jointly with others, a substantial part is my own original work and co-workers and their roles have been clearly indicated. The material contained herein has not been submitted by the author for a degree at any other institution.

Signed: 16/06/2019

## Acknowledgements

I would like to express my deep gratitude to Professor Marcel Utz for providing patient guidance and enthusiastic encouragement, as well as engaging discussion concerning all matters of life and work. His depth of knowledge in all manner of subjects was a great help throughout my PhD and provided a seemingly endless source of ideas and problem solving. The principles of scientific investigation I have learnt from him will stay with me throughout my career.

I wish to thank Professor Malcolm Levitt for his support and guidance, the discussions we have had about science helped me to see problems in a different light and increased my effectiveness as a scientist.

I am grateful to my colleagues who have helped me enormously throughout my time in Southampton in no particular order I wish to thank: James Eills, Graeme Finch, Rachel Greenhalgh, Benno Meir, Javier Alonso-Valdesueiro, Karel Kouril, Hana Kourilova, Aliko Moysiadi, Stuart Elliot, Christian Bengs, Manvendra Sharma, Bishnubatra Partra, Matheus Rossetto, Gabriel Rossetto, Marek Plata, Sylwia Ostrowska, Weidong Gong, Mohammed Sabba, George Bacanu, Laurynas Dagys, Jo Collel and Barbara Ripka.

To the people that provided support and encouragement throughout my work and helped me keep sane, I am indebted to Frankie Leeming, Thomas Kear, Laura Jowett, James Eills, Stuart Elliot, Christian Bengs, Aliko Moysiadi, Nic Charles, Judy Fox, Josie Charles, Gemma Charles and Eddie Robinson you all helped immensely.

In particular I'd like to thank Alyssa Charles for her unwavering support, encouragement, and belief in me, as well as proof reading and correcting my grammar errors.

Finally, I'd like to thank my family for all their support over the years, this is only possible because of them.

*To my friends and family*

# Chapter 1

## Introduction

Microfluidics is a broad term that covers a wide variety of research, it is characterised by the analysis of small volumes of liquids usually nL to  $\mu$ L, in doing so, it offers numerous benefits such as: a reduction in the materials used in experiments leading to lower costs and less waste; a high level of control over the microenvironment; and ease of parallelisation and automation. Microfluidics chiefly uses Lab-on-a-chip (LoC) devices, or micro total analysis systems ( $\mu$ TAS), to perform experiments. These devices, or systems, are intended for the scaling down of laboratory functions to a chip-format, the sizes of which range from a few mm<sup>2</sup> to a few cm<sup>2</sup>. Currently, NMR spectroscopy is not widely utilised in microfluidic devices, or experiments, and could be used to provide extra information on the system of interest. Its non-invasive, non-destructive nature means that it can also be used in conjunction with existing methods of analysis in microfluidics such as fluorescence spectroscopy. As NMR leaves the sample unperturbed, this makes it an ideal candidate for *in situ* monitoring of living systems.

The goal of the work presented here is to incorporate functional microfluidic experiments with high resolution NMR spectroscopy, in such a way that the validity of either technique, microfluidic or magnetic resonance, remains intact. In this approach, microfluidic capability is preserved by utilising a design that, whilst constrained by size and shape, has freedom to house a wide variety of chip designs which enable a host of applications, a few of these are shown in Fig. 1.1. This means that functional microfluidics can be performed, and coupled, with high resolution NMR spectroscopy. In doing so, not only could NMR become a more widely used tool in the microfluidic toolbox, it would also make a valuable attachment to existing tools.

High resolution NMR spectroscopy itself requires an extremely homogenous magnetic field, this means that any device capable of combining microfluidics and NMR should seek to preserve the homogeneity. This combination however, is not without significant challenges. Firstly, a probe capable of  $\mu$ NMR must be designed with comparable performance to existing probes, to maintain validity, and work with existing magnets

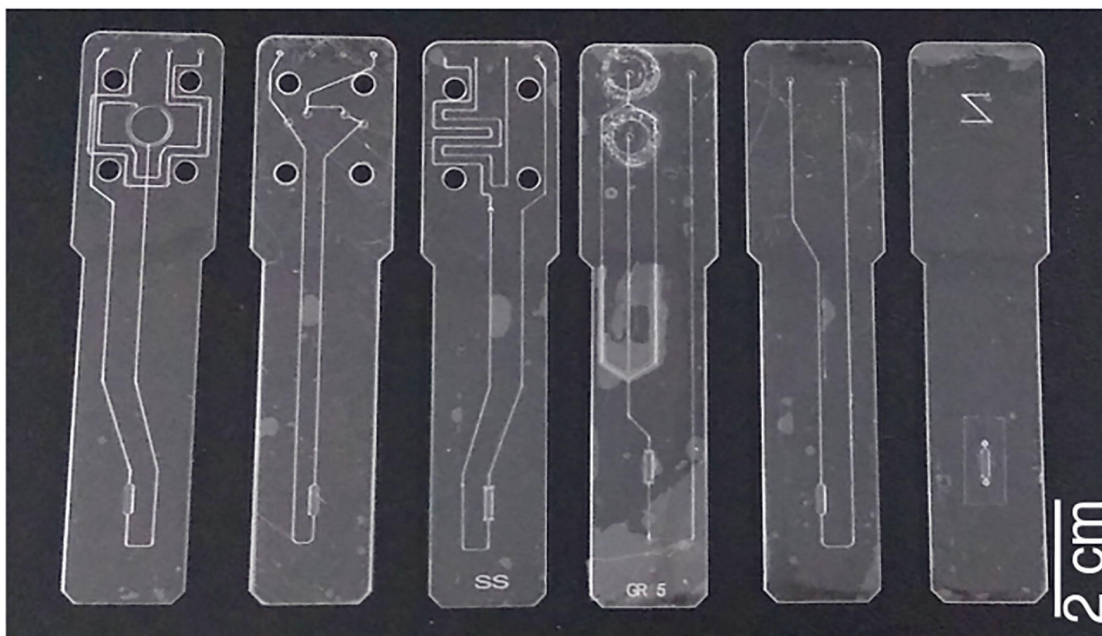


FIGURE 1.1: Microfluidic devices developed for this work, as well as for other applications in microfluidic NMR. From the left: A device for perfusion culture of a tissue slice on chip; capable of peristaltic pumping; hydrogenation on a chip; droplet generation; simple sample chamber filler; 2D/3D cell culture device. Figure taken from [1].

and spectrometers. Secondly, the chip, and any functionality it possesses, must fit in the bore of the magnet which is typically around 38 mm in diameter. This chip should also couple to the probe in a removable way to enable parallelisation of experiments, preserving one of the key attributes of microfluidics. Thirdly, the materials used in construction should be non-magnetic wherever possible and the use of magnetic parts should be kept to a minimum. When designing experiments, the magnetic susceptibilities of solutions and chip material should also be considered, as these need to be as closely matched as possible in order to preserve spectral resolution (a solution for when this is not the case is discussed in chapter 3).

By combining these two fields, and harnessing the 'best of both worlds' approach, new insight and analysis is available. Having quantitative, system-level information, in a single or just a few scans could benefit a wide variety of experiments. Enabling microfluidic NMR also provides the opportunity to scan mass-limited samples, such as those commonly found in ligand binding reactions [2] or macrocyclic chemistry [3].

# Chapter 2

## Background

### 2.1 Microfluidics

#### 2.1.1 History to present day

The first analytical miniaturised device fabricated on silicon was presented in 1979 by Terry *et al* [4]. This device, was a gas chromatograph capable of separating a simple mixture of gases in seconds, and included an injection valve and a 1.5 m long separation column. A thermal conductivity detector was fabricated separately, and clamped to the silicon wafer containing the column. This subsequently allowed for a reduction in size of the chromatograph of nearly 3 orders of magnitude compared to the conventional lab equipment at the time, and is regarded as the first demonstration of the power of miniaturisation from which, the field of lab-on-a-chip and microfluidics would be born [5]. Into the 1980s, research related to miniaturisation focused on the fabrication of components, like micropumps [6, 7], and microvalves [8] rather than silicon based analysers.

In 1990, work describing a miniaturised liquid chromatograph on a silicon wafer was published [9]. This work described a 5 x 5 mm chip containing a column and detector that was connected to an off-chip HPLC pump and valves, enabling it to perform high pressure liquid chromatography. Concurrently, the concept of a 'miniaturised total analysis system' ( $\mu$ TAS) was introduced by Manz *et al* [10], where the incorporation of sample pretreatment, separation, and detection onto a single device was proposed to enhance the analytical performance of the device, rather than simply reduce its size. However, it was also recognised that miniaturisation of the device presented the advantage of not only a smaller consumption of materials, but would also enable the integration of multiple separation techniques capable of monitoring many components in a single device.

Such a device was envisioned as capable of sample handling, analysis, detection, and incorporating control of mass transport. Conventional pumps at the time struggled with the high pressures needed for transport in small channels, and early theoretical considerations showed that electroosmotic pumping was an attractive and feasible way to move aqueous liquid through a  $\mu$ TAS, especially when separation was needed.

Electroosmosis is defined as the motion of liquid induced by an applied potential. An electroosmotic pump has no moving parts and produces an even flow along the entire length of the channel, ideal for early applications of  $\mu$ TAS that imagined separating and analysing aqueous solutions. Early efforts were first put into optimising injection and separation of liquids by switching voltages between the reservoirs containing reagent, carrier and waste [11].

Electrophoresis in a  $\mu$ TAS was reported in 1992 using silicon and glass [12]. This demonstrated success in using electroosmotic pumping for flow control in interconnected channels, without the use of valves, as well as the concept of integrating injection, separation, and detection into a single device. As electrophoresis was most commonly used to separate biological samples, usually charged molecules in aqueous solution, it could be used to detect amino acids separated on-chip, using laser induced fluorescence [13]. In addition to separation of biological samples, applications of reactions concerning biomolecules and the handling of cells also started to emerge.

Microfabricated device capability started to become more complicated and microfluidics found uses in DNA amplification by polymerase chain reaction (PCR) [14] and cellular metabolism [15]. As analysis of biological samples in water became available, fabrication of the devices from glass and silicon became unnecessary and inappropriate. Silicon was at the time expensive, but more importantly, opaque to visible and UV-light, and so couldn't be used with conventional methods of optical detection frequently used in biology. The increasing complexity of the devices also meant it became important for pumps and valves to be integrated into the device and these are more easily made from elastomers than silicon or other rigid materials. The trend towards studying mammalian cells lead to different requirements such as gas permeability, which neither glass or silicon can provide. It was for these reasons that the replacement of silicon and glass with polymers was required [16].

Poly(dimethylsiloxane) (PDMS) was the polymer of choice, the properties of which differ greatly from silicon or glass [17, 18]. The switch to PDMS was made even more attractive by the development of soft-lithography as a method for building prototype devices [19], and the development of a method to fabricate pneumatically actuated valves, pumps, and mixers [19]. These advances are only possible due to the elastomeric nature of PDMS and would not be possible with a pure silicon or glass devices. The improved methods of fabrication lead to the creation of the components required for more sophisticated experiments in the form of: valves that enabled immunoassaysb(Fig. 2.1)

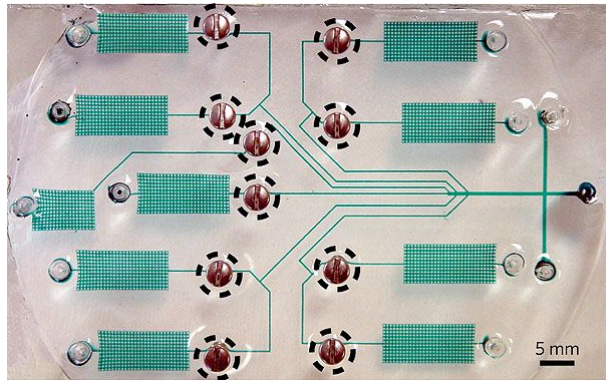


FIGURE 2.1: Components of a microfluidic device got increasingly complicated. This device from Ref.[20] performs immunoassays - widely used in medical and biological research. The screws (dashed circles) are manually operated valves. Water with green dye shows the channels.

[20]; an integrated microfluidic system for efficient mixing [21]; and pumps [22]. With these components, microfluidics was in a position to tackle more complex problems, one example of this is shown in Fig. 2.1.

As these fabrication methods become more widely used, the field of microfluidics moved from adding components to its analytical arsenal, to starting to find applications for devices. Microfluidic devices then found applications in protein crystallisation [23], separations coupled with mass spectroscopy [24], single cell manipulation [25], and synthesis of  $^{19}\text{F}$ -labelled organic compounds for use in PET scans [26].

A subsection of microfluidics began to emerge around this time too, as low Reynolds numbers make multiphase flow manipulation relatively easy, the generation and manipulation of droplets [27–29] then began to be explored. These experiments involved dispersing a liquid phase in a continuous liquid stream to form a monodisperse emulsion of (often) aqueous droplets in oil. These droplets were used to produce polymer particles [30], in making irregular particles [31], hollow microcapsules [32], and protein detection in cells [33]. An example of one of the ways droplets were first produced in microfluidic devices is shown in Fig. 2.2.

In parallel, another branch of microfluidics was being developed, its goal was to culture cells in a repeatable way. In their normal environment, cells are subject to multiple cues including cytokines and other signalling molecules from neighbouring cells, biochemical interactions with the extracellular matrix, mechanical stress, and direct cell to cell contacts. Microfluidics was seen as an ideal method of providing cells with these cues, in a controlled and reproducible fashion that couldn't be easily replicated with conventional cell culture. By using microfluidic devices one can combine cell culture with analytical techniques in order to probe the biochemical processes that govern cell behaviour.

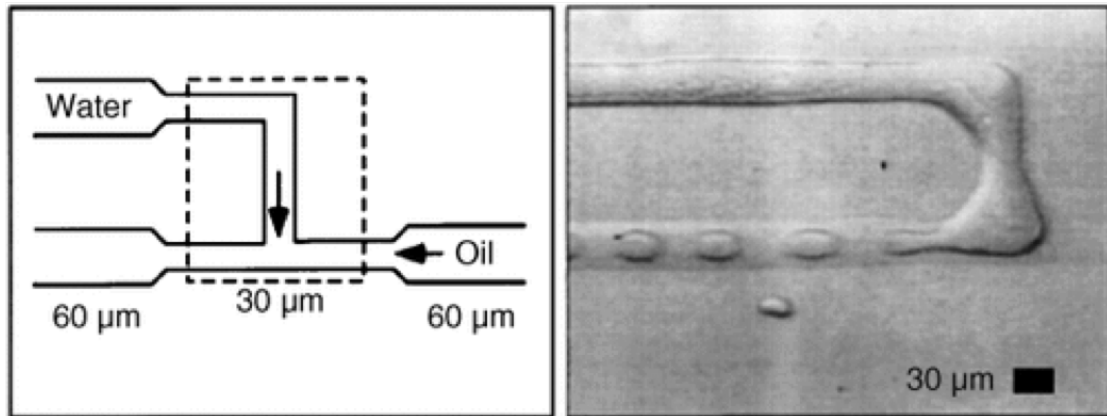


FIGURE 2.2: Formation of droplets in a T-Junction of a microfluidic device the continuous hydrocarbon phase disperses a water phase. Figure from [34]

Microfluidic devices have been used to enable cell-based assays, from culturing cells to biochemical analysis. In Fig. 2.3 images of different devices are shown that convey how complex the devices being produced were becoming. Despite integration of functionalities proving difficult, these demonstrate the power of miniaturisation and the ingenuity being developed in the field. Microfluidics can offer unique control over cell-cell and soluble cues, typical of *in vivo* cell environments, by combining microfabrication of 3D extracellular matrix (ECM) structures and fluid networks capable of delivering nutrients and oxygen [47].

Throughout the 2000s, microfabrication, which combined micropatterning techniques such as photolithography, photo-reactive chemistry, and soft lithography, made it possible to engineer the microenvironment of the cell on similar length scales to the cell itself [48]. This surface patterning of micro-metre sized features enabled control of cell-EDM interactions, and was used to fabricate 3D scaffolds on which to grow cells that were made of biodegradable materials [49].

One area of application was the 3D culture of liver cells. *In vitro* culture of liver cells is of particular interest as many drugs fail clinical studies because they either damage the liver directly, or because the metabolites produced by the liver are toxic [50]. Efforts were made to produce *in vitro* culture systems that mimic real liver conditions. In the liver, hepatocytes are found in a complex 3D environment in which nutrients, soluble factors and oxygen, are transported through blood capillaries and bile canaliculi. This 3D environment often contains polar tissue structure where the two sides of the cell are exposed to different media, for example, in the liver some hepatocytes are exposed to the bile on one side and blood on the other, which is hard to reproduce using 2D cell culture alone. Using silicon as a substrate, Powers *et al.* fabricated 3D liver reactors using array of 300 μm wide channels [51]. In their device they perfused rat liver cells providing fluid shear stresses within physiological range and found that the cells seeded into the channels rearranged extensively to form 'tissue like' structures, and remained viable for up to 2 weeks.

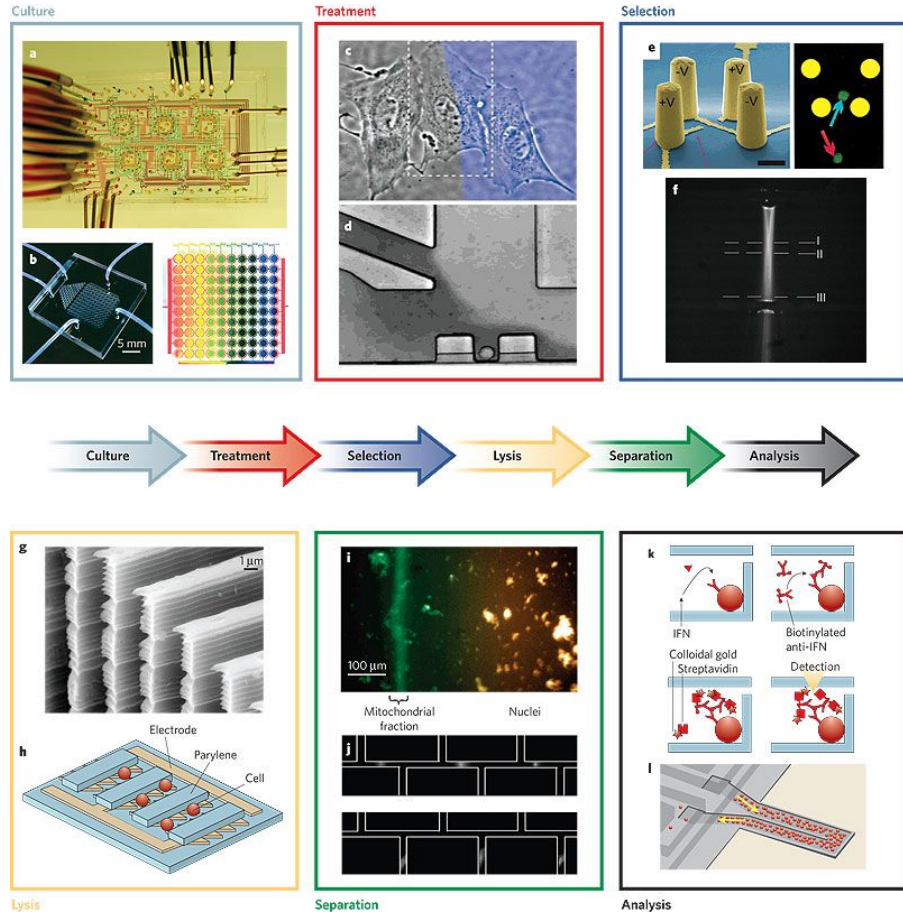


FIGURE 2.3: A collection of microfluidic devices that enabled cell based assays from cell culture, to selection and treatment, to analysis. **a**, Six bioreactors are operated in parallel in a single chip to monitor small numbers of cells [35]. **b**, Microfluidic cell-culture array with integrated concentration gradient generator (left). Image of concentration gradient when blue and yellow dye is used (right) [36]. **c** Two laminar streams exposing two sides of a single cell to different conditions [37]. **d**, Perfusion over a single trapped cell. The perfusion media can be switched in 100 ms [25]. **e**, (left) Cell dielectrophoresis trap. (right) Fluorescent image of trapped cell indicated by blue arrow [38]. **f**, Fluorescent image of light path at the detection zone in a micro flow cytometer [39]. **g** Scanning electron micrograph of a mechanical lysis device with sharp knife-like protrusions [40]. **h**, Schematic of electrical lysis device with microelectrodes [41]. **i**, Isoelectric focusing of cell organelles [42]. **j**, Two-dimensional separation of four model proteins. Isoelectric focusing (top) followed by SDS gel electrophoresis [43]. **k**, Schematic of immunoassay using microbeads as a solid support [44]. **l**, Schematic of a hollow cantilever-based mass sensor for analyte detection [45]. Taken from Ref.[46]

Later, Sivaraman *et al.* developed a different system to culture liver cells in a 3D scaffold using polycarbonate housing for a silicon device. This device contained microfabricated wells in which the cells were seeded and perfused with media. They also observed that the cells in the 3D culture had cell-cell contacts that resembled those found in tissues *in vivo* [50]. It has been observed that co-culture of hepatocytes with other cell types, including liver epithelial cells and Kupffer cells, prolongs the survival of cultured hepatocytes and helps maintain liver-specific properties such as albumin secretion [52].

As 3D cell culture became more widely used, a new sub-genre of microfluidics was formed, organ-on-a-chip. Early efforts had shown that microfabrication of adhesive substrates provided well-controlled environments for cell growth and expression of differentiated tissue-specific functions [53, 54]. Advances in soft lithography-based microfluidic devices made it easier to develop the more complex 3D architecture of living tissues and organs. For example, a poly(dimethylsiloxane) (PDMS) device was developed that contained structures which mimic the structure of the endothelial-epithelial interface that forms the liver sinusoid [55].

Along with liver function, kidney, lung, and body functions were replicated in microfluidic devices shown in Fig. 2.4. Whilst the liver and kidney offer highly simplified micro-engineered models, within organs, *in vivo* nutrients, hormones, metabolites, cytokines and physical signals are usually transferred across interfaces between adjacent living cells, and therefore require a much more complex microenvironment for true replication. Huh *et al.* created a model of the human alveolar-capillary interface, formed in a flexible PDMS device containing a central channel and two hollow side chambers [56]. A 10 µm thick PDMS membrane containing an ordered array of micropores (10 µm diameter) was stretched across the central channel, splitting it in two, see Fig. 2.4. Human alveolar epithelial cells were then cultured on one side of the membrane and exposed to air, while human lung capillary endothelial cells were cultured on the opposing side and exposed to flowing medium. When the hollow side chambers were exposed to vacuum, the cells were subjected to strain ranging from 5%-15% to match strain observed within whole lung *in vivo*. In doing so, they found their 'lung on a chip' accentuated the inflammatory responses of the cells to silica nanoparticles. This mechanical strain also enhanced uptake of nanoparticles and stimulated the transport into the vascular channel, and similar effects of physiological breathing were observed in whole mouse lung. These early organ-on-a-chip experiments paved the way for more complex 'Body-on-a-chip' devices. Body-on-a-chip devices contain multiple types of cultured cells connected by a network of microfluidic channels, which permit recirculation and exchange of metabolites in a physiologically-relevant manner [57]. These devices have found applications in drug screening and disease modelling [58].

As the complexity of cell culture within microfluidic devices increased, so to, did the detection methods. Coupling a detector to an LOC is critical for any analytical purpose. A number of detector technologies were demonstrated in microfluidic devices,

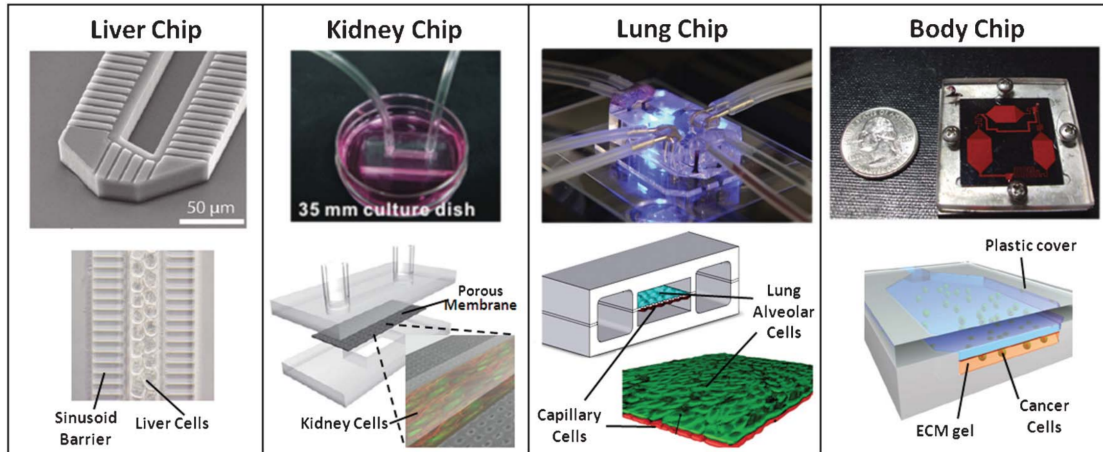


FIGURE 2.4: Organ-Organ and tissue-tissue interfaces in microdevices. Liver chip: A microfluidic liver device with cell culture and flow chambers separated by a baffle that separates cultured hepatocytes from fluid flow to simulate the endothelial-hepatocyte interface of the liver sinusoid. This geometry promotes alignment of hepatocytes in two lines that facilitates the production of functional bile canaliculi along hepatic-cord-like structures [55]. Kidney chip: A simple kidney on a chip that mimics the interface between epithelium and flowing urine was created by bonding a PDMS well and a PDMS channel to either side of a semi-permeable membrane on which cells are cultured and subjected to fluid flow [59]. Lung chip: A lung-on-a-chip capable of replicating mechanical strain caused by breathing, fabricated from PDMS that mimics the physiological function of the alveolar-capillary interface in the human lung. The hollow chambers are subjected to cyclic suction to replicate breathing movements whilst fluid flowing mimics blood flow [56]. Body chip: A microfluidic device containing multiple linked tissue types representing different organs was constructed by sealing three cell culture chambers against a cover. Each cell culture chamber contains a 3D ECM gel containing living cells from a different organ. Media was circulated through the chambers via microfluidic channels during operation [60]. Figure taken from [61].

including electrochemical [62], mechanical [63], and optical methods [64]. The small sample volumes typical to a microfluidic experiment are an important challenge to overcome for any detector, ideally, they should be highly sensitive and scalable to smaller dimensions.

The mechanism and features of the detection technologies are summarised in [65] and reproduced in Table 2.1.1.

Method	Mechanism	Features
Electrochemical	Measures changes in conductance, resistance and/or capacitance at the active surface of the electrodes	(+) Real-time detection, (+) Low-cost microelectrode fabrication, (-) Control of ionic concentrations before detection, (-) Short shelf life
Mechanical	Detection is based on variations of the resonant frequency or surface stress of the mechanical sensor	(+) Monolithic sensor integration, (+) Label free detection, (-) damping effects in liquid samples, (-) Detection takes time ( 30 mins), (-) Complex fabrication
Optical	Detects variations in light intensity, refractive index sensitivity, or interference pattern	(+) Minimal sample preparation, (+) Real-time detection, (+) Ubiquitous in laboratories, (-) Conventional instrumentation is expensive, (-) Set-up complexity

TABLE 2.1: Summary of electrochemical, mechanical and optical detection technologies employed in microfluidics.

Electrochemical detection involves the interaction of chemical species with electrodes or probes. This interaction results in a variation of signal, such as potential or current, which enables analysis of target analytes. The electrochemical phenomenon deals with two major effects: (i) chemical reactions are promoted by passing an electrical current through the electrode system; or (ii) electrode responses are triggered due to specific chemical reactions. These effects are usually observed using an electrolytic cell. Reactions of oxidation and reduction occurring at the surface of the electrodes are the basis for electron transfers between the electrolyte (sample) and the electrodes. In a typical electrolytic cell, the electrode system is formed by the working electrode, where detection of a certain analyte is analyzed, and the reference electrode, where a standard oxidation/reduction is conducted [66]. Wongkaew *et al.* reported an electrochemical biosensor that employed a microelectrode array. In the array, adjacent electrode fingers form micro-sized gaps which allow an increase of the diffusion flux of chemical species, thus leading to an enhanced collection efficiency and higher signal amplification. The microchannels of the device were made by hot embossing PMMA and the electrodes were made, by e-beam and wet-etching processes. The detection of targets using this system took 250 seconds and reported limits of detection of 12.5 pM.

Mechanical detection systems mainly used cantilever technology, which showed that it could be accurate when detecting biomolecules [67]. Cantilever-based devices generally operate in two different modes upon analyte binding: (i) static deflection, where binding on one side of a cantilever causes unbalanced surface stress resulting in a measurable deflection; (ii) dynamic, resonant mode, where binding on a cantilever causes

variations of its mass and consequently shifts the resonant frequency. Mechanical-based detection has the advantage that it may require no labelling of biomolecules. Labels often make the detection method more complicated, time-consuming, and costly, and could interfere with the function of biomolecules under investigation. Another characteristic of cantilever technology is the potential to fabricate large arrays of sensors for multi-molecular sensing [68]. Hou *et al* [69] presented a device that contained a micro-fabricated cantilever array for the specific detection of oxytetracycline (OTC), a common broadband antibiotic used in animals, that can accumulate in our food chain and cause side effects in humans. The device achieved this by functionalising the cantilevers with OTC specific DNA aptamers, these bind to the OTC and increase the load on the cantilevers causing them to deflect, and once calibrated can indicate the concentration of OTC in solution. The limit of detection in this case is 0.2 nM in 1000 seconds.

Optical detection is preferred for robust, sensitive, Lab on a chip devices. It has been the most widely used technique for quantitative proteomic analysis [70], and infectious disease diagnostics [71], due in part, to the ubiquity of the optical instrumentation required in biological laboratories, meaning these devices can be used readily in most locations. Conventional optical detection methods, including absorbance [72], chemiluminescence [73], fluorescence [74], and surface plasmon resonance (SPR) [75], have all been applied in microfluidic devices. Foudeh *et al.* [75] developed an SPR microdevice for the detection of *Legionella pneumophila*, which is the pathogenic organism that causes Legionellosis and is responsible for fatality rates of over 10% within hospital and industrial outbreaks [76]. The device is ultra-sensitive to RNA of *Legionella pneumophila* and has a limit of detection of 1 pM in less than 3 hours.

Presently, microfluidics is a large and diverse field, so much so that the areas that started out as sub-categories are now referred to as their own field of research. Indeed, within the last three years, the journal Lab on a Chip has published no less than 116 reviews focusing on a wide variety of applications that microfluidics now enjoys, such as: 3D printed fluidic networks [77]; droplet microfluidics for synthetic biology [78]; phase behaviour characterisation for industrial CO<sub>2</sub>, oil and gas [79]; the production of stem cells using messenger RNAs [80]; and paper microfluidics for diagnosis of malaria in low resource communities [81].

## 2.2 Quantum Theory of Nuclear Magnetic Resonance

### 2.2.1 Nuclear Spin

Nuclei have an intrinsic property known as spin. This spin can be represented by operators along the three Cartesian axes  $\hat{I}_x$ ,  $\hat{I}_y$ , and  $\hat{I}_z$ . The commutation relation between two operators is defined as:

$$[\hat{A}, \hat{B}] = \hat{A}\hat{B} - \hat{B}\hat{A}. \quad (2.1)$$

If  $[\hat{A}, \hat{B}] = 0$  the operators are said to commute. The physical implication of this is that the two observables can be measured at the same time, measuring one does not affect the outcome of the other and vice versa.

The spin operators  $\hat{I}_x$ ,  $\hat{I}_y$  satisfy  $\hat{I}_z$  have cyclic commutation rules:

$$[\hat{I}_x, \hat{I}_y] = i\hat{I}_z \quad (2.2)$$

$$[\hat{I}_y, \hat{I}_z] = i\hat{I}_x \quad (2.3)$$

$$[\hat{I}_x, \hat{I}_z] = i\hat{I}_y. \quad (2.4)$$

This cyclic commutation means that the spin that nuclei posses can be treated as a type of angular momentum and in NMR,  $\hat{I}_x$ ,  $\hat{I}_y$ , and  $\hat{I}_z$  are referred to as the spin angular momentum operators.

The total square angular momentum operator,  $\hat{I}^2$  can be defined as:

$$\hat{I}^2 = \hat{I}_x^2 + \hat{I}_y^2 + \hat{I}_z^2, \quad (2.5)$$

this commutes with the three spin angular momentum operators:

$$[\hat{I}^2, \hat{I}_x] = 0 \quad (2.6)$$

$$[\hat{I}^2, \hat{I}_y] = 0 \quad (2.7)$$

$$[\hat{I}^2, \hat{I}_z] = 0. \quad (2.8)$$

Spin angular momentum operators have eigenstates and eigenvalues. When the operators act on their eigenstate they return the eigenstate multiplied by a scalar eigenvalue. If the nuclear spin quantum number is  $I$ , then the operator  $\hat{I}_z$  has  $2I + 1$  eigenstates,  $m_I$ . States are denoted  $|I, m_I\rangle$  [82] and the angular momentum operator acts according to the following:

$$\hat{I}_z |I, m_I\rangle = m_I \hbar |I, m_I\rangle. \quad (2.9)$$

The total square angular momentum operator acts in the following way:

$$\hat{I}^2 |I, m_I\rangle = I(I+1)\hbar^2 |I, m_I\rangle, \quad (2.10)$$

where  $I$  can take half-integer and integer values from zero, i.e  $I = 0, \frac{1}{2}, 1, \frac{3}{2} \dots$ , and  $m_I$  takes one of the integer values from  $-I$  to  $+I$ .

### 2.2.2 Spin Systems

The simplest case that can be considered in NMR is a system of isolated spin-1/2 nuclei.

According to the quantum theory of angular momentum discussed in 2.2.1, a single spin-1/2, when placed in a magnetic field, has two eigenstates of angular momentum along the  $z$ -axis, denoted by  $|\alpha\rangle$  and  $|\beta\rangle$ , and defined as:

$$|\frac{1}{2}, +\frac{1}{2}\rangle = |\alpha\rangle \quad (2.11)$$

$$|\frac{1}{2}, -\frac{1}{2}\rangle = |\beta\rangle. \quad (2.12)$$

The states  $|\alpha\rangle$  and  $|\beta\rangle$  are called the *Zeeman eigenstates* of a spin-1/2 and are acted on by  $\hat{I}_z$  according to the following:

$$\hat{I}_z |\alpha\rangle = +\frac{1}{2}\hbar |\alpha\rangle \quad (2.13)$$

$$\hat{I}_z |\beta\rangle = -\frac{1}{2}\hbar |\beta\rangle, \quad (2.14)$$

Eqn. 2.13 shows that the eigenstate  $|\alpha\rangle$  has an eigenvalue of  $+\hbar/2$  and  $|\beta\rangle$  has an eigenvalue of  $-\hbar/2$ , these are said to be polarised along the  $z$ -axis. This polarization is represented in Fig. 2.5 by the up and down arrows pointing along the positive or negative  $z$ -axis, indicating the direction of well-defined spin angular momentum. These arrows should not be over-interpreted, as for the same spin, the  $x$  and  $y$  components are fundamentally unpredictable since the states  $|\alpha\rangle$  and  $|\beta\rangle$  are not eigenstates of the operators  $\hat{I}_x$  or  $\hat{I}_y$ . The arrow along the  $z$ -axis does not mean the  $x$ -axis angular momentum is zero. The  $x$ -axis angular momentum is *undefined* as measurements give  $\pm 1/2$  with equal probability and this is very hard to represent in a diagram.

The Zeeman eigenstates can be used to define the Zeeman basis. The two kets,  $|\alpha\rangle$  and  $|\beta\rangle$  can be represented by the column vectors:

$$|\alpha\rangle = \begin{pmatrix} 1 \\ 0 \end{pmatrix} \quad |\beta\rangle = \begin{pmatrix} 0 \\ 1 \end{pmatrix}, \quad (2.15)$$

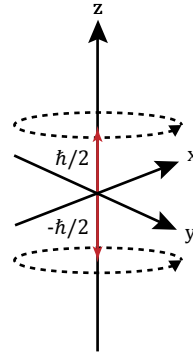


FIGURE 2.5: The projection of the two Zeeman eigenstates in a spin 1/2 nucleus. The dashed circles represent the undefined spin angular momentum in the  $xy$ -plane.

as well as kets, bras are also defined by taking the conjugate transpose of the ket,  $|\alpha\rangle^\dagger = \langle\alpha|$  such that

$$\langle\alpha| = \begin{pmatrix} 1 & 0 \end{pmatrix} \quad \langle\beta| = \begin{pmatrix} 0 & 1 \end{pmatrix}. \quad (2.16)$$

The state,  $|\psi\rangle$ , of a two level system can now be completely described in this basis as the linear combination of the basis states:

$$|\psi\rangle = c_1 |\alpha\rangle + c_2 |\beta\rangle = \begin{pmatrix} c_1 \\ c_2 \end{pmatrix} \quad (2.17)$$

$$\langle\psi| = c_1^* \langle\alpha| + c_2^* \langle\beta| = \begin{pmatrix} c_1^* & c_2^* \end{pmatrix}. \quad (2.18)$$

These are normalised such that  $c_1 c_1^* + c_2 c_2^* = 1$ .

To complete the picture, the states must be orthonormal. Orthonormality between states exists if the inner product of the basis states  $|r_i\rangle$  and  $|r_j\rangle$  satisfies the following conditions:

$$\langle r_i | r_j \rangle = \delta_{ij}, \quad (2.19)$$

where the Kronecker delta,  $\delta_{ij}$  is:

$$\delta_{ij} = \begin{cases} 0 & \text{if } i \neq j \\ 1 & \text{if } i = j \end{cases}, \quad (2.20)$$

and where  $\langle r_i | r_j \rangle = \delta_{ij}$  denotes taking the dot product between the two vectors  $|r_i\rangle$  and  $|r_j\rangle$ .

The basis states help to quantify the component of a state vector along that state. Take our example from Eqn. 2.17, inner products of the overall state,  $|\psi\rangle$  with  $|\alpha\rangle$  and

$|\beta\rangle$ , can be constructed to determine component of the basis states.

$$\langle \alpha | \psi \rangle = c_1 \quad \langle \beta | \psi \rangle = c_2. \quad (2.21)$$

The outer product of the basis state,  $|r_n\rangle$ , for an N-spin system must satisfy:

$$\sum_{n=1}^N |r_n\rangle \langle r_n| = \mathbb{1}, \quad (2.22)$$

where  $\mathbb{1}$  is an N by N identity matrix.

When a second spin is introduced, the Hilbert space is extended to accommodate additional spin states by taking the tensor product of the basis states:

$$|\alpha_1\alpha_2\rangle = |\alpha_1\rangle \otimes |\alpha_2\rangle = \begin{pmatrix} 1 \\ 0 \\ 0 \\ 0 \end{pmatrix} \quad |\alpha_1\beta_2\rangle = |\alpha_1\rangle \otimes |\beta_2\rangle = \begin{pmatrix} 0 \\ 1 \\ 0 \\ 0 \end{pmatrix} \quad (2.23)$$

$$|\beta_1\alpha_2\rangle = |\beta_1\rangle \otimes |\alpha_2\rangle = \begin{pmatrix} 0 \\ 0 \\ 1 \\ 0 \end{pmatrix} \quad |\beta_1\beta_2\rangle = |\beta_1\rangle \otimes |\beta_2\rangle = \begin{pmatrix} 0 \\ 0 \\ 0 \\ 1 \end{pmatrix}. \quad (2.24)$$

The subscripts indicate which spin is being referred to, i.e.  $|\beta_1\alpha_2\rangle$  means that spin 1 is in the  $\beta$  state and spin 2 is in the  $\alpha$  state.

### 2.2.3 Pauli matrices and more operators

In quantum mechanics each observation is associated with a particular operator. For example, the measurement of the spin angular momentum along the  $z$ -axis is associated with  $\hat{I}_z$  and when applied to the  $|\alpha\rangle$  gives the result seen in Eqn. 2.13. The probability of obtaining this result is 1 as  $|\alpha\rangle$  is an eigenstate of  $\hat{I}_z$ . In all other cases the results follow statistical laws and the result of an individual experiment is unpredictable.

In quantum mechanics there is a formula for the average result of very many observations, this is called the expectation value of a general operator,  $\hat{A}$ , when applied to a spin-1/2 system,  $|\psi\rangle$  is denoted:

$$\langle \hat{A} \rangle = \langle \psi | \hat{A} | \psi \rangle, \quad (2.25)$$

from the general case listed in Eqn. 2.17 this becomes:

$$\langle \hat{A} \rangle = \langle \psi | \hat{A} | \psi \rangle \quad (2.26)$$

$$= (c_1^* \ c_2^*) \begin{pmatrix} A_{11} & A_{12} \\ A_{21} & A_{22} \end{pmatrix} \begin{pmatrix} c_1 \\ c_2 \end{pmatrix} \quad (2.27)$$

$$= c_1 c_1^* A_{11} + c_1 c_2^* A_{12} + c_2 c_1^* A_{21} + c_2 c_2^* A_{22}. \quad (2.28)$$

The end sum of all these products is the expectation value of a single spin 1/2 particle when acted upon by  $\hat{A}$ , this quickly becomes cumbersome should there be more than one spin. An easier way to deal with expectation values is described in 2.2.4.

In NMR three operators are used to determine the projection of spin angular momentum along a specific axis,  $\hat{I}_x$ ,  $\hat{I}_y$ , and  $\hat{I}_z$ . These are defined by the Pauli matrices in the Zeeman basis multiplied by  $\hbar/2$ .

$$\hat{I}_x = \frac{\hbar}{2} \begin{pmatrix} 0 & 1 \\ 1 & 0 \end{pmatrix} \quad \hat{I}_y = \frac{\hbar}{2i} \begin{pmatrix} 0 & 1 \\ -1 & 0 \end{pmatrix} \quad \hat{I}_z = \frac{\hbar}{2} \begin{pmatrix} 1 & 0 \\ 0 & 1 \end{pmatrix}. \quad (2.29)$$

As an example, let's take a spin-1/2 particle in a magnetic field and project the  $|\alpha\rangle$  state along the z-axis.

$$\hat{I}_z |\alpha\rangle = \frac{\hbar}{2} \begin{pmatrix} 1 & 0 \\ 0 & 1 \end{pmatrix} \begin{pmatrix} 1 \\ 0 \end{pmatrix} = \frac{\hbar}{2} \begin{pmatrix} 1 \\ 0 \end{pmatrix} = \frac{\hbar}{2} |\alpha\rangle, \quad (2.30)$$

$\hbar/2$  is found to be the eigenvalue of  $|\alpha\rangle$  for the operator  $\hat{I}_z$ .

Three operators are now examined, and how they act on states is explored. They are the total square angular momentum,  $\hat{I}^2$ , and the two shift operators,  $\hat{I}^+$  and  $\hat{I}^-$ , which are defined as the following:

$$\hat{I}^2 = \hat{I}_x^2 + \hat{I}_y^2 + \hat{I}_z^2 \quad (2.31)$$

$$\hat{I}^+ = \hat{I}_x + i\hat{I}_y \quad (2.32)$$

$$\hat{I}^- = \hat{I}_x - i\hat{I}_y. \quad (2.33)$$

They act on general states according to:

$$\hat{I}^2 |I, m_I\rangle = I(I+1)\hbar |I, m_I\rangle \quad (2.34)$$

$$\hat{I}^+ |I, m_I\rangle = \sqrt{(I(I+1) - m_I(m_I+1))} \hbar |I, m_{I+1}\rangle \quad (2.35)$$

$$\hat{I}^- |I, m_I\rangle = \sqrt{(I(I+1) - m_I(m_I-1))} \hbar |I, m_{I-1}\rangle. \quad (2.36)$$

Using a spin-1/2 particle in a magnetic field as an example, let these operators act on the  $|\alpha\rangle$  and  $|\beta\rangle$  states:

$$\hat{I}^2 |\alpha\rangle = \frac{3}{4}\hbar^2 |\alpha\rangle \quad (2.37)$$

$$\hat{I}^+ |\alpha\rangle = 0 \quad (2.38)$$

$$\hat{I}^- |\alpha\rangle = |\beta\rangle \quad (2.39)$$

$$\hat{I}^+ |\beta\rangle = |\alpha\rangle \quad (2.40)$$

$$\hat{I}^- |\beta\rangle = 0, \quad (2.41)$$

the '+' and '-' denote raising or lowering  $m_I$  by 1.

As shown in Eqn. 2.2, the three angular momentum operators cyclically commute. This means the *sandwich formula* applies.

In general, if  $\hat{A}$ ,  $\hat{B}$ , and  $\hat{C}$  cyclically commute, then:

$$\exp\{-i\theta\hat{A}\} \hat{B} \exp\{+i\theta\hat{A}\} = \hat{B} \cos\theta + \hat{C} \sin\theta. \quad (2.42)$$

Geometrically, this can be thought of as a rotation of  $\hat{B}$  by  $\hat{A}$  through an angle  $\theta$ .

It is important to define a set of rotation operators as these are essential for the generation of signal in NMR. They are defined as the complex exponentials of the angular momentum operators seen in 2.2.1:

$$\hat{R}_x(\theta) = \exp\{-i\theta\hat{I}_x\} \quad (2.43)$$

$$\hat{R}_y(\theta) = \exp\{-i\theta\hat{I}_y\} \quad (2.44)$$

$$\hat{R}_z(\theta) = \exp\{-i\theta\hat{I}_z\}, \quad (2.45)$$

and they too have matrix representations:

$$\hat{R}_x(\theta) = \begin{pmatrix} \cos(\frac{1}{2}\theta) & -i \sin(\frac{1}{2}\theta) \\ -i \sin(\frac{1}{2}\theta) & \cos(\frac{1}{2}\theta) \end{pmatrix} \quad (2.46)$$

$$\hat{R}_y(\theta) = \begin{pmatrix} \cos(\frac{1}{2}\theta) & \sin(\frac{1}{2}\theta) \\ \sin(\frac{1}{2}\theta) & \cos(\frac{1}{2}\theta) \end{pmatrix} \quad (2.47)$$

$$\hat{R}_z(\theta) = \begin{pmatrix} \exp\{-i\frac{1}{2}\theta\} & 0 \\ 0 & \exp\{+i\frac{1}{2}\theta\} \end{pmatrix}. \quad (2.48)$$

The rotation operators are applied to the angular momentum operators using the sandwich formula:

$$\hat{R}_x(\theta)\hat{I}_z = \exp\{-i\hat{I}_x\theta\}\hat{I}_z\exp\{+i\hat{I}_x\theta\}. \quad (2.49)$$

The result of this is a rotation of  $\hat{I}_z$  around the  $x$ -axis by an angle  $\theta$ :

$$\hat{R}_x(\theta)\hat{I}_z = \cos\theta\hat{I}_z - \sin\theta\hat{I}_y. \quad (2.50)$$

The rotational direction (sign of the  $\sin\theta$  term) is determined by the right hand co-ordinate system defined in Eqn. 2.2.

How each rotational operator transforms the spin angular momentum operators is shown below:

$$\hat{R}_x(\theta) \begin{cases} \hat{I}_x \rightarrow \hat{I}_x \\ \hat{I}_y \rightarrow \hat{I}_y \cos\theta + \hat{I}_z \sin\theta \\ \hat{I}_z \rightarrow \hat{I}_z \cos\theta - \hat{I}_y \sin\theta \end{cases} \quad (2.51)$$

$$\hat{R}_y(\theta) \begin{cases} \hat{I}_x \rightarrow \hat{I}_x \cos\theta - \hat{I}_z \sin\theta \\ \hat{I}_y \rightarrow \hat{I}_y \\ \hat{I}_z \rightarrow \hat{I}_z \cos\theta + \hat{I}_y \sin\theta \end{cases} \quad (2.52)$$

$$\hat{R}_z(\theta) \begin{cases} \hat{I}_x \rightarrow \hat{I}_x \cos\theta + \hat{I}_y \sin\theta \\ \hat{I}_y \rightarrow \hat{I}_y \cos\theta - \hat{I}_x \sin\theta \\ \hat{I}_z \rightarrow \hat{I}_z \end{cases}. \quad (2.53)$$

## 2.2.4 Density Operator

In Eqn. 2.26, the expectation value of an operator was expressed as the product of the matrix representations of the state and the operator. Simplification of this is possible by constructing a matrix of the quadratic products of the superposition coefficients. If in the general case:

$$|\psi\rangle = \begin{pmatrix} c_1 \\ c_2 \end{pmatrix} = c_1 |\alpha\rangle + c_2 |\beta\rangle \quad (2.54)$$

$$\langle\psi| = \begin{pmatrix} c_1^* & c_2^* \end{pmatrix} = c_1^* \langle\alpha| + c_2^* \langle\beta|, \quad (2.55)$$

then the matrix has the form:

$$|\psi\rangle\langle\psi| = \begin{pmatrix} c_1 c_1^* & c_1 c_2^* \\ c_2 c_1^* & c_2 c_2^* \end{pmatrix}. \quad (2.56)$$

The expectation value of the operator  $\hat{A}$  can now be expressed as:

$$\langle\hat{A}\rangle = \text{Tr}\{|\psi\rangle\langle\psi|\hat{A}\}. \quad (2.57)$$

If there are now  $N$  spins considered, the result of measuring  $A$  is still uncertain. However, an expression for the most likely outcome,  $A_{\text{obs}}$ , can be written by using the sum of expectation values:

$$A_{\text{obs}} = \text{Tr}\{N^{-1} |\psi_1\rangle\langle\psi_1| + |\psi_2\rangle\langle\psi_2| + \dots) \hat{A}\}. \quad (2.58)$$

this can be simplified by defining an operator,  $\hat{\rho}$ :

$$\hat{\rho} = N^{-1}(|\psi_1\rangle\langle\psi_1| + |\psi_2\rangle\langle\psi_2| + \dots), \quad (2.59)$$

where  $N$  is the number of spins in the ensemble. For brevity, this is written as:

$$\hat{\rho} = \overline{|\psi\rangle\langle\psi|}, \quad (2.60)$$

where the overbar indicates the average over all members of the ensemble.

Now the expectation of  $\hat{A}$  over all members of some spin ensemble can be written as:

$$\langle A \rangle = \text{Tr}\{\hat{\rho}\hat{A}\}, \quad (2.61)$$

the operator  $\hat{\rho}$  is referred to as the density matrix.

$$\hat{\rho} = \begin{pmatrix} \overline{c_1 c_1^*} & \overline{c_1 c_2^*} \\ \overline{c_2 c_1^*} & \overline{c_2 c_2^*} \end{pmatrix} = \begin{pmatrix} \rho_\alpha & \rho_+ \\ \rho_- & \rho_\beta \end{pmatrix}. \quad (2.62)$$

The diagonal elements of  $\hat{\rho}$ ,  $\rho_\alpha$  and  $\rho_\beta$ , are state populations or the probabilities of being in a certain state.

The off-diagonal elements are coherences between states. These coherences represent superposition states in the ensemble, the coherences are complex numbers and two coherences between the same pair of states are complex conjugates of each other i.e.:

$$\langle \alpha | \hat{\rho} | \beta \rangle = (\langle \beta | \hat{\rho} | \alpha \rangle)^* = c_1 c_2^* = (c_1^* c_2)^*. \quad (2.63)$$

The coherence order between two states in a magnetic field is defined as the difference in spin angular momentum projection along the  $z$  axis. In our two spin system this would be:

$$\hat{I}_z |\beta\rangle = m_\alpha = +\frac{1}{2}\hbar |\alpha\rangle \quad (2.64)$$

$$\hat{I}_z |\beta\rangle = m_\beta = -\frac{1}{2}\hbar |\beta\rangle. \quad (2.65)$$

These results can be used to calculate the coherence order of the coherence  $\rho_+$ :

$$m_\alpha - m_\beta = +1, \quad (2.66)$$

and conversely the coherence order of  $\rho_-$  is:

$$m_\beta - m_\alpha = -1. \quad (2.67)$$

The density operator can be written as:

$$\hat{\rho} = \rho_\alpha \hat{I}^\alpha + \rho_\beta \hat{I}^\beta + \rho_+ \hat{I}^+ + \rho_- \hat{I}^-, \quad (2.68)$$

using the shift operators,  $\hat{I}^+$  and  $\hat{I}^-$ , and the projection operators,  $\hat{I}^\alpha$  and  $\hat{I}^\beta$ , these have the following matrix representations:

$$\begin{aligned} \hat{I}^+ &= \begin{pmatrix} 0 & 1 \\ 0 & 0 \end{pmatrix} & \hat{I}^- &= \begin{pmatrix} 0 & 0 \\ 1 & 0 \end{pmatrix} \\ \hat{I}^\alpha &= \begin{pmatrix} 1 & 0 \\ 0 & 0 \end{pmatrix} & \hat{I}^\beta &= \begin{pmatrix} 0 & 0 \\ 0 & 1 \end{pmatrix}. \end{aligned}$$

The physical interpretations of the components of the density operator can help to understand the microscopic state of the individual spins. The sum of the populations,  $\rho_\alpha$  and  $\rho_\beta$ , is always equal to one, only the differences between the states have any significance. The difference in population indicates the net longitudinal spin polarization, i.e. if the  $|\alpha\rangle$  state population is larger than the  $|\beta\rangle$  state, then there is net polarization of the spins along the external field direction.

The presence of the coherences,  $\rho_+$  and  $\rho_-$ , indicates transverse spin magnetization i.e. net spin polarization *perpendicular* to the external field. These coherences are complex numbers and as such have phase and amplitude. The phase of the coherences indicates the direction of the spin polarization in the  $xy$ -plane. The  $(-1)$ -quantum coherence is written as:

$$\rho_- = |\rho_-| \exp\{i\phi_-\}, \quad (2.69)$$

and the polarization axis of the spins is:

$$\mathbf{e}'_x \cos \phi_- + \mathbf{e}'_y \sin \phi_-. \quad (2.70)$$

These populations and coherences play a vital role in NMR and will be re-visited in a later section.

### 2.2.5 The Hamiltonian

The Hamiltonian plays an important part in quantum systems. When the Hamiltonian acts on an eigenstate, the eigenvalue returned is the energy level of that state.

### 2.2.5.1 Spins in a magnetic field

In NMR the energy of a nucleus in a magnetic field,  $E$ , is given by:

$$E = -m_I \hbar \gamma B_0, \quad (2.71)$$

where  $m_I$  is the azimuthal quantum number,  $\hbar$  is the reduced Planck constant,  $\gamma$  is the gyromagnetic ratio, and  $B_0$  is the external field taken to be orientated along the  $z$ -axis.

For a spin-1/2 nuclei there are two states labelled as  $\alpha$  and  $\beta$  and these have an energy difference depicted in Fig. 2.6.

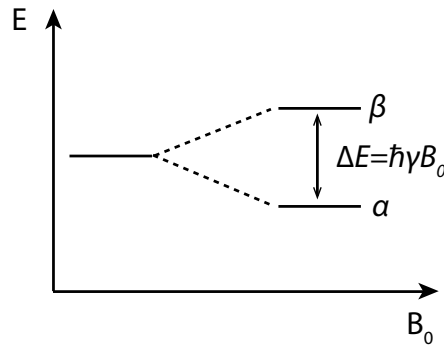


FIGURE 2.6: Energy level and  $\Delta E$  of the two energy levels for a spin-1/2 nucleus.

This splitting of energy levels due to the presence of a magnetic field is referred to as Zeeman splitting. When examining a spin ensemble at thermal equilibrium, overall, there is a slight bias to the lower energy state  $\alpha$ . This preference can be quantified by calculating the ratio of the populations:

$$\frac{\rho_\beta}{\rho_\alpha} = \exp\left\{-\frac{\Delta E}{k_B T}\right\}, \quad (2.72)$$

where  $\rho_\beta/\rho_\alpha$  is the population ratio between the states,  $k_B$  is the Boltzmann constant, and  $T$  is the temperature. The polarization,  $p$ , of a system of spin-1/2 nuclei is

$$p = \frac{P_\alpha - P_\beta}{P_\alpha + P_\beta} = \tanh\left(\frac{\gamma \hbar B_0}{2k_b T}\right). \quad (2.73)$$

For a typical NMR experiment, which operates at  $298K$  and a field of  $14.1$  T, the polarization level,  $p \approx 10^{-5}$  which means that the spins are aligned weakly in the same direction as the magnetic field. It is this small polarization that gives rise to the NMR signal. One possible solution to the low polarization levels at thermal equilibrium is called hyperpolarization, and involves strategies that produce non equilibrium polarization levels.

When placed in a magnetic field, the nuclei will precess around the axis of the field at a rate known as the Larmor frequency, this is defined as:

$$\omega_j^0 = -\gamma_j B_0, \quad (2.74)$$

where  $\gamma_j$  is the gyromagnetic ratio for a nucleus,  $j$ . The gyromagnetic ratio is typically 10s of MHz T<sup>-1</sup> which give Larmor frequencies in the 100s of MHz in an NMR experiment.

If  $|\psi_1\rangle$  and  $|\psi_2\rangle$  are eigenstates of the Hamiltonian  $\hat{\mathcal{H}}$ , then

$$\hat{\mathcal{H}} |\psi_1\rangle = E_1 |\psi_1\rangle \quad (2.75)$$

$$\hat{\mathcal{H}} |\psi_2\rangle = E_2 |\psi_2\rangle. \quad (2.76)$$

The Hamiltonian can also be expressed in matrix form:

$$\hat{\mathcal{H}} = \begin{pmatrix} E_1 & 0 \\ 0 & E_2 \end{pmatrix}. \quad (2.77)$$

If the Hamiltonian is written in the eigenbasis of the system, its main diagonal corresponds to state energies and it has values of 0 everywhere else.

The evolution in time of a quantum system is described by the Schrödinger equation:

$$\frac{d}{dt} |\psi\rangle = i\hbar^{-1} \hat{\mathcal{H}} |\psi\rangle. \quad (2.78)$$

The factor of  $\hbar^{-1}$  here is cumbersome and can be removed by defining a Hamiltonian in natural units,  $\hat{H}$ , such that:

$$\hat{H} = \hbar^{-1} \hat{\mathcal{H}}. \quad (2.79)$$

Both of these Hamiltonians share the same eigenfunctions:

$$\hat{H} |\psi_1\rangle = \omega_{\psi_1} |\psi_1\rangle, \quad (2.80)$$

the eigenvalues are denoted  $\omega_\psi$  and are given by:

$$\omega_{\psi_1} = \hbar^{-1} E_1, \quad (2.81)$$

and the eigenvalue,  $\omega_{\psi_1}$ , is the energy of the state  $|\psi\rangle$  in *units of  $\hbar$* .

Returning to the example of a spin-1/2 particle in a magnetic field, the Hamiltonian is initially proportional to the  $z$  angular momentum operator:

$$\hat{H} = \omega^0 \hat{I}_z, \quad (2.82)$$

where  $\omega^0 = -\gamma B_0$  and is the Larmor frequency from Eqn. 2.74. In matrix form, in the original Zeeman basis, the Hamiltonian is:

$$\hat{H} = \begin{pmatrix} +\frac{\omega}{2} & 0 \\ 0 & -\frac{\omega}{2} \end{pmatrix}, \quad (2.83)$$

where

$$\hat{H} |\alpha\rangle = +\frac{\omega}{2} |\alpha\rangle. \quad (2.84)$$

### 2.2.6 Spin precession

As discussed when describing Larmor frequency when a spin-1/2 particle is placed in a magnetic field it precesses at the Larmor frequency. In quantum mechanics this precession means that the spin state  $|\psi\rangle$  depends on time.

The law of motion for the spin is the time dependent Schrödinger equation:

$$\frac{d}{dt} |\psi\rangle(t) = -i\hat{H} |\psi\rangle(t). \quad (2.85)$$

The spin Hamiltonian is:

$$\hat{H} = \omega^0 \hat{I}_z, \quad (2.86)$$

the equation of motion then becomes:

$$\frac{d}{dt} |\psi\rangle(t) = -i\omega^0 \hat{I}_z |\psi\rangle(t), \quad (2.87)$$

this is a first order differential equation that has the solution:

$$|\psi\rangle(t) = \exp\{-i\omega^0 \Delta t \hat{I}_z\} \psi(t_0), \quad (2.88)$$

where  $t_0$  is the initial time and  $\Delta t$  is the difference in time between  $t_0$  and  $t$ . As the  $\omega^0 \Delta t$  term is angular frequency multiplied by time this simply gives an angle. This shows that it is equal to a rotation about the  $z$ -axis:

$$\hat{R}_z \theta = \exp\{-i\theta \hat{I}_z\}. \quad (2.89)$$

The solution therefore to the Schrödinger equation in the absence of r.f. fields is:

$$|\psi\rangle(t) = \hat{R}_z(\omega^0 \Delta t) |\psi\rangle(t_0). \quad (2.90)$$

In the absence of r.f. fields the Schrödinger equation says that the spin rotates around the  $z$ -axis, through the angle  $\omega_0 \Delta t$

### 2.2.7 Rotating Frame

The field,  $B_0$ , of a regular NMR experiment is many Tesla, giving precession frequencies of hundreds of megahertz. These frequencies correspond to radio frequencies in the electromagnetic spectrum. When considering these precessing spins it can be useful to change from a static frame to a rotating frame of reference.

the static frame of reference axes ( $x$ ,  $y$ , and  $z$ ) and the rotating frame axes ( $x'$ ,  $y'$ , and  $z'$ ) of reference are connected through a time dependent angle,  $\Phi(t)$  such that:

$$x' = x \cos \Phi(t) + y \sin \Phi(t) \quad (2.91)$$

$$y' = y \cos \Phi(t) - x \sin \Phi(t) \quad (2.92)$$

$$z' = z. \quad (2.93)$$

The frame rotates with a constant frequency  $\omega_{\text{ref}}$  around the  $z$ -axis:

$$\Phi(t) = \omega_{\text{ref}}t + \phi_{\text{ref}}, \quad (2.94)$$

for brevity ( $t$ ) is now dropped.

If a spin in state  $|\psi\rangle$  has a Larmor frequency equal to  $\omega_{\text{ref}}$  then the spin state in the rotating frame,  $|\tilde{\psi}\rangle$  is:

$$|\tilde{\psi}\rangle = \hat{R}_z(-\Phi) |\psi\rangle, \quad (2.95)$$

where the tilde denotes a state in the rotating frame.

These of course have an equation of motion:

$$\frac{d}{dt} |\tilde{\psi}\rangle = i\hbar^{-1} \hat{H} |\tilde{\psi}\rangle, \quad (2.96)$$

where:

$$\hat{H} = \hat{R}_z(-\Phi) \hat{H} \hat{R}_z(\Phi) - \omega_{\text{ref}} \hat{I}_z. \quad (2.97)$$

#### 2.2.7.1 Precession in the rotating frame

The spin Hamiltonian in a static field is:

$$\hat{H}^0 = \omega^0 \hat{I}_z. \quad (2.98)$$

The rotating frame Hamiltonian is:

$$\hat{H} = \omega^0 \hat{R}_z(-\Phi) \hat{I}_z \hat{R}_z(\Phi) - \omega_{\text{ref}} \hat{I}_z = (\omega^0 - \omega_{\text{ref}}) \hat{I}_z. \quad (2.99)$$

The frequency  $\omega^0 - \omega_{\text{ref}}$  is the difference between the Larmor frequency and that of the frame and is denoted,  $\Omega^0$ :

$$\Omega^0 = \omega^0 - \omega_{\text{ref}}. \quad (2.100)$$

The rotating-frame spin Hamiltonian in the presence pf a static field, is therefore:

$$\hat{H} = \Omega^0 \hat{I}_z. \quad (2.101)$$

### 2.2.8 Radio Frequency Pulses

In NMR 'pulses' are used to manipulate the spin states. These pulses take the form of an oscillating magnetic field applied at a frequency such that it is resonant with the precessing spin. The frequencies correspond to radio frequencies and as such, the pulses and fields are referred to as r.f. pulses and r.f. fields respectively.

When an r.f. pulse is applied, the spin experiences two magnetic fields: a static field generated by the magnet; and an oscillating field from the excitation coil. The static field is much larger then the oscillating r.f. field.

The weak r.f. field produces a large effect on the nuclear spin due to it being *resonant* with the precession of that spin. This allows the effect of the weak r.f. field to accumulate as time goes on. If the pulse is applied for long enough, then the weak r.f. field can cause a large change in the spin state. In practice, this corresponds to applying several microseconds of an r.f. pulse, which allows for several hundred Larmor precession cycles.

For an r.f. pulse of of phase,  $\phi_p$ , applied along the  $x$ -axis, the r.f. field oscillates at the spectrometer resonance frequency, $\omega_{\text{ref}}$ , and the spin Hamiltonian during the r.f. pulse is given by:

$$\hat{H} = \omega^0 \hat{I}_z + \hat{H}_{\text{RF}} t, \quad (2.102)$$

where

$$\hat{H}_{\text{RF}}(t) = -\frac{1}{2}\gamma B_{\text{RF}} \sin \theta_{\text{RF}} \hat{R}_z(\Phi_p) \hat{I}_x \hat{R}_z(-\Phi_p), \quad (2.103)$$

and

$$\Phi_p(t) = \omega_{\text{ref}} t + \phi_p. \quad (2.104)$$

The rotating frame Hamiltonian is:

$$\hat{H} = -\frac{1}{2}\gamma B_{\text{RF}} \sin \theta_{\text{RF}} \hat{R}_z(-\Phi + \Phi_p) \hat{I}_x \hat{R}_z(\Phi - \Phi_p) + (\omega^0 - \omega_{\text{ref}}) \hat{I}_z \quad (2.105)$$

$$= -\frac{1}{2}\gamma B_{\text{RF}} \sin \theta_{\text{RF}} \hat{R}_z(-\phi_{\text{ref}} + \phi_p) \hat{I}_x \hat{R}_z(\phi_{\text{ref}} - \phi_p) + \Omega^0 \hat{I}_z, \quad (2.106)$$

an additional simplification is possible if the value of  $\phi_{\text{ref}}$ , which is  $\pi$  for positive  $\gamma$  spins, and has the effect of changing the sign of the  $\gamma B_{\text{RF}}$  term is included:

$$\hat{\tilde{H}} = \omega_{\text{nut}} \hat{R}_z(\phi_p) \hat{I}_x \hat{R}_z(-\phi_p) + \Omega^0 \hat{I}_z, \quad (2.107)$$

where  $\omega_{\text{nut}}$  is the nutation frequency:

$$\omega_{\text{nut}} = \left| -\frac{1}{2} \gamma B_{\text{RF}} \sin \theta_{\text{RF}} \right|, \quad (2.108)$$

the nutation frequency is the measure of the r.f. field amplitude.

Using the sandwich property again the final form of the rotating-frame Hamiltonian during an r.f. pulse is:

$$\hat{\tilde{H}} = \Omega^0 \hat{I}_z + \omega_{\text{nut}} (\hat{I}_x \cos \phi_p + \hat{I}_y \sin \phi_p). \quad (2.109)$$

### 2.2.8.1 *x*-pulse

To illustrate the effect an r.f. pulse has on a sample, consider a strong pulse with frequency  $\omega_{\text{ref}}$ , duration  $\tau$ , and phase  $\phi_p = 0$  (an '*x*-pulse'). The amplitude is given by  $\omega_{\text{ref}}$ . Assuming this pulse to be applied directly on resonance such that  $\Omega^0 = 0$ . The rotating frame spin Hamiltonian is:

$$\hat{\tilde{H}} = \omega_{\text{ref}} \hat{I}_x, \quad (2.110)$$

the motion of the spin states may be found using the rotating frame Schrödinger equation. If the spin state before the pulse is given by  $|\tilde{\psi}\rangle_1$  and the spin state after the pulse is  $|\tilde{\psi}\rangle_2$  then they are related by:

$$|\tilde{\psi}\rangle_2 = \hat{R}_x(\theta) |\tilde{\psi}\rangle_1, \quad (2.111)$$

where the rotation operator is as defined in Eqn. 2.43 and the angle  $\theta$  is given by

$$\theta = \omega_{\text{nut}} \tau, \quad (2.112)$$

this angle is referred to as the *flip angle* of the pulse.

To calculate what effect the pulse has on spins in specific states the matrix representation can be used. A  $(\pi/2)_x$  pulse, which means a flip angle of  $\theta = \pi/2$  and a phase of  $\phi_p = 0$ , applied to spin in the state  $|\alpha\rangle$  can be calculated using the matrix

representation of  $\hat{R}_x(\theta)$  as:

$$\hat{R}_x(\pi/2)|\alpha\rangle = \frac{1}{\sqrt{2}} \begin{pmatrix} \cos(\frac{1}{2}\pi/2) & -i \sin(\frac{1}{2}\pi/2) \\ -i \sin(\frac{1}{2}\pi/2) & \cos(\frac{1}{2}\pi/2) \end{pmatrix} \begin{pmatrix} 1 \\ 0 \end{pmatrix} \quad (2.113)$$

$$= \frac{1}{\sqrt{2}} \begin{pmatrix} 1 & -i \\ -i & 1 \end{pmatrix} \begin{pmatrix} 1 \\ 0 \end{pmatrix} \quad (2.114)$$

$$= \frac{1}{\sqrt{2}} \begin{pmatrix} 1 \\ -i \end{pmatrix} = e^{-i\pi/4} \frac{1}{2} \begin{pmatrix} 1+i \\ 1-i \end{pmatrix} = e^{i\pi/4} |-y\rangle. \quad (2.115)$$

The pulse transforms the state  $|\alpha\rangle$  into the state  $|-y\rangle$  in other words it has rotated the polarization by  $\pi/2$  around the  $x$ -axis.

### 2.2.8.2 Pulse of general phase

To understand the significance of the phase of a pulse, consider a pulse exactly on resonance ( $\Omega^0 = 0$ ) with a general phase  $\phi_p$ . The rotating frame spin Hamiltonian is:

$$\tilde{\hat{H}} = \omega_{\text{nut}} (\hat{I}_x \cos \phi_p + \hat{I}_y \sin \phi_p), \quad (2.116)$$

from this, one can see that the effect of the phase shift is to change the axis about which the spin polarizations rotate. The rotation axis is still in the  $xy$ -plane but forms an angle,  $\phi_p$ , with the  $x$  axis. Therefore, a pulse with a phase of  $\pi/2$  rotates the spin polarization around the  $y$ -axis and a phase of  $\pi$  rotates the polarization around the  $-x$ -axis and so on.

The propagator for an on resonance pulse with phase  $\phi_p$  is given by:

$$\hat{R}_{\phi_p}(\theta) = \exp\{-i\omega_{\text{nut}}\tau(\hat{I}_x \cos \phi_p + \hat{I}_y \sin \phi_p)\} \quad (2.117)$$

$$= \exp\{-i\theta(\hat{I}_x \cos \phi_p + \hat{I}_y \sin \phi_p)\}, \quad (2.118)$$

this can be rewritten using rotation operators:

$$\hat{R}_{\phi_p}(\theta) = \hat{R}_z(\phi_p) \hat{R}_x(\theta) \hat{R}_z(-\phi_p). \quad (2.119)$$

The matrix representation can be obtained by multiplying together the matrix representations of the rotation operators from Eqn. 2.46:

$$\hat{R}_{\phi_p}(\theta) = \begin{pmatrix} \cos \frac{1}{2}\theta & -i \sin \frac{1}{2}(\theta) e^{-i\phi_p} \\ -i \sin \frac{1}{2}(\theta) e^{+i\phi_p} & \cos \frac{1}{2}\theta \end{pmatrix}. \quad (2.120)$$

### 2.2.8.3 Off-resonance effects

In general, it is not always possible to ensure exact resonance for all spins at the same time, so the condition  $\Omega^0 = 0$  cannot always be satisfied. Consider the case when  $\Omega^0 \neq 0$ , by examining the spin Hamiltonian during a rectangular pulse where:

$$\hat{H} = \Omega^0 \hat{I}_z + \omega_{\text{nut}} (\hat{I}_x \cos \phi_p + \hat{I}_y \sin \phi_p). \quad (2.121)$$

The rotation axis of the spin polarization now has a  $z$ -component as well as an  $x$ - and  $y$ -component. The axis is therefore tilted out of the  $xy$ -plane.

The rotating frame spin Hamiltonian for an off-resonance pulse may be written as:

$$\hat{H} = \boldsymbol{\omega}_{\text{eff}} \cdot \hat{\mathbf{I}}, \quad (2.122)$$

where  $\boldsymbol{\omega}_{\text{eff}}$  is the effective rotation axis, given by:

$$\boldsymbol{\omega}_{\text{eff}} = \omega_{\text{eff}} \{ \mathbf{e}'_x \sin \beta_p \cos \phi_p + \mathbf{e}'_y \sin \beta_p \sin \phi_p + \mathbf{e}'_z \cos \beta_p \}, \quad (2.123)$$

and  $\{\mathbf{e}'_x, \mathbf{e}'_y, \mathbf{e}'_z\}$  are the rotating reference frame axes. The vector operator  $\hat{\mathbf{I}}$  is defined as:

$$\hat{\mathbf{I}} = \mathbf{e}'_x \hat{I}_x + \mathbf{e}'_y \hat{I}_y + \mathbf{e}'_z \hat{I}_z. \quad (2.124)$$

The tilt of the rotation axis away from the  $z$ -axis is:

$$\beta_p = \arctan\left(\frac{\omega_{\text{nut}}}{\Omega^0}\right), \quad (2.125)$$

the magnitude of the rotation frequency around the tilted axis is given by:

$$\omega_{\text{eff}} = \{(\omega_{\text{nut}})^2 + (\Omega^0)^2\}^{1/2}, \quad (2.126)$$

Using these parameters the rotating frame spin Hamiltonian may be written as:

$$\hat{H} = \omega_{\text{eff}} \hat{R}_z(\phi_p) \hat{R}_y(\beta_p) \hat{I}_z \hat{R}_y(-\beta_p) \hat{R}_z(-\phi_p). \quad (2.127)$$

The rotating-frame spin states before and after the pulse are related through:

$$|\tilde{\psi}\rangle_2 = \hat{R}_{\text{off}} |\tilde{\psi}\rangle_1, \quad (2.128)$$

where  $\hat{R}_{\text{off}}$  is:

$$\hat{R}_{\text{off}} = \hat{R}_z(\phi_p) \hat{R}_y(\beta_p) \hat{R}_z(\omega_{\text{eff}}\tau) \hat{R}_y(-\beta_p) \hat{R}_z(-\phi_p). \quad (2.129)$$

### 2.2.9 The Density operator revisited

Usually in NMR there are  $> 10^{20}$  spins in the sample, the density operator becomes more advantageous here as mentioned it contains information about the entire spin ensemble. Normally, there is only a small population difference between  $\alpha$  and  $\beta$  governed by the Boltzmann distribution, so for a general polarization level,  $p$ , the density operator can be written as:

$$\hat{\rho} = \frac{1}{2} \begin{pmatrix} 1+p & 0 \\ 0 & 1-p \end{pmatrix}, \quad (2.130)$$

using the definition given in Eqn. 2.30 the density operator can be re-written as

$$\hat{\rho} = \frac{1}{2} \hat{\mathbb{1}} + \frac{1}{2} p \hat{I}_z, \quad (2.131)$$

$\hat{\mathbb{1}}$  is identity matrix and corresponds to no population difference between  $|\alpha\rangle$  and  $|\beta\rangle$ .

$\hat{\mathbb{1}}$  is unaffected by rotations so can be ignored in the context of NMR and it becomes

$$\hat{\rho} = \frac{1}{2} p \hat{I}_z, \quad (2.132)$$

to describe the  $z$  magnetization of our sample. If the system is at thermal equilibrium, then  $p$  is equal to the Boltzmann factor defined as:

$$\mathbb{B} = \frac{\hbar\gamma B_0}{k_b T}. \quad (2.133)$$

In NMR the dynamics of a system can be described using the density operator evolution, rather than the evolution of the states using

$$\frac{\partial}{\partial t} |\psi\rangle = -i \hat{H} |\psi\rangle \quad (2.134)$$

$$\frac{\partial}{\partial t} \langle \psi | = i \langle \psi | \hat{H}, \quad (2.135)$$

Using this, the following derivation can be made [83]:

$$\frac{\partial}{\partial t} \hat{\rho} = \frac{\partial}{\partial t} [|\psi\rangle \langle \psi|] \quad (2.136)$$

$$= \left[ \frac{\partial}{\partial t} |\psi\rangle \right] \langle \psi | + |\psi\rangle \left[ \frac{\partial}{\partial t} \langle \psi | \right] \quad (2.137)$$

$$= -i \hat{H} |\psi\rangle \langle \psi| + i |\psi\rangle \langle \psi| \hat{H}, \quad (2.138)$$

to give the relationship

$$\frac{\partial}{\partial t} \hat{\rho} = -i [\hat{H}, \hat{\rho}]. \quad (2.139)$$

This is called the Liouville von Neumann equation.

The calculation of the response of the spin ensemble to r.f. pulses can be done, given the general rotating frame as before, the rotating frame density operator is given by:

$$\hat{\rho} = \overline{|\tilde{\psi}\rangle\langle\tilde{\psi}|}. \quad (2.140)$$

The rotating frame and fixed frame populations and coherences are related by:

$$\tilde{\rho}_\alpha = \rho_\alpha \quad (2.141)$$

$$\tilde{\rho}_- = \rho_- \exp\{-i\Phi(t)\} \quad (2.142)$$

where

$$\Phi(t) = \omega_{\text{ref}}t + \phi_{\text{ref}}, \quad (2.143)$$

the populations remain the same and the coherences are linked through a time dependant phase factor.

### 2.2.9.1 Magnetization vector

The state of a single spin-1/2 can be represented by an arrow indicating the direction of well-defined angular momentum and the response measured by rotating the arrow around the different axes in three dimensional space. Then similarly an ensemble of isolated spins-1/2 can be represented as a magnetization vector,  $\mathbf{M}$ , indicating the magnitude and direction of the net magnetization. The dynamics of the ensemble corresponds to the motion of the magnetization vector.

The magnetization vector has three Cartesian components:

$$\mathbf{M} = M_x \mathbf{e}_x + M_y \mathbf{e}_y + M_z \mathbf{e}_z. \quad (2.144)$$

The longitudinal component is related to the population difference between states:

$$M_z = 2\mathbb{B}^{-1}(\rho_\alpha - \rho_\beta). \quad (2.145)$$

The transverse magnetization components  $M_x$  and  $M_y$  are related to the (-1)-quantum coherence between the states:

$$M_x = -4\mathbb{B}^{-1}Re\{\rho_-\} \quad (2.146)$$

$$M_y = -4\mathbb{B}^{-1}Im\{\rho_-\}. \quad (2.147)$$

These are chosen so that thermal equilibrium magnetization is a unit vector along the  $z$ -axis:

$$\mathbf{M}^{\text{eq}} = \mathbf{e}_z. \quad (2.148)$$

With these, the density operator may be written as:

$$\hat{\rho} = \frac{1}{2}\mathbb{1} + \frac{1}{2}\mathbb{B}\mathbf{M} \cdot \hat{\mathbf{I}} \quad (2.149)$$

$$= \frac{1}{2}\mathbb{1} + \frac{1}{2}\mathbb{B}(M_x\hat{I}_x + M_y\hat{I}_y + M_z\hat{I}_z). \quad (2.150)$$

The populations and coherences can be represented in terms of magnetization:

$$\rho_\alpha = \frac{1}{2} + \frac{1}{4}\mathbb{B}M_z \quad \rho_\beta = \frac{1}{2} - \frac{1}{4}\mathbb{B}M_z \quad (2.151)$$

$$\rho_+ = \frac{1}{4}\mathbb{B}(M_x - iM_y) \quad \rho_- = \frac{1}{4}\mathbb{B}(M_x + iM_y). \quad (2.152)$$

### 2.2.9.2 Density operator under pulses

The sandwich equation can be used to calculate the effect of a strong  $(\pi/2)_x$  pulse on an ensemble of spins-1/2 at thermal equilibrium. Before the pulse, the spin density operator is

$$\hat{\rho}_1 = \frac{1}{2}\mathbb{1} + \frac{1}{2}\mathbb{B}\hat{I}_z, \quad (2.153)$$

after the pulse the density operator is

$$\hat{\rho}_2 = \hat{R}_x(\pi/2)\hat{\rho}_1\hat{R}_x(-\pi/2) = \frac{1}{2}\hat{R}_x(\pi/2)\mathbb{1}\hat{R}_x(-\pi/2) + \frac{1}{2}\mathbb{B}\hat{R}_x(\pi/2)\hat{I}_z\hat{R}_x(-\pi/2) \quad (2.154)$$

$$= \frac{1}{2}\mathbb{1} + \frac{1}{2}\mathbb{B}\hat{R}_x(\pi/2)\hat{I}_z\hat{R}_x(-\pi/2), \quad (2.155)$$

since the identity matrix,  $\mathbb{1}$  is invariant under rotations. The last term can be calculated using the sandwich relationship:

$$\hat{R}_x(\pi/2)\hat{I}_z\hat{R}_x(-\pi/2) = -\hat{I}_y, \quad (2.156)$$

therefore

$$\hat{\rho}_2 = \frac{1}{2}\mathbb{1} - \frac{1}{2}\mathbb{B}\hat{I}_y. \quad (2.157)$$

In terms of the magnetization vector, this is equivalent to rotating the magnetization from the  $z$ -axis to the  $-y$ -axis.

$$\mathbf{M}_1 = \mathbf{e}_z \xrightarrow{(\pi/2)_x} \mathbf{M}_2 = -\mathbf{e}_y. \quad (2.158)$$

To determine what happens to the populations and coherences, consider the pulse effects in terms of the matrix representation:

$$\hat{\rho}_1 = \begin{pmatrix} \frac{1}{2} + \frac{1}{4}\mathbb{B} & 0 \\ 0 & \frac{1}{2} - \frac{1}{4}\mathbb{B} \end{pmatrix} \xrightarrow{(\pi/2)_x} \begin{pmatrix} \frac{1}{2} & -\frac{1}{4i}\mathbb{B} \\ \frac{1}{4i}\mathbb{B} & \frac{1}{2} \end{pmatrix}, \quad (2.159)$$

the pulse accomplishes two things, firstly, the pulse equalises the populations of the two states and secondly, converts the population difference into coherences.

### 2.2.10 Free evolution with relaxation

So far, the Hamiltonian and density operator have only been discussed before, during, and immediately after an r.f. pulse. This picture is insufficient to describe what one observes experimentally. In terms of populations and coherences, experimentally it is found that the populations are not time independent, but gradually drift towards their thermal equilibrium values and that the coherences do not last forever but gradually decay to zero.

For populations and coherences there are two forms of relaxation,  $T_1$  and  $T_2$ .  $T_1$  is the longitudinal relaxation time constant and  $T_2$  is the transverse relaxation time constant. The difference between them is demonstrated in Fig. 2.7. Classically  $T_1$  is the rate constant that governs the return of magnetization to the  $z$ -axis from the  $xy$ -plane.  $T_2$  on the other hand is the time constant that governs the return of magnetization to equilibrium in the  $xy$ -plane. When talking in terms of the density operator it is said that " $T_1$ " is the relaxation rate constant for populations, and ' $T_2$ ' is the relaxation rate constant coherences. But this is incompatible with the classical description of NMR.

The Bloch equations are used to describe how the magnetization vectors change in time [84]:

$$\frac{dM_x(t)}{dt} = \gamma(M_y(t)B_z(t) - M_z(t)B_y(t)) - \frac{M_x(t)}{T_2} \quad (2.160)$$

$$\frac{dM_y(t)}{dt} = \gamma(M_z(t)B_x(t) - M_x(t)B_z(t)) - \frac{M_y(t)}{T_2} \quad (2.161)$$

$$\frac{dM_z(t)}{dt} = \gamma(M_x(t)B_y(t) - M_y(t)B_x(t)) - \frac{M_z(t) - M_0}{T_1}. \quad (2.162)$$

#### 2.2.10.1 Transverse relaxation

The coherences decaying to zero is ensured in the equations by introducing an exponential decay term. between time points 2, immediately after an r.f. pulse ( $t=0$ ), and 3 ( $t>0$ ) with some delay  $\tau$  the equations for the rotating frame coherences are:

$$\rho_-(3) = \rho_-(2)\exp\{(i\Omega^0 - \lambda)\tau\} \quad (2.163)$$

$$\rho_+(3) = \rho_+(2)\exp\{(-i\Omega^0 - \lambda)\tau\}, \quad (2.164)$$

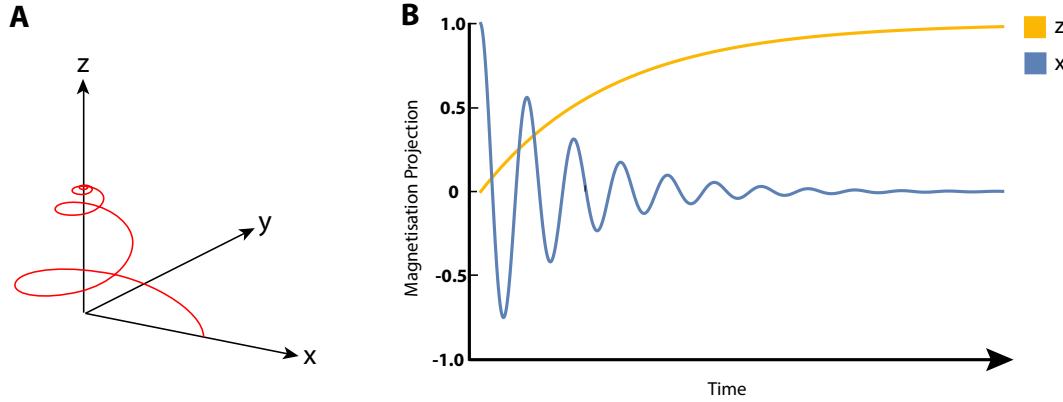


FIGURE 2.7: A) a magnetization vector precesses in the  $xy$ -plane, eventually returning to equilibrium. B) A plot of the magnetization along  $z$ -axis (yellow) and the  $x$ -axis (blue) during the relaxation.

where the damping rate constant  $\lambda$  is given by the inverse of the transverse relaxation time constant  $T_2$ :

$$\lambda = T_2^{-1}. \quad (2.165)$$

These equations for coherences correspond to the following substitution rules for the transverse spin angular momentum operators:

$$\hat{I}_x \rightarrow (\hat{I}_x \cos \Omega^0 \tau + \hat{I}_y \sin \Omega^0 \tau) e^{-\lambda \tau} \quad (2.166)$$

$$\hat{I}_y \rightarrow (\hat{I}_y \cos \Omega^0 \tau - \hat{I}_x \sin \Omega^0 \tau) e^{-\lambda \tau}. \quad (2.167)$$

For the transverse components of the magnetization vector, the equations are:

$$M_x(3) = M_x(2) \cos \Omega^0 \tau + M_y(2) \sin \Omega^0 \tau e^{-\lambda \tau} \quad (2.168)$$

$$M_y(3) = M_y(2) \cos \Omega^0 \tau - M_x(2) \sin \Omega^0 \tau e^{-\lambda \tau}. \quad (2.169)$$

Physically, coherence requires a consistent polarization direction of the spin ensemble. On average all spins experience the same field in a liquid due to motional averaging, however, at any particular instant in time the field are slightly different for different spins locally which cause a gradual loss of synchronisation across the ensemble. Coherence decay does increase the entropy of the spin ensemble and is therefore irreversible.

### 2.2.10.2 Longitudinal relaxation

The equations of motion for the populations is a bit more complicated as the populations decay back to their thermal equilibrium values the equations for this are:

$$\rho_\alpha(3) = (\rho_\alpha(2) - \rho_\alpha^{eq})e^{-\tau/T_1} + \rho_\alpha^{eq} \quad (2.170)$$

$$\rho_\beta(3) = (\rho_\beta(2) - \rho_\beta^{eq})e^{-\tau/T_1} + \rho_\beta^{eq}, \quad (2.171)$$

where the thermal equilibrium populations are:

$$\rho_\alpha^{eq} = \frac{1}{2} + \frac{1}{4}\mathbb{B} \quad \rho_\beta^{eq} = \frac{1}{2} - \frac{1}{4}\mathbb{B}. \quad (2.172)$$

The equation of motion for the  $z$ -axis magnetization vector is:

$$M_z(3) = (M_z(2) - 1)e^{-\tau/T_1} + 1. \quad (2.173)$$

Longitudinal relaxation involves an energy exchange between the spin system and the molecular surroundings and is why it is often referred to as spin-lattice relaxation.

### 2.2.11 NMR signal and detection

In NMR the signal produced by the spins is inductively detected. The precessing transverse magnetization, created when an r.f. field is applied to the sample, induces a voltage, and therefore a current, in a coil that is placed near the sample.

In order to do this, consider a sample containing  $n_s$  number of non-interacting spins-1/2 which have a sample volume,  $V_s$ , and a concentration of spins,  $c_s = n_s/V_s$ . The total magnetic dipole moment operator in this case is:

$$\hat{\mu} = \hbar\gamma \sum_{k=1}^n \hat{\mathbf{I}}_k, \quad (2.174)$$

where  $\hat{\mathbf{I}}_k$  is the spin operator for a nucleus  $k$  such that:

$$\hat{\mathbf{I}}_k = (\hat{I}_{kx}\mathbf{e}_x + \hat{I}_{ky}\mathbf{e}_y + \hat{I}_{kz}\mathbf{e}_z). \quad (2.175)$$

The total nuclear magnetization of the sample is given by:

$$\mathbf{M} = \frac{\sum_{k=1}^n \hat{\mu}}{V_s} = \frac{c_s V_s \langle \bar{\mu} \rangle}{V_s} = c_s \langle \bar{\mu} \rangle, \quad (2.176)$$

where  $\langle \bar{\mu} \rangle$  is the ensemble average of the expectation value magnetic dipole moment.

This magnetization leads to the signal obtained in NMR, to find the relationship the principle of reciprocity is invoked [85]. Consider the induction field,  $\mathbf{B}_1$ , produced by a coil carrying unit current. For a magnetic dipole,  $\mathbf{m}$ , the induced emf is given by:

$$\xi = -\frac{\partial}{\partial t}\{\mathbf{B}_1 \cdot \mathbf{m}\}, \quad (2.177)$$

where  $\mathbf{B}_1$  is the field produced by the unit current in the coil at  $\mathbf{m}$ . It follows that for a sample, after being subjected to a  $(\pi/2)$  pulse, only the value of  $\mathbf{B}_1$  at all points within the sample is needed to be able to calculate the emf induced in the coil, if  $\mathbf{M}$  lies in the  $xy$ -plane:

$$\xi = -\int_{\text{sample}} \frac{\partial}{\partial t}\{\mathbf{B}_1 \cdot \mathbf{M}\} dV_s, \quad (2.178)$$

if  $\mathbf{B}_1$  is assumed to be homogeneous over the sample volume this gives:

$$\xi = \frac{\partial}{\partial t}\{\mathbf{B}_1 \cdot \mathbf{M}\} V_s, \quad (2.179)$$

Substitution of the result from Eqn. 2.176 gives

$$\xi = \frac{\partial}{\partial t}\{\mathbf{B}_1 \cdot \langle \bar{\mu} \rangle\} V_s c_s, \quad (2.180)$$

if the  $B_1$  coil is aligned along the  $x$ -axis, only the  $x$ -axis components contribute to the emf

$$\xi = \frac{\partial}{\partial t}\{B_{1x} \langle \bar{\mu}_x \rangle c_s\} V_s, \quad (2.181)$$

using Eqn. 2.174,  $\langle \hat{\mu}_x \rangle = \hbar\gamma\langle \hat{I}_x \rangle$  the emf becomes

$$\xi = \frac{\partial}{\partial t}\{B_{1x} \langle \hat{I}_x \rangle c_s\} V_s \hbar\gamma, \quad (2.182)$$

from 2.2.4, the ensemble average can be found using the density operator  $\langle \hat{I}_x \rangle = \text{Tr}\{\hat{\rho}\hat{I}_x\}$  so

$$\xi = \frac{\partial}{\partial t}\{B_{1x}[\text{Tr}\{\hat{\rho}\hat{I}_x\}] c_s\} V_s \hbar\gamma. \quad (2.183)$$

For a spin-1/2 nucleus this equation becomes:

$$\xi = \frac{\partial}{\partial t}\{B_{1x}[\rho_- + \rho_+]\} V_s c_s \hbar\gamma \frac{1}{2}, \quad (2.184)$$

if all terms apart from the coherences are considered time independent, the emf can be simplified for now as

$$\xi \sim \frac{\partial}{\partial t}\rho_-(t) + \frac{\partial}{\partial t}\rho_+(t), \quad (2.185)$$

using Eqn. 2.163

$$\rho_-(t) = \rho_-(0)\exp\{(i\omega^0 - \lambda)t\} \quad (2.186)$$

$$\rho_+(t) = \rho_+(0)\exp\{(-i\omega^0 - \lambda)t\}, \quad (2.187)$$

the emf becomes

$$\xi \sim (i\omega^0 \rho_- - i\omega^0 \rho_+), \quad (2.188)$$

the signal that one obtains in an NMR experiment is proportional to the emf induced in the pick-up coil this is denoted  $s_{\text{FID}}$  and is given by:

$$s_{\text{FID}} \sim (i\omega^0 \rho_- - i\omega^0 \rho_+) \frac{1}{2} \frac{B_1}{i} \gamma \hbar c_s V_s. \quad (2.189)$$

### 2.2.11.1 Quadrature detection

This 'raw' NMR signal typically oscillates at many hundred megahertz which is too fast for conversion to a digital signal that can be interpreted on a computer. Therefore, it is necessary to down convert the frequency of the NMR signals. This is accomplished by subtracting a frequency that is close to the Larmor frequency, typically, the frequency subtracted is set somewhere in the middle of the spectrum. This frequency, generated locally by an r.f. synthesiser, is called the reference frequency. It is denoted  $\omega_{\text{ref}}$  and has an associated phase  $\phi_{\text{ref}}$

This process of subtraction is carried out by multiplying together the two input signals in a mixer. The signal from the FID is multiplied by the receiver reference signal:

$$s_{\text{rec}}(t) = \cos(\omega_{\text{ref}} t + \phi_{\text{rec}}), \quad (2.190)$$

the reference signal is split into two parts  $A$  and  $B$  where  $A$  has the same form as above and  $B$  is given an additional phase shift so:

$$s_{\text{rec}}^A(t) = \cos(\omega_{\text{ref}} t + \phi_{\text{rec}}) \quad (2.191)$$

$$s_{\text{rec}}^B(t) = \cos(\omega_{\text{ref}} t + \phi_{\text{rec}} + \pi/2). \quad (2.192)$$

The signal after mixing with  $A$  is:

$$s_{\text{FID}}(t)s_{\text{rec}}^A(t) = (i\omega^0 \rho_-(t) - i\omega^0 \rho_+(t)) \cos(\omega_{\text{ref}} t + \phi_{\text{rec}}), \quad (2.193)$$

which can be evaluated as

$$s_{\text{FID}}(t)s_{\text{rec}}^A(t) = \frac{1}{2}i\rho_-(0)\exp\{i[(\omega^0 + \omega_{\text{ref}})t + \phi_{\text{rec}}]\}e^{-\lambda t} \quad (2.194)$$

$$+ \frac{1}{2}i\rho_-(0)\exp\{i[(\omega^0 - \omega_{\text{ref}})t - \phi_{\text{rec}}]\}e^{-\lambda t} \quad (2.195)$$

$$- \frac{1}{2}i\rho_+(0)\exp\{i[-(\omega^0 - \omega_{\text{ref}})t + \phi_{\text{rec}}]\}e^{-\lambda t} \quad (2.196)$$

$$+ \frac{1}{2}i\rho_+(0)\exp\{i[-(\omega^0 + \omega_{\text{ref}})t - \phi_{\text{rec}}]\}e^{-\lambda t}. \quad (2.197)$$

This rather complicated signal is now passed through a low pass r.f. filter which removes the high frequency components, this removes the components oscillating at  $\omega^0 + \omega_{\text{ref}}$  and retains the low frequency components  $\Omega^0 = \omega^0 - \omega_{\text{ref}}$ . The signal  $s_A(t)$  emerging from the filter is

$$s_A = + \frac{1}{2}i\rho_-(0)\exp\{i(\Omega^0 t - \phi_{\text{rec}})\}e^{-\lambda t} \quad (2.198)$$

$$- \frac{1}{2}i\rho_+(0)\exp\{i(-\Omega^0 t + \phi_{\text{rec}})\}e^{-\lambda t}, \quad (2.199)$$

due to the relationship between laboratory and rotating-frame coherences from Eqn. 2.141 this can be written as

$$s_A = + \frac{1}{2}i\tilde{\rho}_-(0)\exp\{i(\Omega^0 t - \phi_{\text{rec}} + \phi_{\text{ref}})\}e^{-\lambda t} \quad (2.200)$$

$$- \frac{1}{2}i\tilde{\rho}_+(0)\exp\{i(-\Omega^0 t + \phi_{\text{rec}} - \phi_{\text{ref}})\}e^{-\lambda t}, \quad (2.201)$$

where  $\phi_{\text{ref}}$  represents the angle of the rotating frame with respect to the laboratory frame at time  $t = 0$ . The equations for the precession in the rotating frame (Eqn. 2.163) allow for the simplification

$$s_A = + \frac{1}{2}i\tilde{\rho}_-(t)\exp\{-i(\phi_{\text{rec}} - \phi_{\text{ref}})\} - \frac{1}{2}i\tilde{\rho}_+(t)\exp\{i(\phi_{\text{rec}} - \phi_{\text{ref}})\}. \quad (2.202)$$

The same arguments can be repeated for the phase shifted signal path  $B$

$$s_B = + \frac{1}{2}\tilde{\rho}_-(t)\exp\{-i(\phi_{\text{rec}} - \phi_{\text{ref}})\} + \frac{1}{2}\tilde{\rho}_+(t)\exp\{i(\phi_{\text{rec}} - \phi_{\text{ref}})\}. \quad (2.203)$$

These signals are treated as two components of one complex signal:

$$s(t) = s_A(t) + is_B(t), \quad (2.204)$$

which evaluates to

$$s(t) \sim i\tilde{\rho}_-(t)\exp\{-i(\phi_{\text{rec}} - \phi_{\text{ref}})\}. \quad (2.205)$$

Which contains contributions from the rotating frame  $(-1)$ -quantum coherences. The  $(+1)$ -quantum coherences have disappeared however, the contribution is equal to the  $(-1)$ -quantum coherence so a factor two is included the frame phase shift as well as

other sources of constant shifts from instrumentation are corrected in post-processing so the quadrature signal can be expressed as:

$$s(t) \sim 2i\tilde{\rho}_-(t)\exp\{-i\phi_{\text{rec}}\}. \quad (2.206)$$

There are some time independent variables from the original expression of  $s_{\text{FID}}$  which can now be included, and neglecting the noise and gain acquired from quadrature demodulation, these signals are:

$$s(t) = 2i\omega^0 \frac{1}{2} \frac{B_{1x}}{i_c} \gamma \hbar c_s V_s \tilde{\rho}_-(t) \exp\{-i\phi_{\text{rec}}\} \quad (2.207)$$

$$s(t) = i\omega^0 \frac{B_{1x}}{i_c} \gamma \hbar c_s V_s \tilde{\rho}_-(t) \exp\{-i\phi_{\text{rec}}\}, \quad (2.208)$$

where  $\omega^0$  is the Larmor frequency,  $B_{1x}/i_c$  is the coil sensitivity,  $\gamma$  is the gyromagnetic ratio,  $\hbar$  is the reduced Planck's constant, the term  $c_s V_s$  is the number of spins in the sample.

### 2.2.11.2 Signal after a pulse

The signal dependence can be seen more clearly if one gets more quantitative, to do this, consider a  $(\pi/2)_x$  pulse with receiver phase,  $\phi_{\text{rec}} = 0$ , for brevity the tilde will be dropped as only the rotating frame will be considered. In order to calculate the  $(-1)$ -quantum coherence, the density operator must be calculated first. The rotating frame density operator at equilibrium is

$$\hat{\rho}^{eq} = \frac{1}{2} \mathbb{1} + \frac{1}{2} \mathbb{B} \hat{I}_z, \quad (2.209)$$

immediately after the pulse at  $t = 0$  the density operator is

$$\hat{\rho}(0) = \frac{1}{2} \mathbb{1} - \frac{1}{2} \mathbb{B} \hat{I}_y, \quad (2.210)$$

this can be written in terms of the shift and projection operators:

$$\hat{\rho}(0) = \frac{1}{2} \hat{I}^\alpha + \frac{1}{2} \hat{I}^\beta - \frac{1}{4i} \mathbb{B} \hat{I}^+ + \frac{1}{4i} \mathbb{B} \hat{I}^-, \quad (2.211)$$

the  $(-1)$ -quantum coherence is equal to the coefficient of the  $\hat{I}^-$  operator

$$\rho_-(0) = \frac{1}{4i} \mathbb{B}, \quad (2.212)$$

the coherence at a time  $t > 0$  is given by:

$$\rho_-(t) = \rho_-(0) \exp\{(i\Omega^0 - \lambda)t\}. \quad (2.213)$$

By combining this with the signal equation:

$$s(t) = a \exp\{(i\Omega^0 - \lambda)t\}, \quad (2.214)$$

where the signal amplitude  $a$  is

$$a = i\omega^0 \frac{B_{1x}}{i_c} \gamma \hbar c_s V_s \rho_-(0) \exp\{-i\phi_{\text{rec}}\}, \quad (2.215)$$

and in the case of the  $(\pi/2)_x$  pulse

$$a = i\omega^0 \frac{B_{1x}}{i_c} \gamma \hbar c_s V_s \frac{1}{4i} \mathbb{B}, \quad (2.216)$$

collecting like terms and expanding  $\mathbb{B}$  gives

$$a = \frac{1}{4} \frac{B_{1x}}{i_c} \gamma^3 \hbar^2 B_0^2 \frac{n_s}{k_b T}, \quad (2.217)$$

where  $n_s$  is the number of spins in the sample. This relationship makes sense intuitively as increasing the number of spins in the sample leads to an increase in single amplitude as does increasing the coil sensitivity.

### 2.2.11.3 Chemical Shift and J-coupling

In a molecule, nuclei are surrounded by clouds of electrons which can shield, or de-shield, it from the effects of the external field  $B_0$ .

The chemical shielding factor,  $\sigma$ , shifts the resonance frequency of the nuclear spin. It can now include it in Eqn. 2.74:

$$\omega_j^0 = -\gamma_j B_0 (1 - \sigma), \quad (2.218)$$

this chemical shielding is specific to each nuclei position in the molecule. It is possible for two or more nuclei to share the same factor. These are referred to as being 'chemically equivalent'.

The shielding is often around  $10^{-6}$  for  ${}^1\text{H}$ , when plotting and examining spectra it would not be useful to use absolute frequencies, as discussed they are regularly in the hundreds of MHz, whereas the differences in peaks might only be kHz or less. To combat this a relative frequency scale is used called chemical shift,  $\delta$ , defined as:

$$\delta = \frac{\omega_j - \omega_j^{\text{ref}}}{\omega_j^{\text{ref}}}, \quad (2.219)$$

where  $\omega_j$  is the precession frequency of the nucleus of interest, and  $\omega_j^{\text{ref}}$  is the precession frequency of a reference nucleus.  $\delta$  is a dimensionless number, unaffected by magnetic

field strength, it often small compared to the size of the field and is reported in parts per million (ppm).

In addition to the external  $B_0$  field, the nuclear spins are also affected by the magnetic fields generated by neighbouring spins. These magnetic fields are mediated by the electrons in the chemical bonds. This is referred to as spin-spin coupling or  $J$ -coupling and gives rise to peak splittings in spectra. These splittings, and therefore the values of  $J$ -couplings, range from a few Hz to a thousand Hz typically. These become important when considering the Hamiltonian of a multi-spin system but is not discussed in this work.

Both of these,  $\sigma$  and  $J$ -couplings, are tensors this means they depend on the orientation of the molecule and the spin with respect to the magnetic field. In liquids, however, tumble rapidly compared to the timescale of an NMR experiment. This averages the interactions resulting in a scalar quantity for each.

There are additional effects the nuclear spins experience, for example, dipole-dipole coupling which is a through space spin-spin coupling, and quadrupole coupling where there are spins with  $>1/2$  values however, these are not relevant to this work.

## 2.3 Micro-NMR

All NMR experiments depend on two performance metrics: sensitivity and resolution. Sensitivity refers to the minimum number of spins needed to give a signal clearly above the noise, whilst resolution quantifies how well different species in the sample can be differentiated. These two properties are often linked, by selecting a smaller sample it is possible to enhance resolution by detecting a smaller portion of spins in the sample but this compromises sensitivity as the number of spins become more limited.

In NMR, nuclear spin state coherences have long lifetimes that are governed by the decay constant,  $T_2$ , which is typically seconds, but in some cases can be minutes long. These long lifetimes contribute to extremely narrow lines in the spectrum, with resolutions of one part per billion regularly achieved in commercial systems.

### 2.3.1 Sensitivity

#### 2.3.1.1 Signal to noise ratio

Sensitivity in NMR at thermal equilibrium is always in short supply. In an NMR experiment, the signal amplitude after a  $\pi/2$  pulse at thermal equilibrium,  $a$ , can be expressed as:

$$a = \frac{1}{4} \frac{B_{1x}}{i_c} \gamma^3 \hbar^2 B_0^2 \frac{n_s}{k_b T}, \quad (2.220)$$

where,  $B_{1x}/i_c$  is the coil sensitivity,  $\gamma$  is the gyromagnetic ratio of the nucleus,  $\hbar = h/2\pi$ ,  $B_0$  is the magnetic field,  $n_s$  is the number of spins in the sample,  $k_B$  is the Boltzmann constant and  $T$  is the absolute temperature. The amplitude of the signal depends on the Boltzmann distribution of population which at room temperature is on the order of  $10^{-25}$ J which is much lower than the thermal energy of the system. From the equation, increasing  $B_0$  would seem a valid strategy and comparatively it can be, increasing from 14.1T to 23.5T can almost triple the signal amplitude, however even at 23.5T there is only a factor of  $6 \times 10^{-6}$  in population difference. It's this very small value that is responsible for the low sensitivity of NMR compared to other techniques.

As mentioned, detection in NMR is typically done through the induction of a voltage in a coil that's close to the precessing nuclear spins, this is usually referred to as the sample coil. Unfortunately, this coil also brings with it a type of interference, noise, analogous to the 'hiss' in the background of radio it is produced mainly from thermal motion of electrons in the sample coil with some contribution from thermal motion of ions in solution. The signal to noise ratio, SNR, is an important factor in NMR experiments if its too low the signal will never be seen.

The SNR was formulated by Abragam[86] and the analysis extended by Hoult and Richards[85] and is defined as the peak signal divided by the root mean square

(rms) noise. By including the amplitude from Eqn. 2.220 and using the *Rayleigh-Jeans approximation* for the noise the SNR is:

$$\text{SNR} = \frac{k_0 \frac{1}{4} \frac{B_{1x}}{i_c} \gamma^3 \hbar^2 B_0^2 \frac{n_s}{k_b T_s}}{F \sqrt{4k_b T_c R_{\text{noise}}} \Delta f}, \quad (2.221)$$

where  $k_0$  is a factor that accounts for inhomogeneity in the  $B_1$  field,  $T_s$  is the temperature of the sample, and  $n_s$  is the number of spins in the sample. The factor  $B_1/i_c$  the magnetic field from the coil per unit current is defined as the coil sensitivity. The denominator is the noise determined by the noise factor from the spectrometer ( $F$ ) and the dissipative losses,  $R_{\text{noise}}$ , of the coil, circuit and sample for the spectral bandwidth  $\Delta f$ .  $T_c$  is the absolute temperature of the coil, and  $k_b$  is the Boltzmann constant.

In the same paper, Hoult and Richards introduced the principle of reciprocity for calculating the sensitivity of the RF coil, This states that the signal received from a sample by a coil is proportional to the magnetic field which would have been created in the sample if unit current were passed through the coil. Therefore the SNR is directly proportional to the sensitivity of the coil,  $B_1/i_c$ . This can be seen if an effective sample volume is defined, that is the volume in which  $B_1$  is within 10% of the maximum value at the centre of the coil. The SNR is given by a more simple expression[87]:

$$SNR = C \frac{B_1 n_s}{i_c \sqrt{R \Delta f}}, \quad (2.222)$$

where  $n_s$  is the number of spins in located within an effective volume. For protons at 600MHz the constant,  $C$  equals  $1.4 \times 10^{-11}$  in SI units ( $B_0 = 14.1\text{T}$ ,  $T = 300\text{K}$ ,  $\gamma = 0.2675 \times 10^9 \text{ radT}^{-1}\text{s}^{-1}$ ,  $I = 1/2$  and  $F = 1$  assuming negligible noise from the spectrometer.)

From the simple expression it becomes clear that the way to improve SNR is to increase the filling factor, maximise coil sensitivity,  $B_1/i_c$ , and minimise the total resistance. The filling factor,  $\alpha_F$  is given by:

$$\alpha_F = \frac{\int B_1^2 \rho(r) dV}{\int B_1^2 dV}, \quad (2.223)$$

where the function  $\rho$  is unity in the sample area, and zero elsewhere. For a long solenoid coil with the interior space filled with sample,  $\alpha_F = 1/2$ .

Increasing the filling factor and maximising maximise coil sensitivity, can be solved by decreasing the size of the detector. The third, minimising resistance in the coil, can be tackled by commercially available cryo-probes where the coil is cooled with a stream of He gas to 20K this reduces the thermal noise from the source and can increase SNR by a factor of four.

To see how size of coil affects SNR, consider an RF helical coil. An idealised coil is a cylindrical shell with uniform current density. The RF current penetrates to a frequency specific depth  $\delta_{\text{RF}}$ . For copper at 600 MHz and room temperature  $\delta_{\text{RF}} = 2.7 \mu\text{m}$ . The centre field is given by:

$$\frac{B_1}{i_c} = \frac{\mu_0}{\sqrt{l^2 + d^2}}. \quad (2.224)$$

Resistance is:

$$R = \rho_r \frac{\pi d}{l}, \quad (2.225)$$

with  $l$ , the height of the copper cylinder,  $d$  the diameter and  $\rho_r$  the resistivity. Optimum coil sensitivity is given by  $d/l = 1$  in this case the signal to noise is:

$$SNR = 0.9 \times 10^{-16} \frac{n_s}{d \sqrt{\Delta f}}, \quad (2.226)$$

for a fixed number of spins the SNR scales with  $1/d$  as predicted by [85]

### 2.3.2 Signal Averaging

In NMR, the total signal that emerges from the probe contains signal from the sample under observation as well as uncontrolled random signals called noise. In NMR spectroscopy, the most dominant source of noise comes from the thermal motions of the electrons in the receiver coil, called thermal noise. In order for the signal that originated from the sample to rise above the noise, signal averaging must be employed. This works as the sum of two identical experiments is twice the signal of the original individual experiment:

$$s_{\text{NMR}}(1+2) = s_{\text{NMR}}(1) + s_{\text{NMR}}(2) = 2s_{\text{NMR}}(1). \quad (2.227)$$

The key, is that this relationship does not apply equally to the noise, as it is random. A suitable definition of the noise amplitude in a single experiment is given by the root mean square (RMS) noise defined as:

$$\sigma_{\text{noise}} = \langle s_{\text{noise}}(1)^2 \rangle^{1/2}, \quad (2.228)$$

where the angle bracket indicates an average over all sampling points.

As in 2.2.11, the signal generated by the noise is proportional to the noise voltage in the coil such that:

$$\langle s_{\text{noise}}(1)^2 \rangle \sim (\langle \xi_n^2 \rangle), \quad (2.229)$$

where  $\langle \xi_n^2 \rangle$  is the mean square emf produced in the coil by thermal noise, and  $F$  is the noise factor from the spectrometer.

This mean square emf is derived from statistical mechanics and can be expressed as [88, 89]:

$$\langle \xi_n^2 \rangle = 4k_b T_C R_{\text{noise}} \Delta f. \quad (2.230)$$

Including a factor for the noise from the spectrometer,  $F$ ,  $\sigma_{\text{noise}}$  can be expressed quantitatively as:

$$\sigma_{\text{noise}} = F \sqrt{4k_b T_C R_{\text{noise}} \Delta f}, \quad (2.231)$$

which is equal to the denominator for the SNR from Eqn. 2.221.

The RMS noise is the same for two experiments assuming the noise is stationary i.e. the noise does not change from one experiment to the next. However, this does not imply that the noise from two experiments has twice the value. Summed over the two experiments the RMS noise takes the value:

$$\sigma_{\text{noise}}(1+2) \cong \sqrt{2}\sigma_{\text{noise}}(1). \quad (2.232)$$

Since the noise over two experiments increases by  $\sqrt{2}$  but the signal doubles. Therefore the signal to noise ratio over two experiments can be written as:

$$\text{SNR}(1+2) = \sqrt{2} \frac{s_{\text{NMR}}(1)}{\sigma_{\text{noise}}(1)}. \quad (2.233)$$

This can be extended to show the signal-to-noise over  $N$  transients is a factor  $\sqrt{N}$  larger than the signal for a single transient. So by signal averaging over many scans the SNR can be increased.

In principle, this allows NMR signals that have a SNR less than one to be 'pulled out' of the noise. In reality, this is time consuming as in order to repeat an experiment precisely it is essential to allow the spin system to reach thermal equilibrium again. The different NMR experiments must therefore be separated by an interval many times longer than  $T_1$ , which in some case can be several seconds. For example, if the SNR of the first experiment is 0.1 clearly the signal will be buried in the noise. The SNR may be changed to 10:1 by signal averaging over 10,000 scans. If each scan takes 1 second this amounts to 3 hours of instrument time which is long but acceptable. However, if the SNR is 0.01 then it follows that 300 hours would now be needed which is not feasible.

In order for smaller signals to be detected, the amount of signal i.e. the amount of polarization in the sample, needs to be increased this can be done by preparing the sample in a specific way and is referred to as 'hyperpolarization'.

### 2.3.3 Limit of Detection

The signal to noise ratio can be found in the time or frequency domain. In the time domain the root mean square noise,  $\sigma_{\text{noise}}$ , is proportional to  $\sqrt{\Delta f}$ . Therefore the SNR in the time domain is not a good measure of sensitivity, it can be artificially inflated by narrowing the bandwidth. Instead it is better to use *limit of detection*, defined as the number of spins that have to resonate within a bandwidth of 1 Hz to give an SNR of 3. This gives the normalised limit of detection as[90]:

$$\text{nLOD}_t = \frac{3n_s}{\text{SNR}_t \sqrt{\Delta f}}. \quad (2.234)$$

Where  $n_s$  is the number of spins that were present in the sample for the measurement and  $\text{SNR}_t$  is the signal to noise ratio in the time domain. In the frequency domain, this becomes

$$\text{nLOD}_\omega = \frac{3n_s \sqrt{\Delta t}}{\text{SNR}_\omega}, \quad (2.235)$$

here,  $\Delta t$  is the effective acquisition time for a single scan, given by the inverse of the line broadening applied in the processing of the spectrum.

Practically, NMR relies on signal averaging (see 2.3.2) to enhance the spectra. This method requires waiting between scans for the spins to reach thermal equilibrium. In this case, a better measure of sensitivity can be applied by using total measurement time as  $\Delta t$ . In this case the limit of detection now depends on instrumentation and sample as  $T_1$  relaxation dictates the experiment repetition rate.

### 2.3.4 Concentration limit of detection

Both types of LOD discussed so far are absolute measures. It is often of more interest to examine the *concentration* limit of detection cLOD. This is given by dividing the LOD by the sample volume:

$$\text{cLOD} = \frac{\text{nLOD}}{V_s} = \frac{\text{nLOD}}{\alpha_f V_c}. \quad (2.236)$$

Where  $V_c$  is the volume of the coil and  $\alpha_f$  is the filling factor defined in Eqn. 2.223.

Eqn. 2.235 shows that overall, the mass sensitivity of a probe is inversely proportional to SNR. It follows from Eqn. 2.226, that the reduction in coil size would lead to a reduction of nLOD. This relationship has been a key driving force in the development of micro-NMR, however, a coil size reduction of a factor of 2, reduces the volume by a factor of 8 leading to a rise in cLOD. For a *concentration* limited sample, it is more important to have as high a volume as possible to increase the number of spins available for detection. For a *mass* limited sample, the number of spins is fixed so it is more advantageous to reduce the size of the coil.

### 2.3.5 Transmission line probe

This work employs a planar transmission line probe (TLP) [1, 2], in which the geometry differs from that of a classic micro-coil. The design of the TLP is based off early work by van Bentum *et al.* and for an equivalent helix gives  $\sqrt{2}$  larger SNR [87]. The TLP geometry, shown in Fig. 2.8, features two conducting planes of a specific length with a constriction in the centre. This geometry, gives rise to an electromagnetic eigenmode with a strong anti-node of the magnetic field between the two planes at the constriction. This concentrates the r.f. field and the detection sensitivity onto the sample area. The probe is compatible with a generic microfluidic device that has well defined outer geometry, and a fixed sample chamber position. The main advantage of using this probe is the compatibility of the device with customisable microfluidic devices, allowing a broad range of applications such as tissue culture, microfluidic droplets, cell culture, and hydrogenation on a chip [1]. These applications can be coupled with practical NMR using the TLP, which few other microprobes allow [91–93]. The limit of detection LOD for the TLP used is  $1.4 \text{ nmol s}^{1/2}$  which comparatively lower than detectors of a similar size and more similar to the LOD of commercial cryo-probes mentioned previously. Where the probe is exceptional in terms of micro-detector is the cLOD, this is demonstrated in Fig. 2.9 which shows a wide variety of micro-NMR detectors that have been reported in the literature. Fig. 2.9 has detection volume and mass LOD (nLOD) plotted logarithmically on the *x*-axis and *y*-axis respectively, the diagonal lines represent constant concentration (cLOD). The general trend of decreasing nLOD with size is indicated with a line of gradient 1/2. The area shaded orange that is defined as the 'metabolomics feasible' range is a maximum  $5 \text{ mM } \sqrt{s}$  ensuring species present at  $0.1 \text{ mM}$  can be detected within less than 20 mins. The TLP has a cLOD of  $1 \text{ mM } \sqrt{s}$  and can detect species at  $0.02 \text{ mM}$  in that time frame. Whilst this is suitable for some metabolomic information to be gained, however, the subtle changes in molecules present at less than  $0.02 \text{ mM}$  are of interest but are unreachable with this probe using thermal polarisation at this time.

For this work, the goal is not only to combine NMR detection and microfluidics, clearly that has been done before. However, it is the combination of these two in a way that does not minimise compromises on either side: free fluidic design and complexity on the one hand, and the full resolution and sensitivity of conventional liquid state NMR spectroscopy on the other.

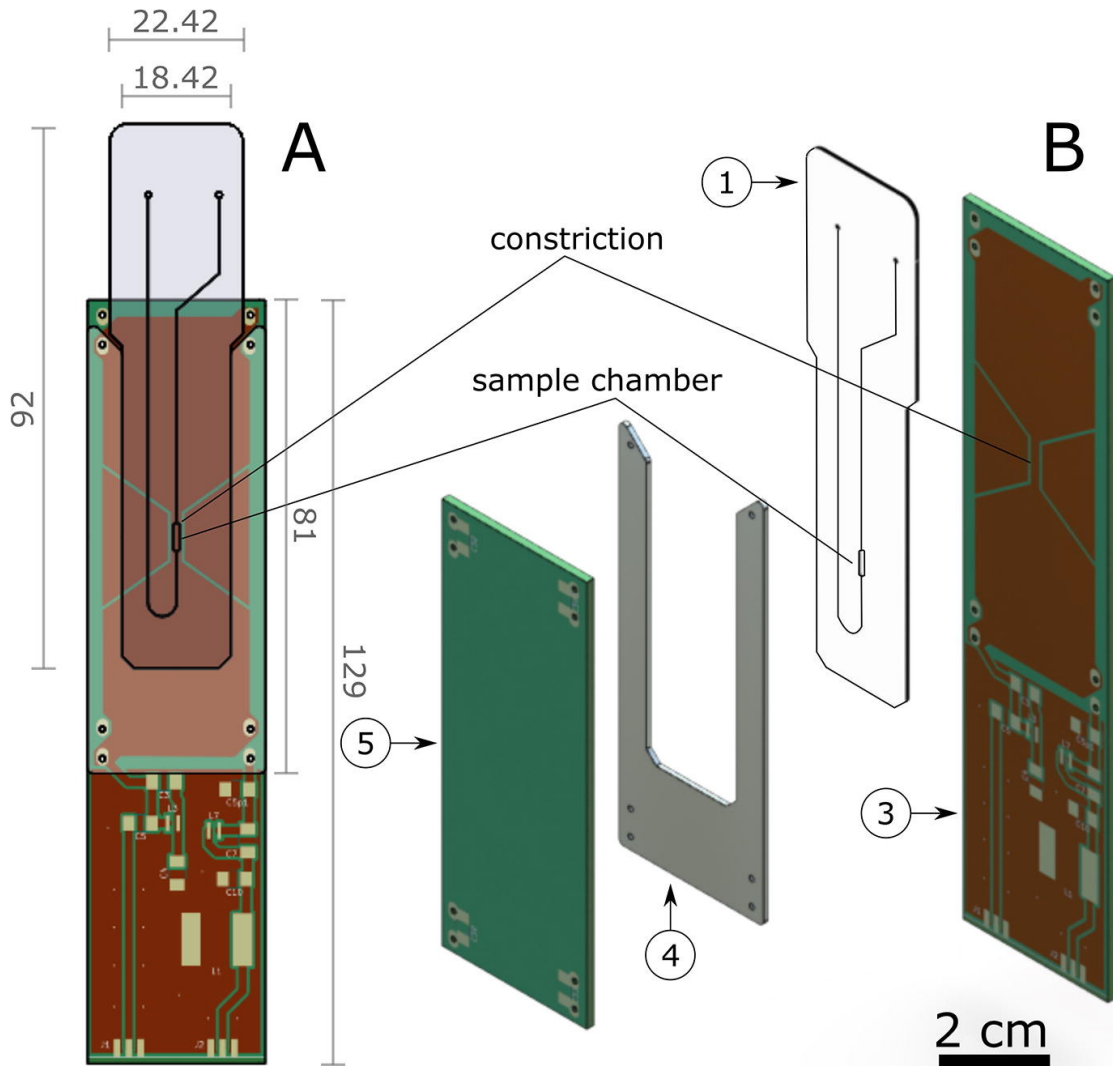


FIGURE 2.8: Drawings of the detector assembly and the microfluidic device (1). A: front view (dimensions in mm); B: exploded view. Spacer (4) ensures the alignment of the sample chamber with the constrictions on the PCB planes. In A, PCB plane 5 is hidden to show the orientation of 1 with respect to PCB plane 3. Thickness of each of the PCB planes is 1.52 mm and the copper layers on the PCBs is  $35 \mu\text{m}$ . Both the microfluidic device and the spacer are made from PMMA and have thickness of 0.9 mm and 1 mm respectively. Figure reproduced from [1].

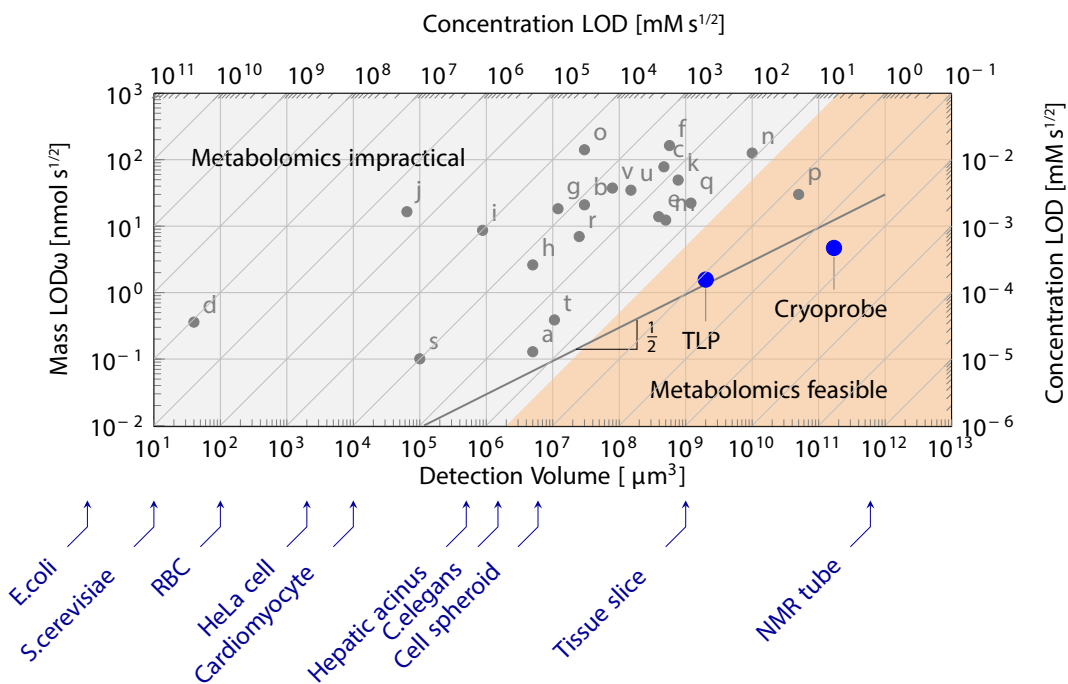


FIGURE 2.9: Plot comparing the limits of detection of previously design micro-NMR detectors. Letters a-t correspond to different authors as cited by Badilata *et al.* [90]. Letters u [94] and t [91] represent more recent work. The probe used here is labelled at TLP and a commercial cyro-probe is shown for reference.

## Chapter 3

# Microfluidic Droplet NMR

This chapter is an extended version of W Hale, G Rossetto, R Greenhalgh, G Finch and M Utz, High-resolution nuclear magnetic resonance spectroscopy in microfluidic droplets, *Lab on a Chip*, 2018, **18**, 3018-3024 [95]

### 3.1 Synopsis

In this chapter, a system that enables high-resolution NMR spectroscopy of microfluidic droplet emulsions is discussed. Acquiring NMR spectra of emulsions is complicated by the magnetic susceptibility mismatch between the phases, and the chip material. In order to overcome these challenges a 2-part solution is needed. Firstly, air-filled structures are incorporated into the microfluidic chip design in order to match the poly(methyl methacrylate) (PMMA) with the continuous phase (cyclohexane) susceptibility. Secondly, a Eu<sup>3+</sup> complex is doped into the dispersed phase (water) in order to match the susceptibility of the phases. High resolution spectra with line widths of 3 Hz were obtained in the ideal case. However, a serial dilution experiment that was used to obtain spectra of glucose droplets showed the highly sensitive dependence of line width on Eu concentration.

### 3.2 Introduction

Droplet microfluidics is the field of microfluidic research that separates samples into discreet droplets by dispersing one immiscible fluid (dispersed fluid) in another (continuous fluid). In this way, samples can be manipulated freely in the lab-on-a-chip (LoC) system, and problems due to viscous dispersion and cross-contamination are avoided. In doing so, microdroplets of tuneable size and volume, typically femto- to nanolitres, are produced at rate reported to be up to 44 kHz [96]. Thorsen et al [34] reported

one of the first droplet microfluidic devices. In the letter, they show how one can use microfluidic channels to generate mono-disperse microemulsions by shearing water into a perpendicular flow of oil. By varying the ratio of the pressures driving the flow of each fluid they produce droplets that range in diameter from 10  $\mu\text{m}$  to 60  $\mu\text{m}$ .

Droplets have since emerged as a versatile tool finding wide ranging applications in areas such as microcapsule synthesis [97], crystal growth [98], chemical reactions [99], cell/organism encapsulation [100–102], PCR [103, 104], and Protein studies [105, 106]. These applications are diverse owing to many advantages that microfluidic droplets possess: limited cross contamination; high production rates; large surface area to volume ratio; small reagent volumes; and independent control of each droplet [107].

Droplet generation can, broadly speaking, be divided into two categories. These are active and passive generation methods. Active methods are defined as applying additional force to the device to create droplets such as electric [108], magnetic [109] or centrifugal [110] or by modifying intrinsic forces by tuning fluid velocity [111]. Passive methods rely on the inherent instability of the liquid-liquid interface when mixing two immiscible fluid in order to generate droplets [112–114]. Zhu and Wang [115] have published an in-depth review of the various methods of droplet generation as well as the equations that govern them.

Here, active droplet generation is used in the form of fluid velocity variation. Two syringe pumps were employed that allowed separate manipulation of flow rates of the dispersed and continuous fluid. The dispersed and continuous phase are co-flowed to the the droplet generation point. By using this method, one can control the production rate and size of the droplets. Droplets of size 100  $\mu\text{m}$  in diameter and a rate suitable enough to fill the sample chamber. If the flow is too fast the droplets have a very low residence time and there is never enough build up to perform an experiment. If, however, the flow is too slow the droplets that are formed are too big and inconsistent for any kind of reliable experimentation.

As discuss in chapter 1, nuclear magnetic resonance (NMR) as a spectroscopic technique has two chief advantages. It is non-invasive and non-destructive which makes it ideally placed to study living systems without destroying them. Indeed, NMR and magnetic resonance imaging (MRI) are both methods actively employed in metabolomics [116], drug discovery [117] and cancer imaging [118]. The nature of NMR means that one can glean quantitative, system level information in one experiment without the need for chemical tags. In a microfluidic context, where fluorescence spectroscopy [119, 120], or mass spectrometry [121, 122], are often the methods of choice for detection, NMR can be used in parallel to these and contribute to a better understanding of the system.

In this work, the possibility to obtain high-resolution NMR spectra from small volumes of droplet emulsions on a chip is explored. Integration of high-resolution NMR spectroscopy with microfluidic systems is challenging for a number of reasons. On the

one hand, small sample volumes place stringent demands on detector sensitivity [90, 123]. This has recently been addressed with the design of highly efficient planar NMR micro-coils [124] and transmission line resonators [1, 2]. Another challenge is the preservation of high spectral resolution, which depends on a highly homogeneous magnetic field over the sample volume. Differences in magnetic susceptibility between the materials used for the microfluidic chip and the sample fluid, as well as the materials and geometry of the probe assembly, lead to a demagnetising field that varies continuously over the sample volume. Typical diamagnetic volume susceptibilities range from about  $-11$  ppm to about  $-5$  ppm (in SI units); [125, 126] differences of the order of several ppm are therefore commonplace. Unmanaged, they lead to broadening of NMR spectral lines over a ppm or more, which corresponds to a severe loss of resolution in  $^1\text{H}$  liquid state NMR.

Managing susceptibility differences for an emulsion of droplets on a microfluidic chip adds additional complexity, since three different materials are now involved: the chip, the continuous phase, and the droplet phase, all with different susceptibilities. This can be mitigated in a two-step approach, which is based on the observation that most organic solvents in use as continuous phases for droplet microfluidics are less diamagnetic than water. First, the susceptibility difference between the chip and the continuous phase are compensated by shimming structures that are added to the chip design. Then, the susceptibility of the aqueous droplet phase is matched to that of the continuous phase by adding a paramagnetic solute.

### 3.2.1 Susceptibility

Magnetic susceptibility,  $\chi_V$ , is a measure of how much a material will become magnetized in an applied magnetic field, broadly, this allows a classification of most materials as para- ( $\chi > 0$ ) or dia- ( $\chi < 0$ ) magnetic. Materials used in this work are listed in Table 3.1.

The magnetization of the material is given by the equation  $\mathbf{M} = \chi_V \mathbf{H}$  where  $\mathbf{M}$  is the magnetisation of the material and  $\mathbf{H}$  is the magnetic field. In [127], a derivation of how the susceptibility can affect the magnetic field around a sample and influence its spectra is given.

In the absence of currents Ampere's law requires that  $\nabla \times \mathbf{H} = 0$ . The magnetic field  $\mathbf{H}$  can then be expressed by a scalar magnetic potential  $U$  as:

$$\mathbf{H} = -\nabla U. \quad (3.1)$$

To describe an object being inserted into a magnetic field the potentials are split, as  $U = U_0 + U_d$ , where  $U_0 = H_0 z$  represents the original homogeneous field, and  $\mathbf{H}_d = -\nabla U_d$  is the field generated by the magnetic dipoles induced in the inserted object

(sometimes referred to as demagnetising field). The magnetic field  $H_0$ , which is assumed to be along the z-axis, arises from the superconducting coil.

The macroscopic magnetic induction  $\mathbf{B}$  is given by:

$$\mathbf{B} = \mu_0(\mathbf{H} + \mathbf{M}), \quad (3.2)$$

where  $\mu_0 = 4\pi \times 10^7 \text{ VsAm}^{-1}$  denotes vacuum permeability. With Gauss' law  $\nabla \cdot \mathbf{B} = 0$  this becomes:

$$\mathbf{B} = \mu_0(-\nabla(U_0 + U_d) + \mathbf{M}) \quad (3.3)$$

$$\nabla \cdot \mathbf{B} = \mu_0(-\nabla^2(U_0 + U_d) + \nabla \cdot \mathbf{M}) \quad (3.4)$$

$$\nabla^2 U_d = \nabla \cdot \mathbf{M}. \quad (3.5)$$

It is assumed that the object consists of a number of spatial domains characterised by a locally constant magnetic susceptibility  $\chi_k$ . The magnetisation therefore, is a piecewise constant,

$$\mathbf{M}_k = \chi_k H_0 \mathbf{e}_z, \quad (3.6)$$

the  $\nabla \cdot \mathbf{M}$  term from Eqn. 3.3 vanishes everywhere except at domain boundaries. The magnetic field satisfies the boundary conditions[128]

$$(\mathbf{H}_{d2} - \mathbf{H}_{d1}) \times \check{\mathbf{n}} = 0, \quad (3.7)$$

$$(\mathbf{H}_{d2} - \mathbf{H}_{d1}) \cdot \check{\mathbf{n}} = H_0(\chi_2 - \chi_1)\mathbf{e}_z \cdot \check{\mathbf{n}}, \quad (3.8)$$

where  $\check{\mathbf{n}}$  denotes the surface normal from material 1 to material 2. Equations 3.3, 3.7 and 3.8 are formally solved by:

$$U_d(\mathbf{r}) = \frac{H_0}{4\pi} \int_{\delta_{12}} \frac{\check{\mathbf{n}} \cdot \mathbf{e}_z (\chi_2 - \chi_1)}{\sqrt{(\mathbf{r} - \mathbf{r}')^2}} dS, \quad (3.9)$$

where  $dS$  is an infinitesimal surface element, and  $\mathbf{r}'$  is the integration variable. If there are more than two materials involved, as there are in droplets where there are three: the continuous phase; the water phase; and the PMMA, each boundary gives an additive contribution of the same form.

The resonance frequency observed is proportional to the magnetic induction  $\mathbf{B}_{ext}$  experienced by chemically equivalent nuclei within each domain. This induction is determined by the outside field  $H_0$  plus the induced magnetic dipoles of all molecules in

the same domain except the molecule carrying the observed spin.[129] In liquids and isotropic solids, the external magnetic induction differs from the macroscopic  $\mathbf{B}$  as:

$$\mathbf{B}_{ext} - \mathbf{B} = \frac{2\mu_0\chi_s}{3}\mathbf{H}_0. \quad (3.10)$$

The magnetic induction relevant for the Larmor precession of nuclear spins in the sample is therefore

$$\mathbf{B}_{ext} = \mu_0 H_0 \left(1 + \frac{\chi_s}{3}\right) \mathbf{e}_z - \mu_0 \nabla U_d. \quad (3.11)$$

Since  $\chi$  is a piecewise constant, the  $\mu_0 \nabla U_d$  term contributes to continuously varying fields and therefore any line broadening seen in the spectrum, whereas the  $\mu_0 H_0 \left(1 + \frac{\chi_s}{3}\right) \mathbf{e}_z$  term produces a bulk magnetic susceptibility shift (BMS) of the resonance line.

### 3.2.2 Matching susceptibilities

Matching susceptibilities of materials is a problem in microfluidic NMR. Fortunately, the susceptibilities of the materials used are typically similar as in most of our experiments, the solvent is water and the chip material is PMMA.

When the susceptibilities are mismatched, as they are in droplets, this can cause inhomogeneities in the magnetic field. These inhomogeneities shift the resonances and broadens the lines in the spectra rendering them useless. For any kind of useful NMR the magnetic field needs to be very homogeneous, with most commercial superconducting magnets achieving homogeneities of a few parts per billion. In microfluidic devices, air-filled shim structures have been utilised to match susceptibilities between chip construction material and fluid. Utz and co workers [127] have shown that susceptibility mismatches can be compensated for by installing such shim structures around the NMR sensitive region, to produce an equal and opposite demagnetising field to the one caused by the solution. Using this, they showed well resolved spectra can be taken of glucose dissolved in the mismatched liquid.

The work in this chapter, combines both structural shimming and chelated lanthanide doping, to glean high resolution NMR spectroscopy from a microfluidic droplet emulsion. The system is comprised a PMMA chip, an aqueous dispersed phase, and a cyclohexane continuous phase. As mentioned the PMMA and water are susceptibility are quite similar. The cyclohexane, however, is matched to neither. Hence, for all materials and solvents to be matched, structural shimming is employed to match the PMMA to the cyclohexane and a chelated lanthanide  $[\text{Eu(DTPA)}]^{2-}$  will be used to match the water susceptibility.

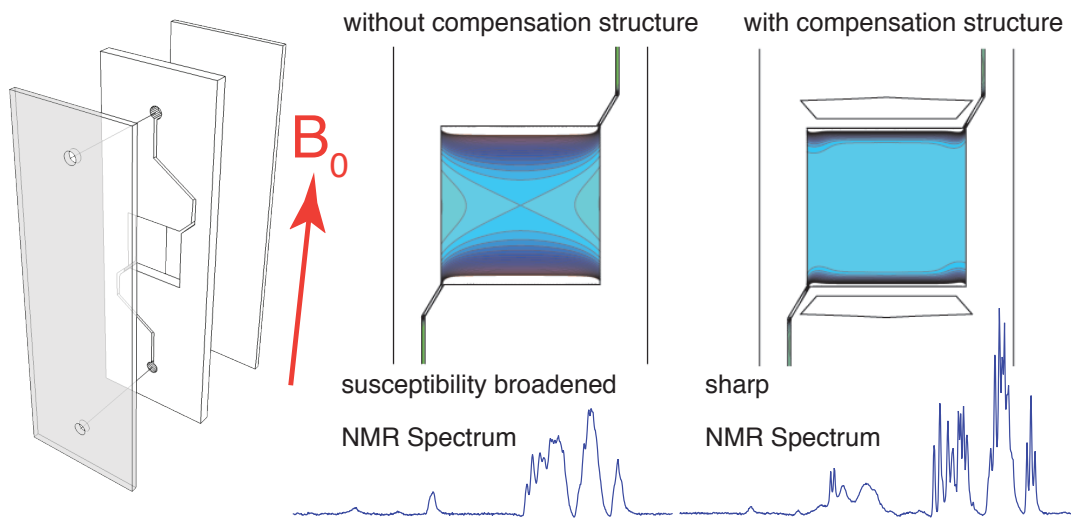


FIGURE 3.1: Summary graphic of the work in [127]. This shows how the NMR spectrum of glucose changes in a susceptibility mismatched chip but by cutting shim structures around the sample chamber high resolution NMR is still possible despite the mismatches.

In emulsions, susceptibility differences between the oil and aqueous phases lead to similar line broadening [125] NMR spectroscopy is extensively used to characterise emulsion droplet size distributions using pulsed field gradient methods [130–136]. These methods do not require spectral resolution of individual compounds other than the two solvents, and are therefore unaffected by the susceptibility broadening. By contrast, high-resolution NMR spectroscopy, with sufficient resolution to distinguish multiple compounds present in either of the two phases, requires careful mitigation of the susceptibility differences. It has also been shown that susceptibility differences can be compensated for in a liquid sample by doping of a chelated lanthanide [137]. For example, Lennon *et al.* demonstrated that the susceptibility mismatch between the inside and outside of deoxygenated red blood cells could be compensated for by doping 3mM of dysprosium tripolyphosphate  $[Dy(P_3O_{10})_2]^{7-}$  into the extracellular fluid [138]

It should be noted that in principle, the same effect could be achieved if a diamagnetic dopant could be added to the continuous phase. However, while paramagnetic dopants are easily available in the form of transition metal ions, no effective diamagnetic dopants exist in the literature.

$\text{Eu}^{3+}$  complexes are paramagnetic, and are frequently used as shift agents in NMR spectroscopy. Unlike other lanthanide ions such as  $\text{Gd}^{3+}$  or  $\text{Ho}^{3+}$ , which are powerful nuclear relaxation agents,  $\text{Eu}^{3+}$  has only a minimal effect on nuclear magnetic relaxation due to its extremely short electron spin-lattice relaxation time [139] Addition of millimolar quantities of  $\text{Eu}^{3+}$  to aqueous solutions therefore does not cause significant relaxation line broadening, but changes the bulk magnetic susceptibility of the solution

TABLE 3.1: Bulk magnetic susceptibilities

Compound	$\chi_V/10^{-6}$ (SI)	Ref
water	-9.05	[140]
cyclohexane	-7.640	[140]
PMMA	-9.01	[141]
Air	+0.36	[142]

proportionally to the Eu<sup>3+</sup> concentration. It is therefore possible to adjust the susceptibility difference in a droplet emulsion by adding a Eu<sup>3+</sup> complex that selectively dissolves in (or at least strongly partitions to) the aqueous phase.

In the present work, the diethyl-triamine pentaacetate (DTPA) complex of Eu<sup>3+</sup>, Eu[DTPA]<sup>2-</sup> is used. As an ion species, it is readily soluble in aqueous media, while exhibiting only negligible solubility in apolar organic solvents. Microfluidic chips are fabricated from poly methyl methacrylate (PMMA). By a fortunate coincidence, the susceptibilities of PMMA and water are very close to each other (Table 3.1). NMR lines in microfluidic devices made from PMMA are therefore narrow if aqueous samples are used, provided that the boundaries of the chip and the environment are either aligned with the external magnetic field, or are kept sufficiently remote from the detection area. By contrast, most organic solvents are considerably less diamagnetic than water, as exemplified by the case of cyclohexane, which has been used in the present study.

In the remainder of this chapter, finite element calculations are used to estimate the NMR line widths expected in a droplet emulsion depending on the susceptibility mismatch. The results are then compared to experimental line widths obtained with varying concentrations of Eu[DTPA]<sup>2-</sup> in the aqueous phase. Finally, narrow NMR lines are obtained by combining structural shimming [143] with susceptibility matching, and demonstrate that this approach can be used to obtain a high resolution of glucose contained within the compensated droplets. The chip used in this work is shown in Fig. 3.2. It consists of a sample chamber in the centre of the chip, which is designed to line up with the sensitive area of a transmission-line micro-NMR detector [2], and a convergent flow droplet generator. The aqueous phase and the continuous phase are fed into the two ports at the top. Droplets are formed and transported downstream into the sample chamber. The chamber is surrounded by four shim structures, which are circular shaped cutouts filled with air. They have been designed to compensate for the difference in susceptibility between the chip material (PMMA) and the oil phase (cyclohexane) as shown in Fig. 3.3. The operation of the chip is shown on the right side of Fig. 3.2; droplets of about 100  $\mu\text{m}$  diameter are formed and fill the sample chamber.

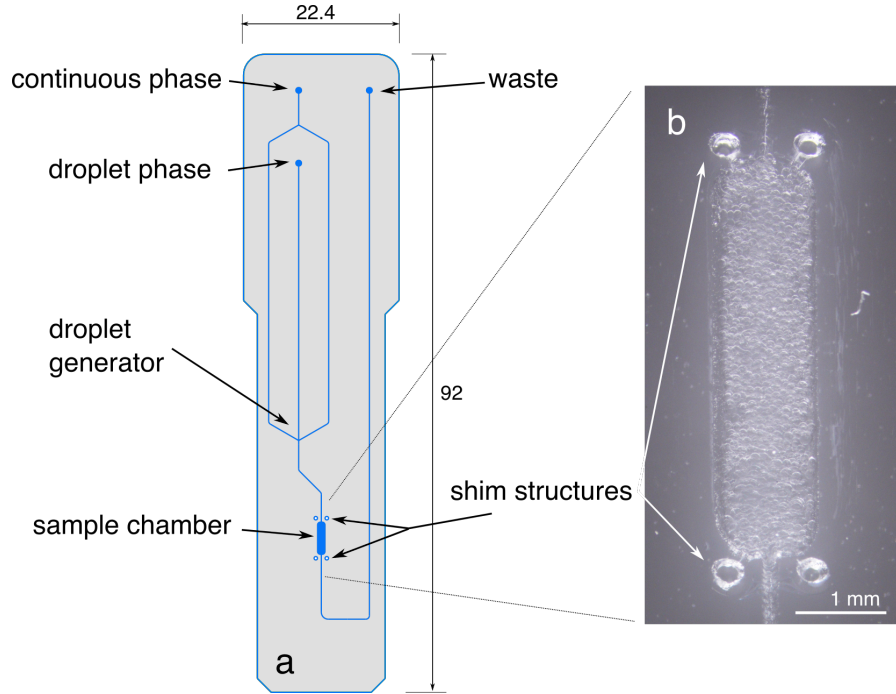


FIGURE 3.2: Droplet chip design (left) and detail micrograph of the sample chamber area filled with droplets (right). Some droplets are also visible in the entrance and exit channels.

### 3.3 Materials and Methods

Microfluidic chips of the design shown in Fig. 3.2 were fabricated from PMMA sheet material by laser cutting, and subsequent bonding of layers with a plasticiser under heat and pressure [144]. The chips consist of a top and bottom layer of 200  $\mu\text{m}$  thickness each, and a middle layer of 500  $\mu\text{m}$ . Fluid channels upstream from the flow-focussing droplet generator were scored into the middle layer at low laser power to a depth of about 100  $\mu\text{m}$ . Downstream from the droplet generator, the channels and the sample chamber were cut through the 500  $\mu\text{m}$  middle layer by increased laser power, as were the shimming structures. The chips were connected to a pair of Cole-Palmer 200-CE syringe pumps for droplet generation. A flow rate of 20  $\mu\text{l}/\text{min}$  was typically used for the continuous phase and 4  $\mu\text{l}/\text{min}$  for the aqueous droplet phase. The continuous phase consisted of cyclohexane (Sigma-Aldrich) with 0.5% w/v of span-65 (sorbitan tristearate, Sigma-Aldrich) as a surfactant to ensure droplet stability. The cyclohexane/span solution was kept in a water bath at 30°C for at least 2h to ensure complete dissolution of the surfactant. Prior to use, all solutions were left to equilibrate at a controlled room temperature of 25°C for at least 4h. Steady state conditions were ensured by letting the droplet generation run until the volume inside the chip had been exchanged at least five times. The chip was then disconnected from the syringe pumps, and the connection points sealed prior to insertion of the chip into the NMR probe.

NMR measurements were carried out on a Bruker AVANCE III spectrometer equipped with an Oxford wide bore magnet operating at 7.05 Tesla, corresponding to a  $^1\text{H}$  Larmor frequency of 300 MHz. A home-built NMR probe based on a transmission-line detector was used [2]. It accommodates microfluidic chips of the shape shown in Fig. 3.2. In the present work, the probe was doubly tuned to allow irradiation both at 300 MHz for  $^1\text{H}$  and at 75 MHz for  $^{13}\text{C}$ . Details of the electronic and mechanical design of the probe are given in Ref. [145].

NMR spectra were obtained at an RF nutation frequency of 66 kHz for  $^1\text{H}$ , corresponding to 90 degree pulse length of 3.8  $\mu\text{s}$ . Shimming was first performed on a sample of pure cyclohexane in an identical chip, these resulting values were used throughout all subsequent experiments with minor adjustments being made to linear shims (X,Y,Z) before each experiment to minimise line width. NMR spectra were acquired using Bruker spectrometer software (TopSpin 2.0), and were processed using home-built scripts written in *Julia*. [146] 20 mM of 4,4-Dimethyl-4-silapentane-1-sulfonic acid (DSS, Sigma Aldrich) was added to the aqueous phase as a chemical shift standard.

MRI gradient echo images of the sample chamber were obtained using ParaVision software and the fast low-angle shot (FLASH) pulse program. Flip angles of 30° were employed as well as a repetition time of 600 ms; 8 scans were averaged for each image. Two images were acquired for each field map at echo times of 6 and 10ms, respectively. The data was processed using home built software in *Mathematica*.

$\text{Eu}[\text{DTPA}]^{2-}$  solutions were prepared from a  $82.2 \pm 0.25$  mM stock solution, which was prepared by adding 1 g of  $\text{EuCl}_3$  (Sigma Aldrich) to a 50 mL volumetric flask. Separately, 3.93 g of diethylenetriaminepentaacetic acid (DTPA, Sigma Aldrich) and 1.99 g of NaOH (Fischer) were dissolved in 100 mL deionised (DI) water (Sigma Aldrich). An equimolar amount of the DTPA solution was added to the  $\text{EuCl}_3$  solution. The pH of this solution was then adjusted by addition of 2M NaOH solution dropwise until a neutral pH was attained. This was then topped up to 50 mL using DI water.

Finite element calculations of field distributions in emulsions were carried out using COMSOL Multiphysics with the "magnetic fields, no currents" (mfnc) physics module. Optimisation of the shim structures was done with COMSOL Multiphysics [147]. Starting from a SolidWorks model of the chip design, which was also used as a basis for production of the devices using a laser cutter, a finite element model was assembled and meshed. The shim structures consist of four symmetrically arranged circular holes through the middle layer of the three-layered devices. The positions and the diameters of these holes were optimised using a Nelder-Mead simplex algorithm. At each iteration, the magnetic field distribution inside the sample chamber was calculated using the mfnc physics module. The square norm of the second derivative of the z-component of the magnetic field was integrated over the volume of the sample chamber, and was used as optimisation target.

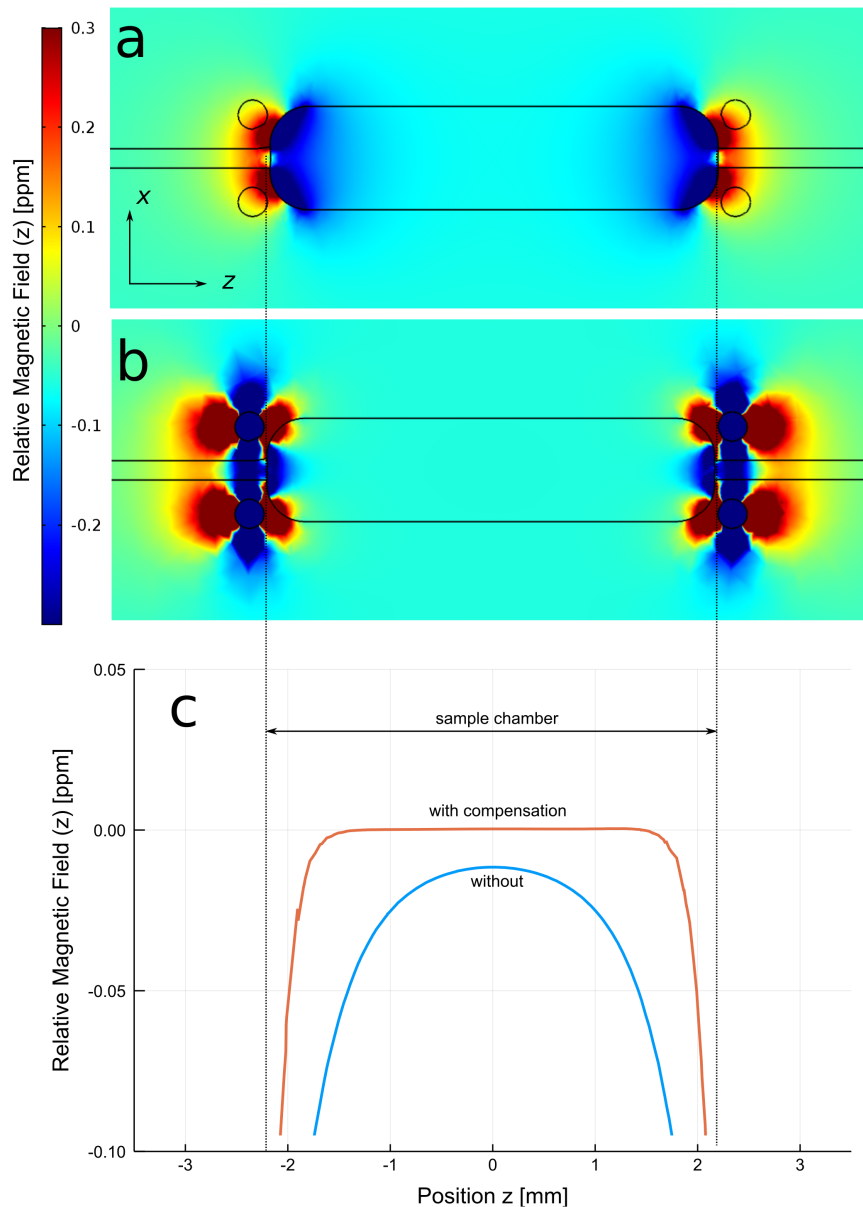


FIGURE 3.3: A: Finite element simulation of relative magnetic field distribution in an uncompensated chip (circular structures filled with PMMA) filled with cyclohexane and B: a compensated chip filled with cyclohexane; C: a linear plot of relative magnetic field along the z-axis through the middle of the sample chamber.

### 3.4 Results and Discussion

While it is possible to predict the magnetic field distribution in a system of multiple phases with differing susceptibilities by solving the magnetostatic equation (Eqn. 3.9), this requires precise geometric information on the arrangement of the two phases. In the case of an emulsion, the arrangement of the droplets is not regular. However, at high droplet densities, it can be expected to approximate a dense packing of spheres. In

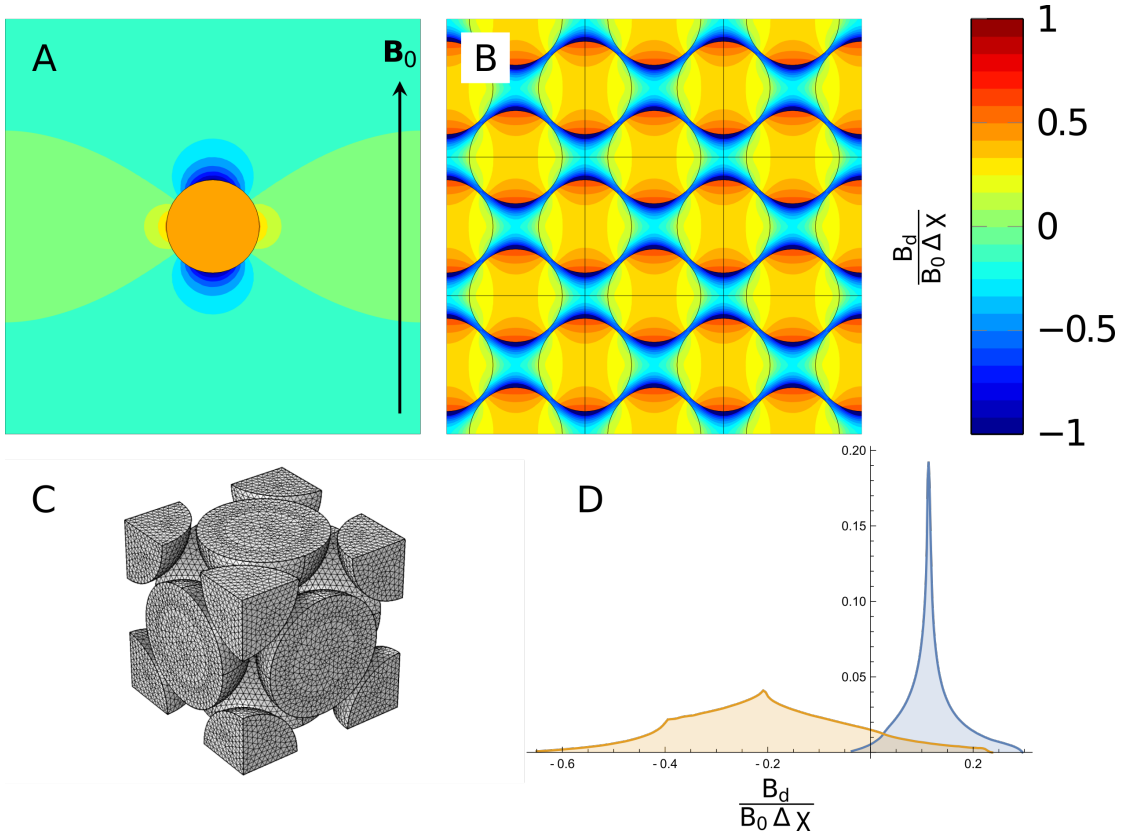


FIGURE 3.4: A: Finite element simulation of magnetic field distribution in droplets.  $z$ -component of the reduced magnetic field  $H_{\text{red}}$  in an isolated spherical droplet and B: in a face-centred cubic arrangement of droplets; C: FEM mesh used to calculate the result shown in B; D: histograms of the  $z$ -component of the reduced magnetic field in the continuous (orange) and in the droplet (blue) phase in the FCC arrangement.

order to obtain a semi-quantitative prediction, the demagnetising field in face-centred cubic (FCC) and simple cubic (SC) lattices of diamagnetic spheres was simulated; the results are shown in Fig. 3.4. A single unit cell containing one (SC) or two (FCC) independent spheres was meshed under periodic boundary conditions in all directions (Fig. 3.4C). As is well known, the demagnetising field inside an isolated diamagnetic sphere is homogeneous, while the field outside of the sphere is that of a magnetic point dipole located at the sphere's centre. This situation is approximated in a lattice if the lattice constant is much larger than the sphere diameter. The computed demagnetising field of a small sphere in an SC lattice is shown in Fig. 3.4A. The contour levels display the  $z$ -component of the local demagnetising field normalised by the background  $B_0$  field and the susceptibility difference  $\Delta \chi = \chi_{\text{sphere}} - \chi_{\text{continuous}}$ . The field is homogeneous inside the sphere, and a spatially varying demagnetising field only exists in the continuous phase. By contrast, in a densely packed face-centered cubic lattice the field is no longer homogeneous inside the spheres (Fig. 3.4B). The FCC lattice approximates the geometry of a dense microemulsion of homogenous water-in-oil droplets. Fig. 3.4D shows the histograms of the  $z$ -components of the demagnetising field in the continuous

and droplet phases of the FCC lattice, respectively.

The NMR spectra expected from an ideal emulsion of the same geometry can be predicted from these histograms (neglecting no broadening contributions from the sample container). The magnetic field relevant for nuclear Larmor precession, often referred to as the "external" field [129]  $\mathbf{B}_{\text{ext}}$  from Eqn. 3.11 is given by:

$$\mathbf{B}_{\text{ext}}(\mathbf{r}) = B_0(1 + \frac{\chi_s}{3})\mathbf{e}_z - \mu_0 \nabla U_d(\mathbf{r}), \quad (3.12)$$

where  $B_0$  is the magnitude of the external field,  $\chi_s$  is the local magnetic susceptibility, and  $U_d(\mathbf{r})$  is the scalar magnetic potential of the demagnetising field. The volume susceptibility of a solution containing a paramagnetic species at low concentration  $c_p$  is

$$\chi_s \approx \chi_0 + c_p \zeta_P, \quad (3.13)$$

where  $\chi_0$  is the volume susceptibility of the pure solvent, and  $\zeta_P$  is the molar susceptibility of the paramagnetic species.  $\zeta_P$  depends slightly on the molecular environment. For example, values of  $5.86 \cdot 10^{-5}$  l/Mol,  $5.68 \cdot 10^{-5}$  l/Mol, and  $6.14 \cdot 10^{-5}$  l/Mol have been measured at 300K for Eu<sub>2</sub>O<sub>3</sub>, EuF<sub>3</sub>, and EuBO<sub>3</sub>, respectively[148] To our knowledge, the precise molar susceptibility of Eu[DTPA]<sup>2-</sup> in aqueous solution has not been measured to date, but it is likely to be similar to the above values.

Fig. 3.5 shows <sup>1</sup>H NMR spectra obtained from emulsions in the chip shown in Fig. 3.2 with varying Eu[DTPA]<sup>2-</sup> concentrations in the aqueous phase as indicated in the figure. While the spectra are extremely broad without dopant, concentrations in the vicinity of 23 mM lead to much sharper lines for both water and cyclohexane, and the pure phase line widths are recovered at the optimum concentration of  $c_p = 23.75$  mM. Using the susceptibilities for H<sub>2</sub>O and cyclohexane given in Table 3.1, this leads to molar susceptibility for Eu[DTPA]<sup>2-</sup> of  $5.94 \cdot 10^{-5}$  l/Mol, well within the range of molar susceptibilities reported in literature for other Eu<sup>3+</sup> compounds. Using this value, the histograms shown in Fig. 3.4D can be converted into predicted emulsion NMR spectra as a function of Eu[DTPA]<sup>2-</sup> concentration in the aqueous phase, as shown in Fig. 3.6. The predicted behaviour is qualitatively similar to the experimental observation; very broad lines are expected at zero dopant concentration, while sharp lines are recovered near the optimum concentration. Also, the droplet phase peak is predicted to be narrower than the one from the continuous phase; this is already evident in the histograms in Fig. 3.4. However, the predicted spectra are consistently sharper than the experimentally observed ones. It is not entirely clear what causes the discrepancy between the experimental observation and the simulations. However, it should be noted that the experimental geometry of the emulsion differs significantly from the simulation; the droplets are neither uniform in size, nor are they arranged in a crystalline (FCC) lattice.

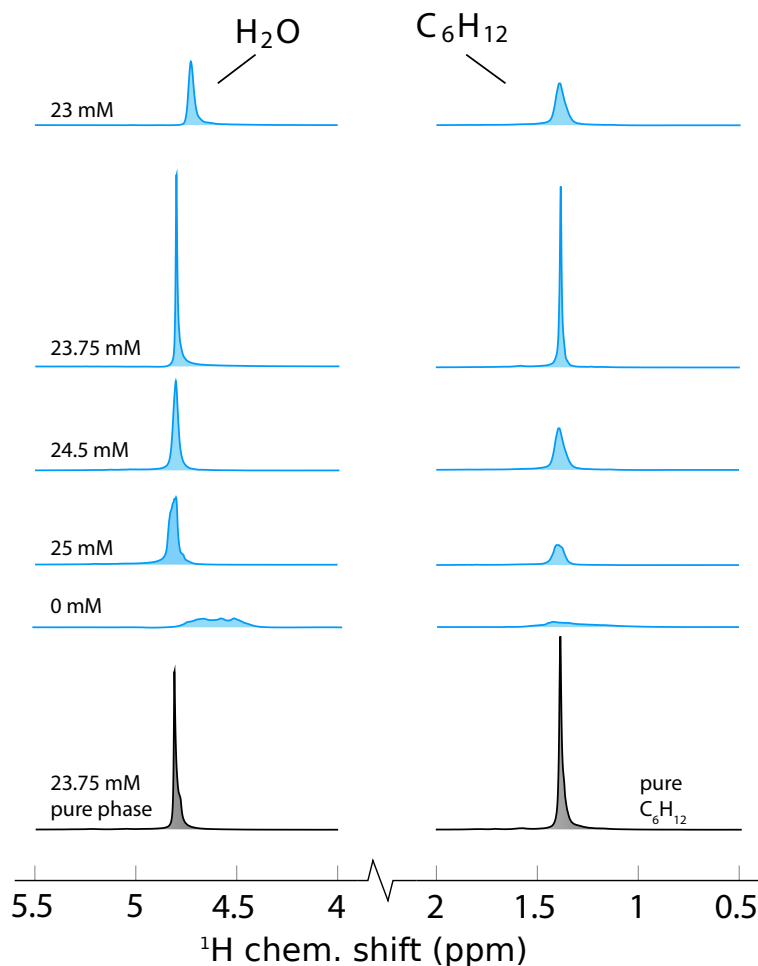


FIGURE 3.5:  $^1\text{H}$  NMR line shapes of water (left) and cyclohexane (right) of a water in cyclohexane emulsion as a function of  $\text{Eu}[\text{DTPA}]^{2-}$  concentration in the aqueous phase normalised to the sharpest peak. The spectra given in black are the pure phase spectra produced by the same chip.

The observed widths of the NMR signals from cyclohexane and water are summarised in Fig. 3.7. Here, the line width is defined as the ratio of the peak integral to the peak height, multiplied by  $2/\pi$ . In the case of Lorentzian line shapes, this definition is equivalent to the full width at half height (FWHM). However, the expected line shapes from the droplet emulsion are very different from a Lorentzian (Fig. 3.4D), such that using the FWHM would be misleading.

Both line widths exhibit a narrow minimum at 23.75 mM  $\text{Eu}[\text{DTPA}]^{2-}$  in the aqueous phase. The water and cyclohexane minimum peak widths are 3.1 Hz and 3.5 Hz, respectively. For comparison, the best resolution that has been reached with the same NMR probe is 1.76 Hz for a homogeneous solution of 150 mM sodium acetate in  $\text{H}_2\text{O}$ .[2]

Fig. 3.8 shows magnetic field ( $B_0$ ) maps of the sample chambers filled with droplet

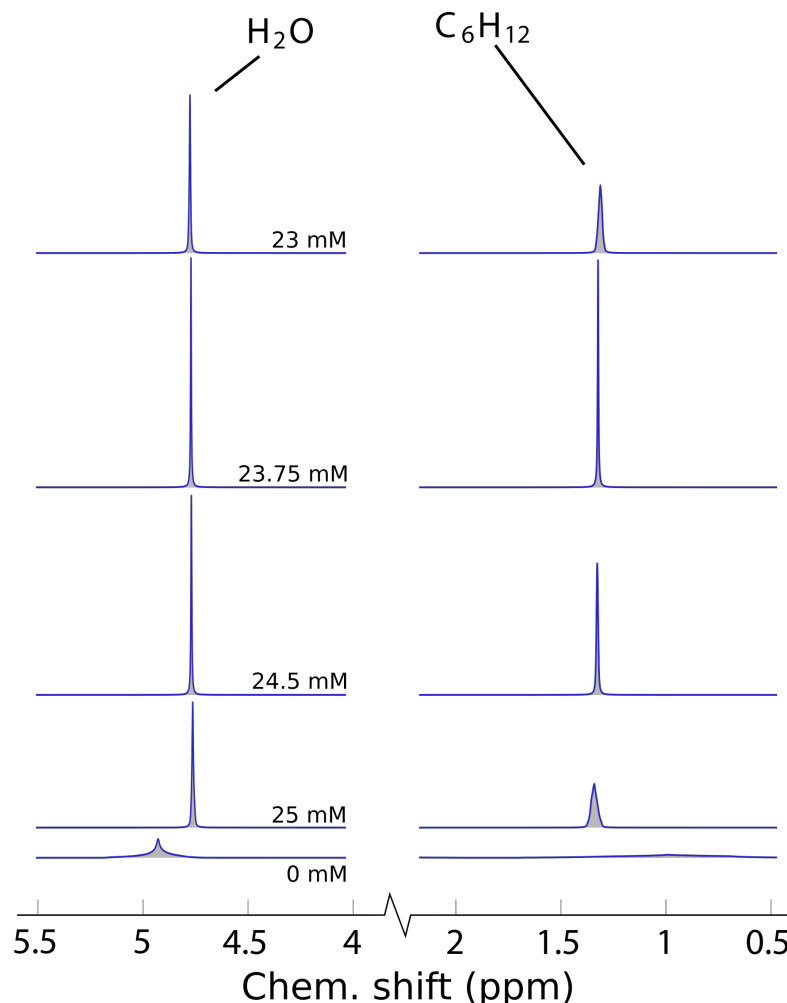


FIGURE 3.6: Predicted  $^1\text{H}$  NMR line shapes of water (left) and cyclohexane (right) of a water in cyclohexane emulsion as a function of  $\text{Eu}[\text{DTPA}]^{2-}$  concentration in the aqueous phase.

emulsions. In these experiments, two separate images with different echo times are acquired. The phase difference in each pixel is therefore proportional to the echo time difference and to the local magnetic field. The echo time difference is constant therefore the colour denotes the phase acquired by each pixel and can be used to inform on the homogeneity of the magnetic field in the sample.

In Fig. 3.8A, the droplets do not contain any paramagnetic dopant. As a result, the susceptibilities of the phases are unmatched, and strong local magnetic field differences are visible in the images. By contrast, the droplets in Fig. 3.8B are doped with 23.75 mM  $\text{Eu}[\text{DTPA}]^{2-}$ . As is clearly visible in the image, the local differences in the magnetic fields are strongly attenuated in this case.

While the above results have demonstrated that optimal line widths can be minimised in  $^1\text{H}$  NMR spectra of microfluidic emulsions by paramagnetic doping, the question remains if this is sufficient to resolve homonuclear  $J$ -couplings of a few Hz. This

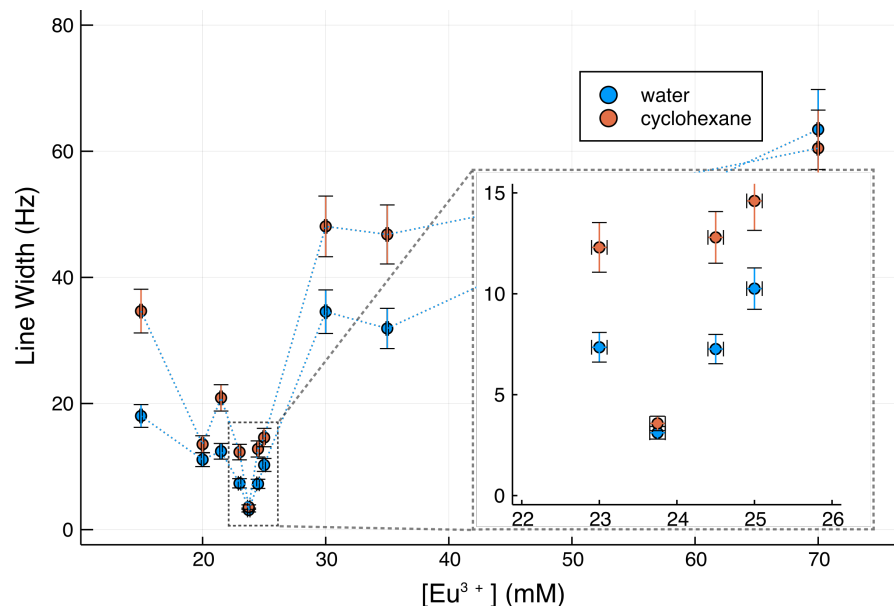


FIGURE 3.7: Observed line widths of water (blue circles) and cyclohexane (orange circles) in microfluidic droplet emulsions as a function of the  $\text{Eu}[\text{DTPA}]^{2-}$  concentration in the aqueous phase. Inset is the plot around the minimum concentration. The widths of both lines are minimal at the matched concentration of 23.75 mM.

is required in order to do meaningful NMR spectroscopy, particularly in the context of complex metabolic mixtures. The top trace in Fig. 3.9 shows a spectrum of 200 mM glucose and 23.75 mM  $\text{Eu}[\text{DTPA}]^{2-}$  in water. The water signal has been suppressed by pre-saturation. In this case, the resolution is about 3 Hz; such that e.g., the triplet at 3.2 ppm (which corresponds to the proton in the 2-position on the  $\beta$ -glucose anomer) is clearly resolved.

Spectrum 1 in Fig. 3.9 has been obtained from droplet emulsions, starting from an aqueous stock solution prepared to a nominal concentration of 23.75 mM in  $\text{Eu}[\text{DTPA}]^{2-}$  and 200 mM in glucose. Initially, the resolution in this spectrum is quite poor, in spite of the attempt to dope at the previously determined optimum concentration. Estimates predicted the pipetting and weighing errors to add up to an uncertainty in the concentration of the stock solution of  $\pm 1\%$ . Assuming the stock solution was too concentrated, rather than too dilute, it was then gradually diluted with small amounts of DI water corresponding to a change in concentration much less than the experimental error in each step. As can be seen in spectra 2-7, the resolution gradually increases, and matches the pure phase spectrum at spectrum 5, before it deteriorates again. In practice, high resolution spectra therefore require careful calibration of the dopant concentration. It may not be practical to achieve this in one step by preparing the stock solution, particularly if small volumes are used as in our experiments. Rather, a gradual dilution as in Fig. 3.9 may be required to calibrate the  $\text{Eu}[\text{DTPA}]^{2-}$  concentration for an accurate match of the aqueous and carrier fluid susceptibilities. However, if such a match is established, the resulting resolution is as good as that of the pure aqueous solution.

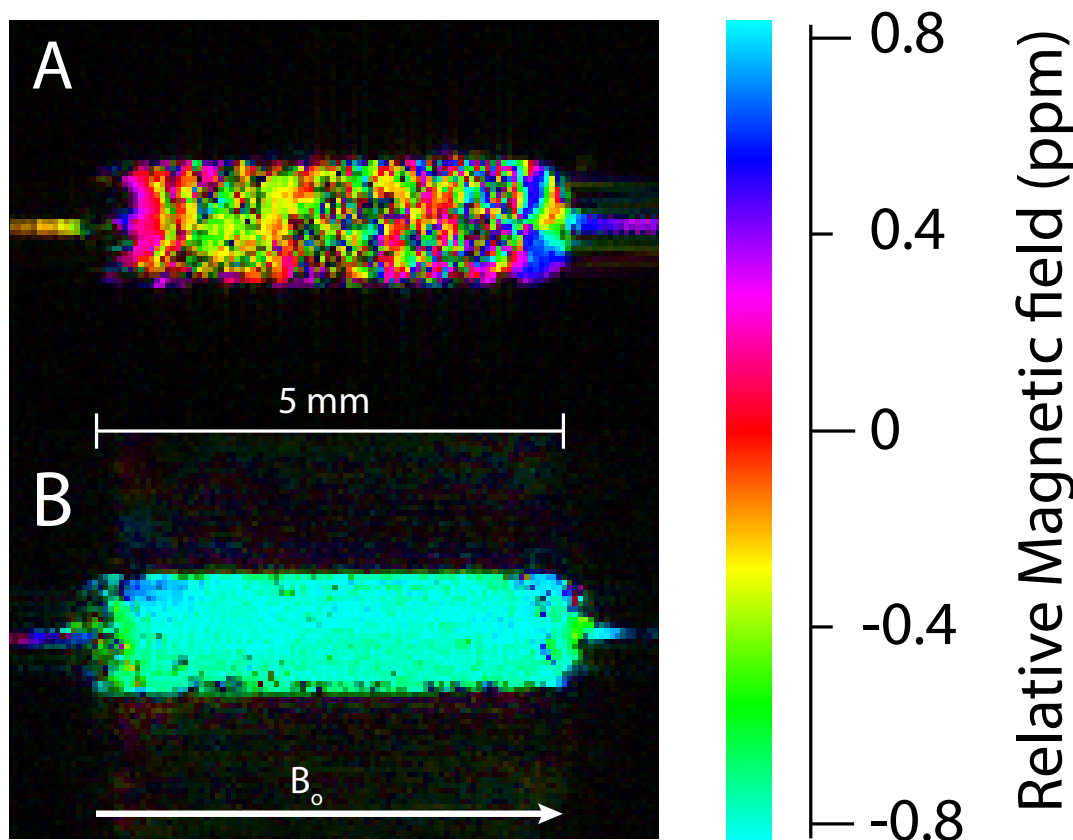


FIGURE 3.8:  $B_0$  Field maps obtained by magnetic resonance imaging of emulsions with (A)  $\Delta\chi = -1.41 \times 10^{-6}$  and (B)  $\Delta\chi \approx 0$ .

### 3.5 Conclusion

Susceptibility differences between the chip, the aqueous phase, and the oil phase in a microfluidic droplet system can be successfully mitigated by a combination of structural shimming and doping of the less diamagnetic of the liquid phases with a europium compound. The ultimate resolution achieved is only slightly inferior to what has been demonstrated in homogeneous solutions on a microfluidic chip and is suitable for high resolution NMR spectroscopy.

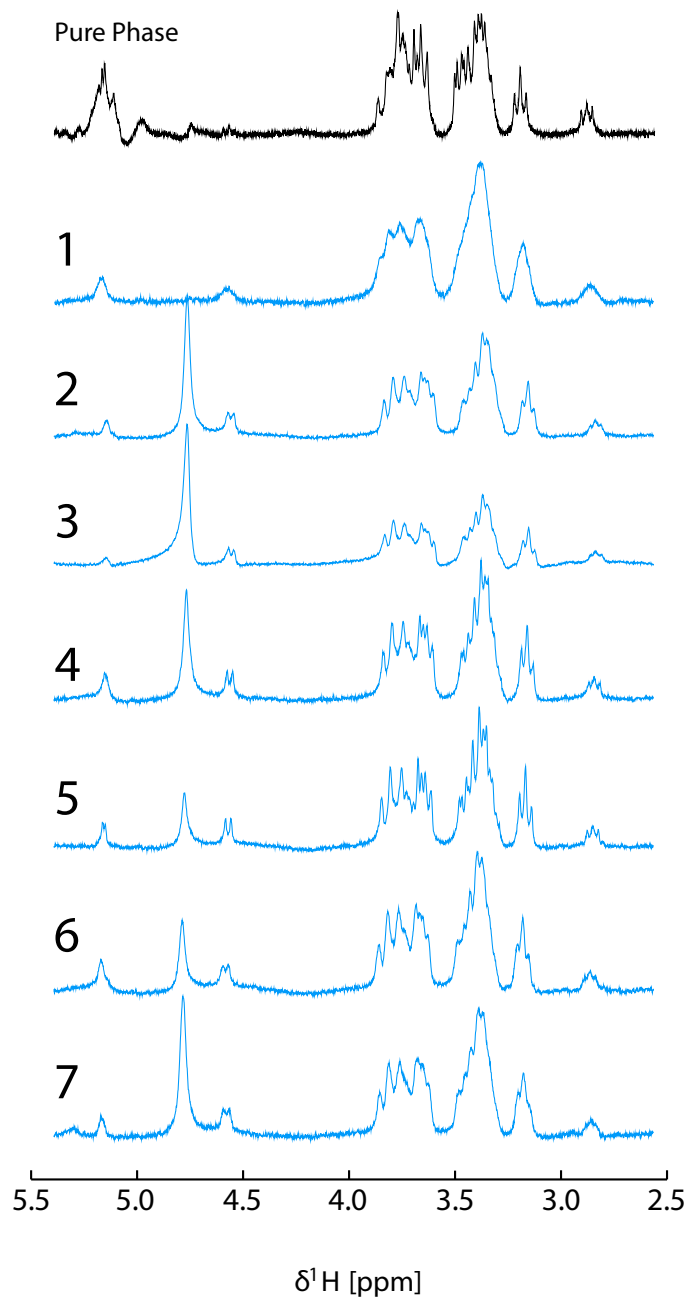


FIGURE 3.9: Spectra of 200 mM Glucose in  $\text{H}_2\text{O}$  obtained from microfluidic droplet emulsions in cyclohexane. 1: Aqueous phase contains  $c_0 = 23.75 \pm 0.25$  mM  $\text{Eu}[\text{DTPA}]^{2-}$ . Spectra 2-7 have been obtained by gradual dilution of the aqueous phase with small amounts of DI water. 2:  $\ln c/c_0 = -0.5\%$ ; 3:  $\ln c/c_0 = -0.75\%$ ; 4 :  $\ln c/c_0 = -0.875\%$ ; 5 :  $\ln c/c_0 = -1.0\%$ ; 6 :  $\ln c/c_0 = -1.125\%$ ; 7 :  $\ln c/c_0 = -1.25\%$ . A spectrum of pure phase 200mM glucose with optimised Eu doping in the same chip is included for comparison (black). The nonuniform peak at 4.8 ppm is due to carrier frequency drift during water suppression

# Chapter 4

## Parahydrogen induced polarization on a chip

This chapter is an extended version of J Eills<sup>1</sup>, W Hale<sup>1</sup>, M Sharma, M Rossetto, M H Levitt and M Utz, High-Resolution Nuclear Magnetic Resonance Spectroscopy With Picomole Sensitivity by Hyperpolarisation On A Chip, *Journal of the American Chemical Society*, 2019 [149]

### 4.1 Synopsis

In this chapter a device that combines high-resolution NMR and parahydrogen induced hyperpolarization (PHIP) with a high-sensitivity transmission line micro-detector is discussed. The para-enriched hydrogen gas is introduced into solution by diffusion through a membrane integrated into a microfluidic chip. NMR microdetectors, operating with sample volumes of a few  $\mu\text{l}$  or less, benefit from a favourable scaling of mass sensitivity discussed in 2.3. However, the small volumes make it very difficult to detect species present at less than millimolar concentrations in microfluidic NMR systems.

In view of overcoming this limitation, parahydrogen-induced polarization (PHIP) is implemented on a microfluidic device with  $2.5 \mu\text{l}$  detection volume. Integrating the hydrogenation reaction into the chip minimises polarization losses to spin-lattice relaxation, allowing the detection of picomoles of substance. This corresponds to a concentration limit of detection of better than  $1\mu\text{M}\sqrt{\text{s}}$ , unprecedented at this sample volume. The stability and sensitivity of the system can be used to extract quantitative information on the hydrogenation kinetics and their interplay with nuclear relaxation. It is further exemplified by homo- ( $^1\text{H}-^1\text{H}$ ) and heteronuclear ( $^1\text{H}-^{13}\text{C}$ ) 2D NMR experiments at natural  $^{13}\text{C}$  abundance.

---

<sup>1</sup>These authors contributed equally to the work.

## 4.2 Introduction

High-resolution NMR spectroscopy is a superbly versatile method which provides detailed, and quantitative, information on chemical composition and structure. It is widely used to follow the progress of chemical reactions [150, 151], as well as metabolic processes in living systems [152–155]. However, NMR suffers from inherently low sensitivity which is due, in part, to the very weak polarization of nuclear spins along the magnetic field for samples in thermal equilibrium at ambient conditions. Conventional high-resolution NMR therefore requires nanomole quantities of sample. Many important problems require detection of analytes at low micromolar concentrations, such as transient reaction intermediates, or metabolic species. Despite the comparatively higher mass sensitivity of NMR for small sample volumes [156, 157], conventional micro-NMR systems around  $1 \mu\text{L}$  achieve mass limits of detection of no better than [2]  $1 \text{ nmol}\sqrt{\text{s}}$ , corresponding to a concentration limit of detection of  $1 \text{ mM}\sqrt{\text{s}}$ . An increase of several orders of magnitude in sensitivity is therefore required to enable NMR studies of mass-limited samples at micromolar concentrations.

Microfluidic lab-on-a-chip devices are finding increasing applications in chemistry and the life sciences. They provide detailed control over the experimental conditions at a much smaller length scale than conventional reactors, and allow integration of synthesis, separation, and analytical steps on a single platform [158–165]. The small size also affords the possibility of high experimental throughput. In the life sciences, microfluidic devices are increasingly used as sophisticated culture platforms for cells, cell assemblies, tissues, and small organisms [166–170]. The integration of NMR with microfluidics [2, 90, 171, 172] is promising, as it enables in-situ, non-invasive monitoring of chemical and metabolic processes in lab-on-a-chip systems.

The usefulness of microfluidic NMR could be significantly enhanced if the following conditions could be met: (i) sample volumes around  $1 \mu\text{l}$  or less; (ii) a concentration limit of detection near  $1 \mu\text{M}\sqrt{\text{s}}$ ; and (iii) spectral resolution of better than 0.01 ppm to allow distinction and identification of chemical species.

Although exquisitely sensitive NMR detection schemes exist, approaching even single-spin detection in favourable cases [173–183], they lack spectral resolution. While a recent study has demonstrated resolution of  $J$  couplings using a nitrogen-vacancy (NV) centre magnetometer [184]. None of these alternative detection schemes are compatible with high (several Tesla) magnetic fields, which are essential to produce spectral dispersion by chemical shifts. So far, no method has been demonstrated with the combination of high spectral resolution, high chemical dispersion, and high sensitivity for small volumes required for advanced microfluidic NMR measurements significantly below the  $1 \text{ mM}$  concentration scale.

Hyperpolarization methods generate substances which exhibit a transiently high level of nuclear spin polarization, with an increase in the NMR signal strength of more than 4 orders of magnitude [185], and can be combined with micro-NMR detectors and microfluidic systems [186–193]. One such method involves the chemical reaction of the singlet spin isomer of molecular hydrogen, and is called parahydrogen-induced hyperpolarization (PHIP) [194–197].

While most studies have so far brought the reaction liquid in direct contact with hydrogen gas either through bubbling or by atomisation of the liquid in a hydrogen-filled chamber [198–204], liquid-gas interfaces and in particular bubbles pose difficulties in the context of microfluidic devices, since they tend to alter the flow properties, and can block fluid transport altogether. Continuous delivery of parahydrogen by diffusion through gas-permeable membranes has been demonstrated at conventional size scales [205, 206]. It has been shown that silicone elastomer membranes can be used to deliver parahydrogen directly to a flowing liquid in a microfluidic device [192]. Bordonali et al [193] have recently combined a microfluidic NMR probe system with a gas exchange chip based on a silicone elastomer membrane to implement the SABRE (signal enhancement by reversible exchange) variant of parahydrogen-induced polarization, but achieved only small signal enhancement factors (3 to 4).

In distinction from previous work [198–204, 206], this work integrates the hydrogenation reactor into the chip itself, which greatly reduces the polarization losses due to spin-lattice relaxation. As shown below, a signal enhancement factor over thermal polarization of about 1800 is achieved, allowing detection of a picomole quantity of analyte in a sample volume of 2.5  $\mu\text{l}$ , while maintaining the full resolution of conventional  $^1\text{H}$  NMR spectroscopy.

This is accomplished by letting the parahydrogen gas diffuse through a silicone elastomer membrane [206] to come into contact with a solution flowing through the chip at a constant rate. The solution contains a precursor, which is hydrogenated through a homogeneous catalyst also present in the solution. Two hydrogenative PHIP experiments are performed in this way. In the ALTADENA experiment, the solution is hydrogenated ‘on-chip’ at low magnetic field and transferred to a high field magnet for detection. ALTADENA is used as a proof of principle that the device is capable of hydrogenation ‘on-chip’. In the PASADENA reactions, the microfluidic device is held in the bore of a conventional NMR magnet using a purpose-built transmission line NMR probe. This yields a continuous on-chip stream of hyperpolarized material. As shown in the following, in addition to very high detection sensitivities, this also results in a continuous and highly stable operation of the system, making it possible to perform hyperpolarized two-dimensional NMR experiments [205, 207–209]. By replacing the hyperpolarized gas feed with hydrogen gas at thermal equilibrium, it is possible to gain kinetic information on the hydrogenation process, as well as to calibrate the intensity of the hyperpolarized NMR

signals. This allows accurate assessment of the achieved polarization levels, something that has been notoriously difficult in the context of parahydrogen-induced polarization.

## 4.3 Hyperpolarization

### 4.3.1 Sensitivity

As described in 2.2.5.1, NMR has low polarization levels that are governed by the Boltzmann distribution given in Eqn. 2.73. For example, for a spin-1/2 particle in a static field of 14.1 Tesla there is only a factor of  $6 \times 10^{-6}$  difference in the populations of the  $|\alpha\rangle$  and  $|\beta\rangle$  state. Compared to other detection techniques, NMR suffers from poor limits of detection (LODs) in comparison to other detection methods. Raman Spectroscopy, has LODs of  $10^{-12} - 10^{-15}$  M, Laser induced fluorescence (LIF) has detected concentrations at  $10^{-13}$  M and mass spectrometry has achieved  $10^{-19}$  M. These alternative techniques are several orders of magnitude higher than that of NMR. While sensitivity is not a strong point, NMR is quantitative, non-invasive, and non-destructive making it an ideal tool for mass limited and, in particular, living samples.

### 4.3.2 Hyperpolarization

From Eqn. 2.73 in 2.2.5.1, it is found that, the polarization level of nuclear spins at room temperature is low. In fact, for protons, it is only  $3 \times 10^{-6}$  per Tesla [210]. The signal derived from an NMR experiment is proportional to this polarization and means that the sensitivity and LOD is limited. The highest field available commercially is 28 Tesla which corresponds to polarization levels in protons of  $10^{-4}$  and whilst there are clear advantages to working in higher fields the size and more importantly - cost, make them unsuitable for many applications. Clearly just increasing the field is not a viable option if close to unity polarization is to be achieved.

There are techniques for increasing the spin polarization levels in samples to beyond the thermal equilibrium. The general term used to describe these is hyperpolarization. Hyperpolarization has applications in a diverse range of fields such as MRI [211–214], drug discovery [215, 216], reaction monitoring [217–219], metabolomics [220, 221], catalysis[222, 223] and material chemistry [224–226].

However, these hyperpolarized states are still subject to relaxation as discussed in 2.2.10 and return to thermal equilibrium with time constant  $T_1$ . This means the hyperpolarized spin order lasts seconds to minutes which limits their applications.

### 4.3.3 Techniques

#### 4.3.3.1 Brute Force

The most simple technique for hyperpolarization is "brute force". It is performed by simply cooling the sample to a few degrees kelvin in a high magnetic field [227, 228], under these circumstances, the polarization of  $^1\text{H}$  nuclei is 1%. In an experiment, the sample is first cooled to 2.3 K, after which, there is a waiting period to allow for the build up of polarization of the  $^1\text{H}$  nuclei. This period is required due to long  $T_1$  times at cryogenic temperatures and can be up to 70 hours [227]. After the polarization build up, the solid sample is passed through a low field to facilitate thermal mixing and polarization of  $^{13}\text{C}$  nuclei. Finally, the solid sample is rapidly dissolved in warm solvent and detected.

There are drawbacks however, firstly, the long  $T_1$  times at cryogenic temperatures mean long wait times are required in order to sufficiently build up polarization in the sample and prohibit high-throughput production. Secondly, and perhaps more importantly, the limit of polarization with this technique is around  $10^{-2}$  at achievable magnetic fields and temperatures.

#### 4.3.3.2 Dynamic Nuclear polarization

Dynamic nuclear polarization (DNP) methods use the thermal equilibrium electron spin polarization to polarize the nuclei under investigation. Close to unity polarization of the electrons is achieved by cooling to cryogenic temperatures (<2K) in a high magnetic field (>7 T). The electron polarization is transferred to nearby nuclear spins by saturating one of the transitions of the electron-nuclear coupled spin system with microwave frequency radiation.

The source of the electrons are 'free radicals' - molecules that have an unpaired electron spin, that are spread homogeneously throughout the sample. After cooling, the sample is held in a cryostat which is at 1.2 - 1.5K. The electrons have a much shorter  $T_1$  in contrast to nuclear spins so after irradiation with microwave radiation to induce polarization transfer between electrons and nuclei, the electrons repolarize quickly compared to the nuclei who retain non-equilibrium polarization. This polarization diffuses throughout the sample. After some time, tens of minutes is not uncommon, the nuclear spins are polarised to around 0.1 or 10%. The sample is then detected, either as the solid, or a liquid, depending on which type of DNP is being performed.

Several different types of DNP have been reported. These are solution state DNP [229], solid state magic angle spinning (MAS) DNP [230], rapid-melt DNP [231] and static solid state DNP with dissolution and observation [232]. The latter is most commonly referred to as dissolution-DNP and written as d-DNP.

The large equipment required for d-DNP, as well as the high cost of liquid helium for the cryostat and the extra superconducting magnet can make this method prohibitive for most NMR groups.

## 4.4 Parahydrogen Induced polarization - PHIP

### 4.4.1 Parahydrogen

Hydrogen exists as a diatomic made up of two protons and two electrons. As such, the total wave function contains electronic, vibrational, rotational and spin components and can be written as:

$$\Psi^{tot} = \Psi^{elec}\Psi^{vib}\Psi^{rot}\Psi^{spin} \quad (4.1)$$

Because the two protons are fermions they are subject to the Pauli exclusion principle which states that the total wave function must be antisymmetric with respect to exchange. With this in mind, it is important to note that the electronic, and vibrational states, are symmetrical in the ground state. and it is assumed that they occupy the ground state, the symmetry of the overall wave function therefore depends of the symmetry of  $\Psi^{rot}\Psi^{spin}$ .

Rotational wavefunctions have quantum number  $J$ . For even numbers of  $J$  ( $J=0,2,\dots$ ) the wavefunction is symmetric with respect to particle exchange for odd numbers of  $J$  ( $J=1,3,\dots$ ) the wavefunction is antisymmetric. The nuclear spin wave function can also be symmetric or antisymmetric. By adding the angular momentum of both spins, it can be shown that they combine to give four possible quantum states with column vector representations derived from Eqn. 2.23:

$$|T^+\rangle = |\alpha\alpha\rangle = \begin{pmatrix} 1 \\ 0 \\ 0 \\ 0 \end{pmatrix} \quad (4.2)$$

$$|T^0\rangle = \frac{1}{\sqrt{2}} |\alpha\beta\rangle + |\beta\alpha\rangle = \frac{1}{\sqrt{2}} \begin{pmatrix} 0 \\ 1 \\ 1 \\ 0 \end{pmatrix} \quad (4.3)$$

$$|T^-\rangle = |\beta\beta\rangle = \begin{pmatrix} 0 \\ 0 \\ 0 \\ 1 \end{pmatrix} \quad (4.4)$$

$$|S^0\rangle = \frac{1}{\sqrt{2}} |\alpha\beta\rangle - |\beta\alpha\rangle = \frac{1}{\sqrt{2}} \begin{pmatrix} 0 \\ 1 \\ -1 \\ 0 \end{pmatrix}. \quad (4.5)$$

The three triplet ( $T$ ) states have spin quantum number  $I = 1$  and  $m_I = +1, 0, -1$  denoted by the superscript symbol on each state. The singlet ( $S$ ) state has  $I = 0$  and  $m_I = 0$ . The triplets states are symmetric with respect to spin exchange, whilst the singlet state is anti-symmetric with respect to spin exchange. Hydrogen in the triplet state is referred to as *ortho* and the singlet state is referred to as *para*.

In order for  $\Psi^{tot}$  to be antisymmetric, the antisymmetric rotational states are restricted to coupling to the symmetric (triplet) spin states whilst the symmetric rotational states are restricted to coupling to the antisymmetric (singlet) state.

The rotational energy is given by  $E_j = \frac{J(J+1)\hbar^2}{2I}$  where  $I$  is the moment of inertia of the diatomic and is given by  $I = \mu l^2$ , where  $\mu$  is the reduced mass, and  $l$  is the internuclear distance.

At room temperature, the ratio of *ortho* to *para* hydrogen is very nearly 3 to 1. However, by cooling down hydrogen the lowest ( $J = 0, 1$ ) rotational energy states start to become populated. The ratio of *para* to *ortho* hydrogen may be calculated using the respective partition functions [234]:

$$\frac{N_{\text{para}}}{N_{\text{ortho}}} = \frac{\sum_{J=\text{even}} (2J+1) \exp\left\{-\frac{J(J+1)\theta_R}{T}\right\}}{3 \sum_{J=\text{odd}} (2J+1) \exp\left\{-\frac{J(J+1)\theta_R}{T}\right\}}, \quad (4.6)$$

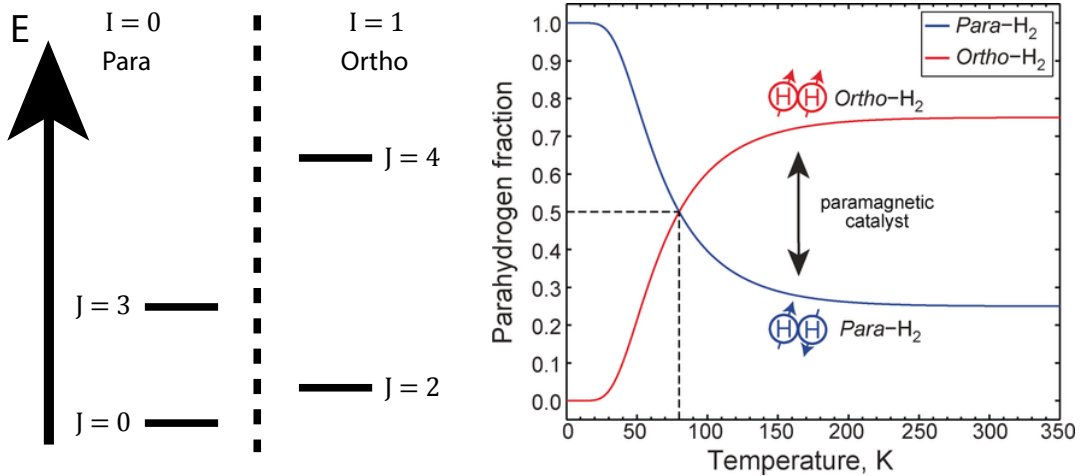


FIGURE 4.1: Left: The rotational energy levels of para- and orthohydrogen with their associated  $J$  values. Right: a graph showing the fraction of para- and orthohydrogen as a function of temperature. The dotted line shows 50% para enrichment that is achieved by cooling to 77K using liquid nitrogen. Image taken from [233].

for the first few levels this is:

$$\frac{N_{\text{para}}}{N_{\text{ortho}}} = \frac{1 + 5\exp\{-\frac{6\theta_R}{T}\} + 9\exp\{-\frac{20\theta_R}{T}\} + 13\exp\{-\frac{42\theta_R}{T}\} + \dots}{3(3\exp\{-\frac{2\theta_R}{T}\} + 7\exp\{-\frac{12\theta_R}{T}\} + 11\exp\{-\frac{30\theta_R}{T}\} + \dots)}, \quad (4.7)$$

where the rotational constant,  $\theta_R$ , is:

$$\theta_R = \frac{\hbar^2}{8\pi^2 I k_b}. \quad (4.8)$$

Using Eqn. 4.7, the percentage of parahydrogen in an equilibrium mixture can be plotted as a function of temperature, shown in Fig. 4.2.

By cooling alone, the ratio would remain unchanged, conversion from ortho to para spin states without the aid of a catalyst (typically charcoal or iron (III) oxide) is not possible. The catalyst temporarily breaks the symmetry of the  $\text{H}_2$  molecule which allows spin-spin transitions and leads to a much larger fraction of the *para* form of hydrogen. Crucially, when warmed up to room temperature in the absence of a symmetry breaking catalyst, no conversion from the singlet state  $|S^0\rangle$  back to the triplet states  $|T^+\rangle$ ,  $|T^0\rangle$ ,  $|T^-\rangle$  occurs. This is because transitions between singlet and triplet states are forbidden through quantum mechanical selection rules. It is therefore possible to store pure parahydrogen in the right container for days to weeks.

Para enrichment fraction,  $f$ , can be measured by NMR. By measuring the  $\text{oH}_2$  signal of the enriched  $\text{H}_2$  ( $S_e$ ) and comparing it to the signal obtained from the same amount of  $\text{H}_2$  at room temperature ( $S_{rt}$ ). The enrichment fraction is given by [235, 236]:

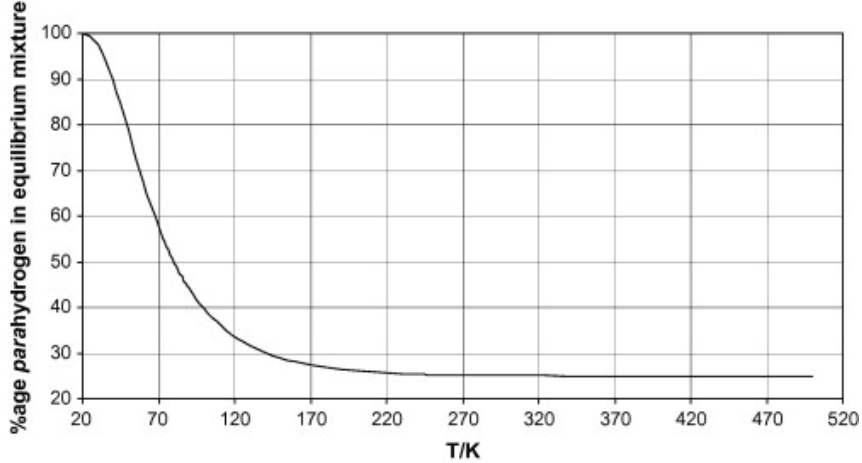


FIGURE 4.2: Calculated percentage of parahydrogen in an equilibrium mixture of *ortho*- and *parahydrogen* gas as a function of temperature using Eqn. 4.7 and  $\theta_R = 87.6$  K.  
Taken from [234].

$$f = 1 - (3S_e/4S_{rt}) \quad (4.9)$$

#### 4.4.2 PASADENA and ALTADENA

'Parahydrogen and synthesis allow dramatically enhanced nuclear alignment' (PASADENA)[237] and 'adiabatic longitudinal transport after dissociation engenders net alignment' (ALTADENA)[238] are subclasses of PHIP experiments characterised by the strength of magnetic field in which the hydrogenation and detection are performed.

The difference between PASADENA and ALTADENA are the  $J$ -coupling regimes in which the reaction and detection happens. The regime is determined by the value of the  $J$ -coupling (in Hz) compared to the value of the difference in chemical shifts of the individual protons. Where the strong regime has  $J$ -couplings that take the approximate value of the difference in chemical shift ( $\frac{\delta\omega}{J} \approx 1$ ), and the weak regime has  $J$ -couplings much smaller than the difference in chemical shift ( $\frac{\delta\omega}{J} \gg 1$ ). Since the chemical shift depends on external magnetic field ( $B_0$ ) and the  $J$ -couplings are independent of field one can select an appropriate magnetic field for the desired experiment. In PASADENA experiments the reaction and detection is carried out at high field ( $> 1$  T) whereas in ALTADENA the reaction is carried out at low field ( $< 10$  mT), and the product is transferred to a high magnetic field for detection[239].

This difference manifests itself as a difference in  $J$ -coupling regimes in the *parahydrogen* derived hydrogens in the product molecule. ALTADENA refers to hydrogens in the strong coupling regime upon addition and PASADENA refers to the weak coupling regime upon addition.

#### 4.4.2.1 Spin Physics

The spin physics of PASADENA and ALTADENA can be interpreted through the density operator formulism. In a PASADENA type experiment, parahydrogen is added to a molecule in high field forming a weakly coupled AX system of the type discussed in 4.4.2. Due to the weak coupling,  $\frac{\delta\omega}{J} \gg 1$ , the eigenbasis is close to the Zeeman basis. The initial density operator,  $\hat{\rho}_{\text{ini}}$ , can be defined using Eqn. 4.2 as:

$$\hat{\rho}_{\text{ini}} = |S^0\rangle \langle S^0| = \frac{1}{2} |\alpha\beta - \beta\alpha\rangle \langle \alpha\beta - \beta\alpha|, \quad (4.10)$$

using the zeeman basis states for a 2 spins system from Eqn. 4.2 the matrix representation is:

$$\hat{\rho}_{\text{ini}} = \frac{1}{2} \begin{pmatrix} 0 \\ 1 \\ -1 \\ 0 \end{pmatrix} \otimes (0 \ 1 \ -1 \ 0) \quad (4.11)$$

$$= \frac{1}{2} \begin{pmatrix} 0 & 0 & 0 & 0 \\ 0 & 1 & -1 & 0 \\ 0 & -1 & 1 & 0 \\ 0 & 0 & 0 & 0 \end{pmatrix}. \quad (4.12)$$

This density operator may also be expressed as a linear combination of operators:

$$\rho_{\text{ini}} = \frac{1}{4} \mathbb{1} - (\hat{I}_{1x}\hat{I}_{2x} + \hat{I}_{1y}\hat{I}_{2y} + \hat{I}_{1z}\hat{I}_{2z}). \quad (4.13)$$

These diagonal elements (populations) do not evolve as these components commute with the Hamiltonian. The off-diagonal elements (coherences) evolve at a rate  $\approx \delta\omega$ .

The Hamiltonian of the product molecule is given by:

$$\hat{H}_{\text{pas}} = 2\pi(\omega_1 \hat{I}_{1z}) + 2\pi(\omega_2 \hat{I}_{2z}) + 2\pi J_{12}(\hat{I}_{1x}\hat{I}_{2x} + \hat{I}_{1y}\hat{I}_{2y} + \hat{I}_{1z}\hat{I}_{2z}), \quad (4.14)$$

as the reaction continues, an ensemble of molecules are hydrogenated at different time points, this gives a new density operator,  $\hat{\rho}_{\text{pas}}(t)$ , expressed as:

$$\hat{\rho}_{\text{pas}}(t) = \exp\{-i\hat{H}_{\text{pas}}t\} \hat{\rho}_{\text{ini}} \exp\{+i\hat{H}_{\text{pas}}t\}. \quad (4.15)$$

Usually, the hydrogenation period is much longer than the coherence evolution. A new average density operator can be found by averaging the ensemble over the reaction

time,  $t_r$  by:

$$\bar{\hat{\rho}}_{\text{pas}}(t_r) = \frac{1}{t_r} \int_{t=0}^{t_r} \hat{\rho}_{\text{pas}}(t) dt, \quad (4.16)$$

these coherences average to zero over the reaction time period and so the density operator becomes:

$$\hat{\rho}_{\text{pas}} = \frac{1}{2} \begin{pmatrix} 0 & 0 & 0 & 0 \\ 0 & 1 & 0 & 0 \\ 0 & 0 & 1 & 0 \\ 0 & 0 & 0 & 0 \end{pmatrix}, \quad (4.17)$$

and can also be written as:

$$\hat{\rho}_{\text{pas}}(t_r) = \frac{1}{4} \mathbb{1} - \hat{I}_{1z} \hat{I}_{2z}, \quad (4.18)$$

Fig. 4.3 shows the eigenstate populations and general simulated spectra of a thermal equilibrium experiment and a PASADENA experiment.

In a usual NMR spectrum, a  $\pi/2$  pulse is used to excite observable single quantum coherences. For a PASADENA signal to be observed, a  $\frac{\pi}{4}$  pulse must be used. The reason becomes clear when examining the effect on  $\hat{\rho}_{\text{pas}}(t_r)$  of a pulse with general tilt angle,  $\theta$ , along the  $y$ -axis:

$$\hat{R}(\theta)_y \hat{\rho}_{\text{pas}}(t_r) = \hat{\rho}_\theta p = \cos^2(\theta) \hat{I}_{1z} \hat{I}_{2z} + \cos(\theta) \sin(\theta) (\hat{I}_{1z} \hat{I}_{2x} + \hat{I}_{1x} \hat{I}_{2z}) + \sin^2(\theta) \hat{I}_{1x} \hat{I}_{2x}, \quad (4.19)$$

using a tilt angle of  $\theta = \pi/2$  would give:

$$\hat{\rho}_{\pi/2p} = \hat{I}_{1x} \hat{I}_{2x}, \quad (4.20)$$

which is unobservable double quantum coherence. However, a pulse with  $\theta = \pi/4$  gives:

$$\hat{\rho}_{\pi/4p} = \frac{1}{2} (\hat{I}_{1z} \hat{I}_{2z} + \hat{I}_{1z} \hat{I}_{2x} + \hat{I}_{1x} \hat{I}_{2z} + \hat{I}_{1x} \hat{I}_{2x}), \quad (4.21)$$

where the  $\hat{I}_{1x} \hat{I}_{2z}$  and  $\hat{I}_{1z} \hat{I}_{2x}$  terms are observable.

In an ALTADENA experiment, the hydrogenation is performed at low field. In this case, when a molecule of hydrogen is added to a substrate the density operator,  $\hat{\rho}_{\text{ini}}$ , is projected onto the new eigenbasis which at low field (where  $\frac{\delta\omega}{J} \ll 1$ ) is the singlet-triplet basis. To a good approximation the only term is the  $|S_0\rangle$  and there is no evolution of the system.

The sample is then transferred to high-field (where  $\frac{\delta\omega}{J} \gg 1$ ). It is done adiabatically, this means that the rate of change of magnetic field,  $dB_0/dt$  being small with respect to the value of the  $J$ -coupling between the protons, squared i.e.  $dB_0/dt < (J_{12})^2$ . As the field increases, the eigenbasis changes from singlet-triplet to the Zeeman basis. The adiabatic change carries the population of the  $|S_0\rangle$  state to the  $|\alpha\beta\rangle$  or  $|\beta\alpha\rangle$  state, depending on which is more energetically more favourable. This change is depicted

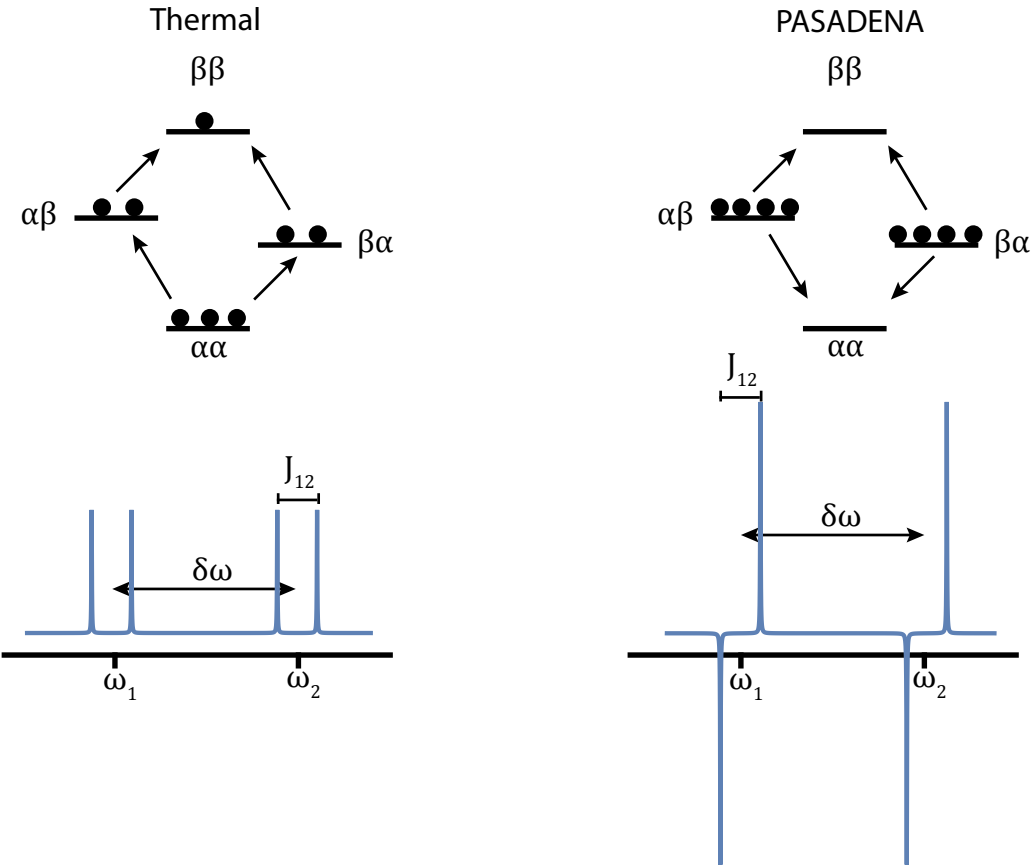


FIGURE 4.3: Above: Populations of states represented as balls in a thermal (left) and a PASADENA experiment. Below: Simulations of spectra arising from adding thermal hydrogen to a molecule (left) and of a PASADENA experiment when adding parahydrogen.

graphically in Fig. 4.4 where  $|\beta\alpha\rangle$  has been arbitrarily chosen as the lower energy state. In the case shown, only one of the four energy levels, namely  $|\beta\alpha\rangle$  is now populated, therefore the density operator,  $\hat{\rho}_{alta}$  is given by:

$$\hat{\rho}_{alta} = |\beta\alpha\rangle \langle \beta\alpha|. \quad (4.22)$$

This leads to [238]:

$$\hat{\rho}_{alta} = \hat{I}_{1z}\hat{I}_{2z} \pm \frac{1}{2}(\hat{I}_{1z} - \hat{I}_{2z}), \quad (4.23)$$

where the positive sign applies if  $J_{12}(\omega_1 - \omega_2) < 0$ , and the negative sign applies in the opposite case.

An r.f. pulse with general angle,  $\theta$ , orientated along the  $y$ -axis gives:

$$\hat{R}(\theta)_y \hat{\rho}_{alta} = \hat{\rho}_\theta = \cos(\theta) \sin \theta (\hat{I}_{1z}\hat{I}_{2x} + \hat{I}_{1x}\hat{I}_{2z}) \pm \frac{1}{2} \sin \theta (\hat{I}_{1x} - \hat{I}_{2x}). \quad (4.24)$$

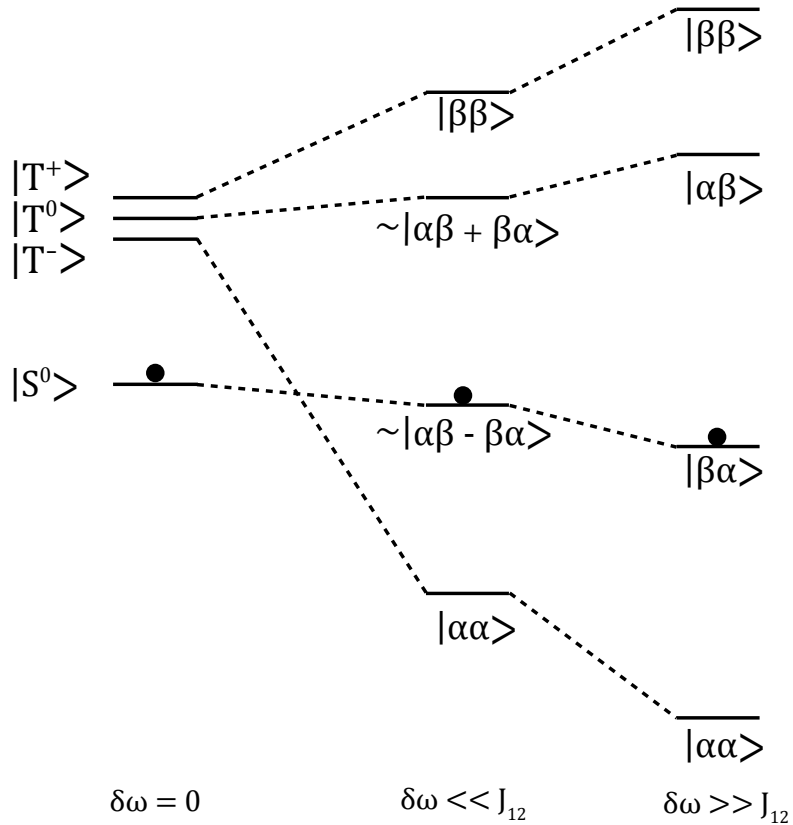


FIGURE 4.4: Correlation diagram for the ALTADENA effect. Hydrogenation at low field populates the singlet state, adiabatically increasing the field carries the population into a high field state.

A pulse with  $\theta = \pi/4$  here yields:

$$\hat{\rho}_{\pi/4a} = \frac{1}{2}(\hat{I}_{1z}\hat{I}_{2x} + \hat{I}_{1x}\hat{I}_{2z}) \pm \frac{1}{2\sqrt{2}}(\hat{I}_{1x} - \hat{I}_{2x}), \quad (4.25)$$

that gives rise to two out of phase doublets shown in Fig. 4.5. However, unlike PASADENA, ALTADENA does not require a  $\pi/4$  pulse so  $\pi/2$  pulses are more common.

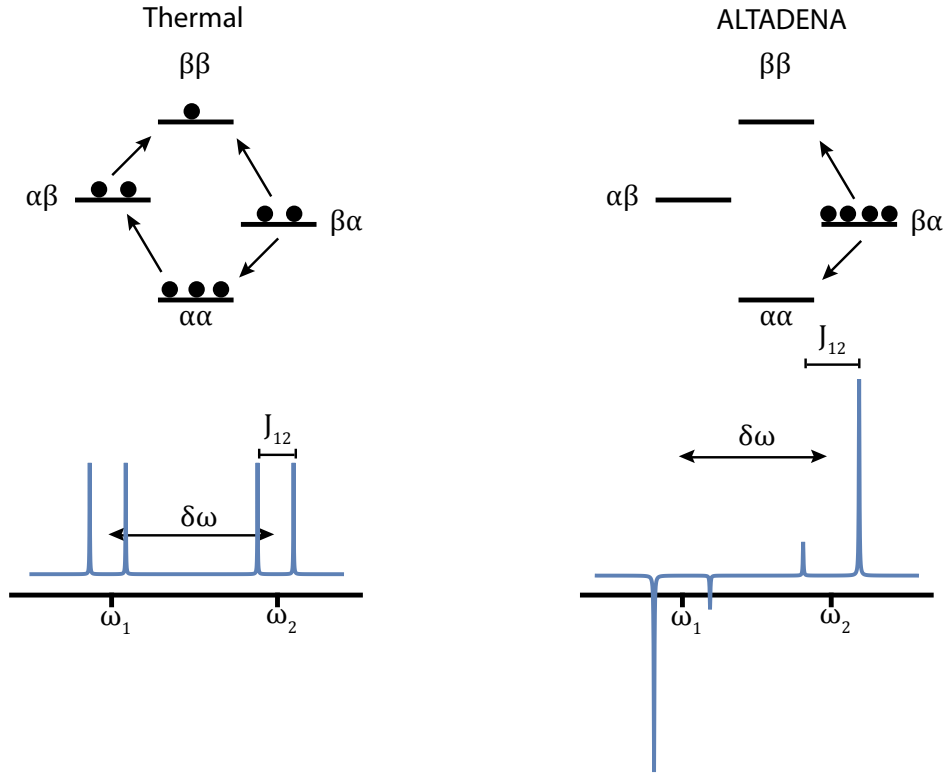


FIGURE 4.5: Top: Populations of Zeeman states represented by balls for thermal(left) and ALTADENA(right) experiments. Bottom: Simulations of a thermal spectrum after applying a  $\pi/4$  pulse and an ALTADENA experiment.

## 4.5 Materials and methods

The microfluidic chips for the PASADENA experiments were constructed from three layers of cell cast PMMA sheet material (Weatherall Equipment). The sheet thickness was  $200 \mu\text{m}$  for the top and bottom layers, and  $500 \mu\text{m}$  for the middle layer. The fluid and gas channels were designed on AutoCAD and cut into the PMMA using a laser cutter (HPC Laser L3040) to a width and depth of  $150 \mu\text{m}$ . The layers were subsequently bonded together with a plasticiser (2.5% v/v dibutyl phthalate in isopropyl alcohol) under heat and pressure (358 K, 3.5 tonnes) [144]. The total internal fluid volume is  $4 \mu\text{l}$ , and the sample chamber is  $2.5 \mu\text{l}$ .

The chip for the ALTADENA experiment was a single  $500 \mu\text{m}$  layer of PMMA. The fluid and gas channels for this device were designed and cut in the same manner as above.

Both devices also employ a poly(dimethyl siloxane) (PDMS) membrane (Shielding Solutions) to facilitate para-H<sub>2</sub> transport, of 1 mm thickness with laser-cut screw holes. The parahydrogen polarization lifetime in the PDMS after O<sub>2</sub> removal was measured to be  $\sim 4$  h.

The PMMA chips and PDMS membrane layer are sealed with a pair of screw-tightened 3D printed (Accura Xtreme, Proto Labs) holders, with fluid and gas in/out ports (to fit Kinesis UK NanoPorts).

For PASADENA experiments, the assembled microfluidic device was put in a transmission line based home-built probe [1]. The device sits between the two stripline planes on a sample holder having sample chamber of the device coinciding with the constriction on stripline planes. PASADENA and 2D NMR experiments were performed at a field strength of 11.7 T with an AVANCE III console. Nutation frequencies for RF pulses were 100 kHz for protons, and 20 kHz for carbon in the case of the HMQC spectrum. 16k data points were acquired over 1.2 s for proton 1D spectra. Saturation recovery experiments used a train of 512  $\pi/2$  pulses separated by a delay of 0.1 ms, followed by a recovery delay, and a  $\pi/4$  excitation pulse. The PH-TOCSY spectrum was acquired using the States-TPPI method, with 256  $t_1$  increments, averaging 8 transients per increment. 2048 complex data points in 0.2 s were acquired for each increment. The PH-HMQC experiment was acquired using the States method, with 128  $t_1$  increments, averaging 8 transients with 2048 complex points over 0.2 s. 1D spectra and 2D spectra were processed using scripts written in Julia [146].

For ALTADENA experiments, the device was placed outside the magnet in order for the hydrogenation to occur at low field. The solution was passed through the device and into a 5 mm NMR tube (NORELL). ALTADENA NMR experiments were performed at a field strength of 16.5 T with a NEO console with cryoprobe. The 1D spectra were processed also using scripts written in Julia [146].

To generate parahydrogen gas at 50% para enrichment, hydrogen gas (purity 99.995%) was passed through a home-built parahydrogen generator containing an iron (III) oxide catalyst cooled to 77 K using liquid nitrogen.

The solution before both experiments contained 20 mM propargyl acetate **2** and 5 mM 1,4-bis(diphenylphosphino)butane(1,5-cyclooctadiene)rhodium tetrafluoroborate **3** in methanol-d<sub>4</sub>. In an attempt to avoid possible spin relaxation or chemical side-reaction effects, dissolved oxygen from the atmosphere was removed by 5 minutes of vigorous helium bubbling.

The parahydrogen gas was delivered through a PTFE tube (1/16 inch O.D., 1/32 inch I.D.) into the 3D printed chip holder, and out via a second PTFE line, using a mass flow controller (Cole-Parmer) to limit the flow to 20 ml min<sup>-1</sup> at an overpressure of 5 bar. Although most of the parahydrogen gas passes directly through the system, some amount dissolves into the PDMS layer, which in terms of H<sub>2</sub> solubility behaves similarly to other organic solvents. The solution was loaded into a 3.5 ml plastic syringe with a Luer lock connection to in-flow PEEK tubing (1/16 inch O.D., 0.007 inch I.D.) leading to the chip. The same tubing was used for the solution out-flow into a container exposed to

a back pressure of 1.5 bar of nitrogen gas, to preventing formation of hydrogen bubbles in the chip. Solution flow into the chip was controlled with a syringe pump (Cole-Parmer).

## 4.6 Results and Discussion

### 4.6.1 Parahydrogen relaxation in PDMS

To determine the hydrogen ortho-para conversion in PDMS, the ortho-para conversion time of H<sub>2</sub> dissolved in PDMS was measured. A high-pressure NMR tube of 5 mm outer diameter (Sigma-Aldrich) was filled with PDMS resin (Sylgard 84, 3M). A teflon capillary of 1/16 inch outer diameter (Sigma-Aldrich) was pushed into the NMR tube along the central axis, and the PDMS was allowed to cure. The capillary was then removed, leaving a cylindrical void in the centre of the NMR tube. The tube was then exposed to vacuum for varying amounts of time, in order to study the conversion effect of the residual oxygen the results of which are shown in Fig. 4.6.

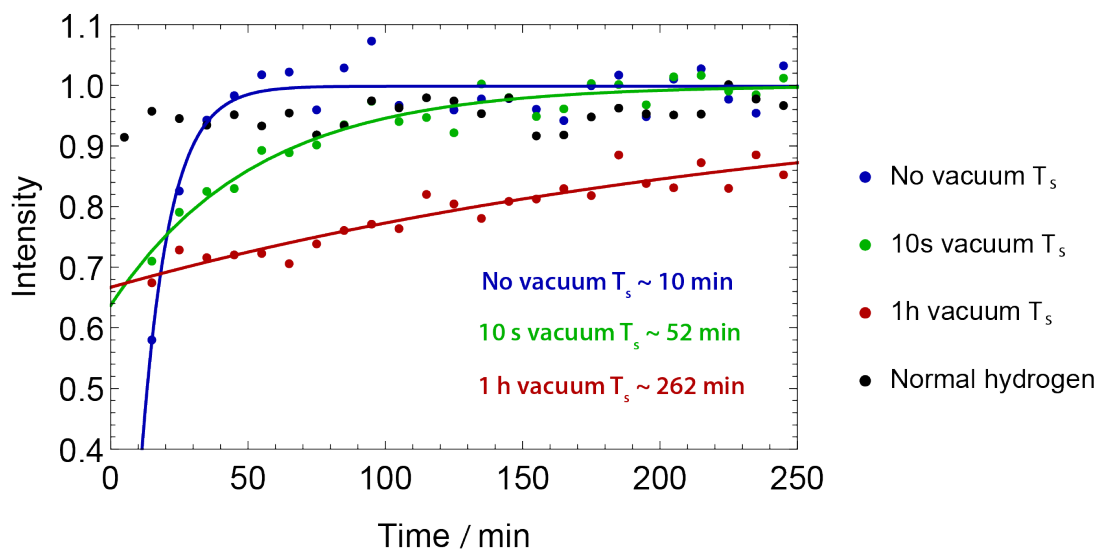


FIGURE 4.6: Ortho-para conversion of hydrogen in PDMS after various times under vacuum.

The detectable thermal signal in the ortho-para conversion experiment is given by  $(1 - \frac{1}{3}(4f - 1))$ , where  $f$  is the para-enrichment level of the H<sub>2</sub> gas. Therefore, the equilibrium ratio of  $f = 0.25$  gives a signal of 1, and pure parahydrogen gas gives no signal. Hence, our signal starting at 50% enrichment should vary from 2/3 to 1. The data was fit to a function of the form  $(A - B e^{-\frac{t}{T_s}})$ , with  $A$ ,  $B$  and  $T_s$  as variables. The  $T_s$  under no vacuum of 10 min lead to the assumption that no significant relaxation would occur during the transport of H<sub>2</sub> through the PDMS membrane.

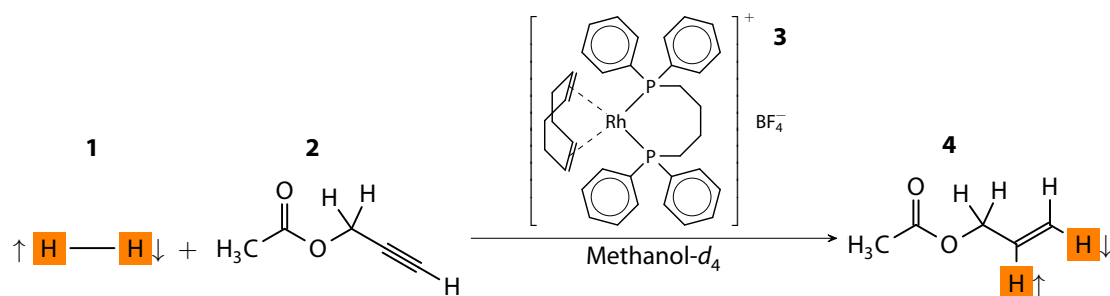


FIGURE 4.7: Scheme of the reaction used in the PHIP@chip experiment. Hydrogen gas **1** enriched in parahydrogen reacts with propargyl acetate **2** in the presence of the Rh catalyst **3** to form allyl acetate **4**.

#### 4.6.2 Reaction Scheme

The hydrogenation reaction system employed in the present work is shown in Fig. 4.7. Parahydrogen-enriched hydrogen gas **1** was allowed to react with propargyl acetate **2**, in the presence of a rhodium catalyst **3**. The substrate **2** was chosen in view of future studies based on side-arm hydrogenation (SAH) [202, 203, 240]. In SAH, the polarisation of the <sup>1</sup>H nucleus is transferred to a neighbouring <sup>13</sup>C and the moiety that has been hydrogenated is removed. SAH techniques can help to bring generality to the PHIP technique as they eliminate the need for the hyperpolarized target molecule to contact unsaturated bonds.

#### 4.6.3 ALTADENA

In order to verify that the parahydrogen transfer on chip was possible, an experiment was performed whereby the parahydrogen transfer was microfluidic and ‘on chip’ but the detection was performed in a conventional NMR tube and probe.

This ALTADENA type experiment involved the addition of para enriched hydrogen gas to propargyl acetate outside the magnetic field in a device shown in Fig. 4.8. This device is a simpler version of the one eventually used. It features 3D printed holders that are used to deliver the gas and liquid as well as seal against any liquid or gas leak. The chip is made from a single 500  $\mu\text{m}$  thick layer of PMMA with serpentine paths for liquid and gas flow. B in the Fig. 4.8 shows the path structure in the chip as well as the hydrogen and fluid paths respectively.

The set-up for this experiment employs a syringe pump, the hydrogenation device outside the magnet and a standard 5 mm NMR tube inside the 16.5 T magnet. The device was pressurised with 5 bar of 50% enriched parahydrogen and allowed to equilibrate for some time. Then, 100  $\mu\text{l}$  was flown through the device at a flow rate of 1000  $\mu\text{l min}^{-1}$  this was done to ensure the sample from the experiment would reside completely in the sensitive area. For the ALTADENA, 350  $\mu\text{l}$  was flown through the device and

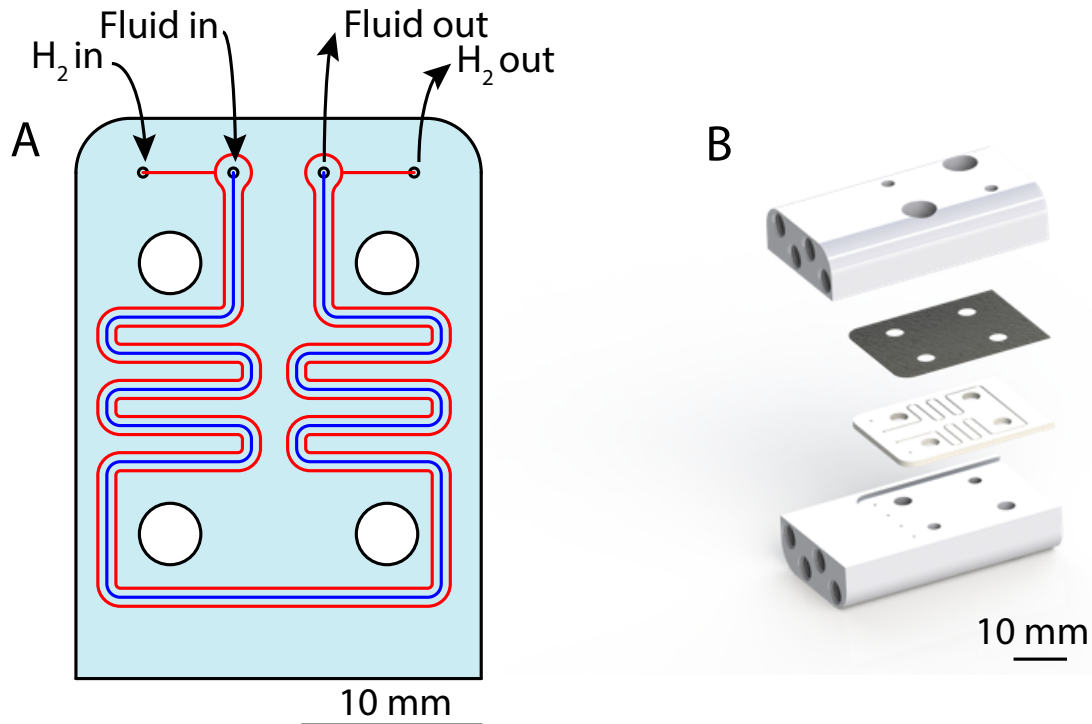


FIGURE 4.8: A) Liquid channel (blue) and hydrogen channel (red) as scored onto the PMMA layer of the device. B) A 3D render of the hydrogenation device used for the ALTADENA experiments.

collected in the magnet. A  $\pi/2$  pulse was applied and the spectra recorded the result of the experiment is shown in Fig. 4.9.

A comparison is shown between scans taken of the same experiment, in Fig. 4.9 i) spectra from an experiment with thermal hydrogen and ii) one with parahydrogen. The parahydrogen ALTADENA signal (ii) exhibits the characteristic inverted peaks and a much higher signal to noise ratio (SNR) and gives enhancement by comparison of the SNR of around 200. This result provided a proof of principle that parahydrogenation induced polarization (PHIP) on a chip was possible by bubble free transfer through a PDMS membrane in our devices.

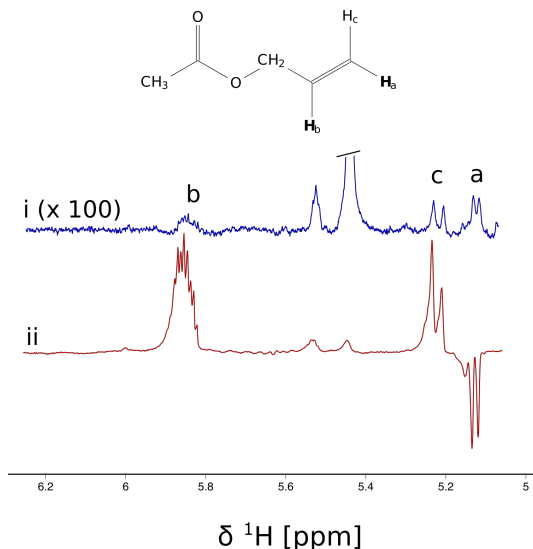


FIGURE 4.9: Spectra obtained from i) a thermal hydrogenation and ii) a parahydrogenation of propargyl acetate to give allyl acetate with hydrogens derived from parahydrogen labelled a and b. By comparison of SNR the enhancement for the ALTADENA experiment is 200.

#### 4.6.4 PASADENA

Fig. 4.10 shows the microfluidic device used for the present study. It consists of a chip made from PMMA, which houses a sample chamber of 2.5 L volume that aligns with the transmission line detector of a home-built NMR probe assembly, which was fitted inside of an 11.7 T NMR magnet. Fluid is flowed through the chip by means of a syringe pump installed outside of the magnet bore; connections are made through threaded ports in the two 3D-printed holders shown in Fig. 4.10b. Para-enriched  $\text{H}_2$  gas at 5 bar above ambient pressure flows through a second channel in the chip, which runs in the immediate vicinity of the liquid channel. A depiction of the set-up is given in Fig. 4.11.

The chip consists of three laser-cut layers of poly methylmethacrylate (PMMA) bonded together, as shown in Fig. 4.10b. Channels in the left part of the chip, where it is clamped between the holders, are cut through the top layer, while they are scored into the middle layer of the chip (and hence sealed from the outside) in the free part of the device. Within the clamps, the exposed channels are sealed by means of a PDMS membrane. The flowing liquid as well as the pressurised hydrogen gas are therefore exposed to the PDMS layer, which serves as a diffusion bridge for the hydrogen. The holders, made by 3D printing, keeps the membrane and the chip aligned, and maintains mechanical pressure to ensure sealing. Channels inside the holders guide the fluid and gas to and from the four access points at the top end of the chip, as shown in Fig. 4.10b. The PDMS membrane acts both as a diffusion conduit for hydrogen gas and as a fluid seal. In a crucial difference to the otherwise similar geometry of the hydrogenation chip used by Bordonali et al[241], the gas and liquid channels are arranged side by side,

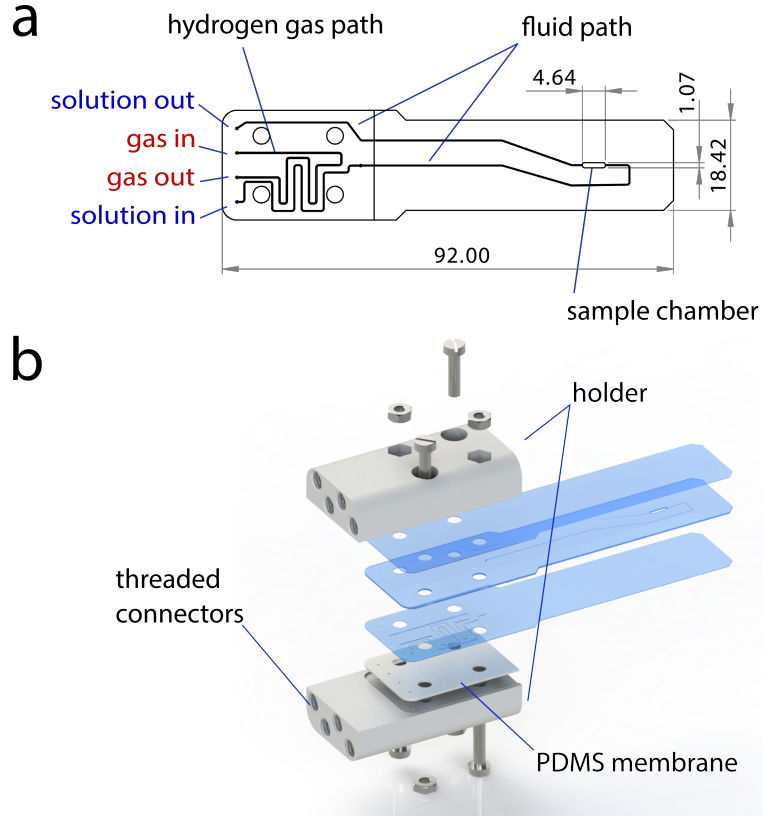


FIGURE 4.10: Overview of the PHIP@chip device. a: outline drawing of the chip (dimensions in mm). b: CAD rendering of the chip assembly with individual chip layers separated, consisting of the PMMA chip, PDMS membrane, and two 3D printed holders with threads for the gas and fluid connections. The hydrogen gas diffuses through the PDMS membrane into the flowing liquid.

and molecular hydrogen diffuses through the bulk of the PDMS membrane rather than across the membrane. Clamping the PDMS membrane onto the chip using the holders, makes it possible to use large gas pressures (up to 5 bar in the present experiments). This would be difficult to achieve in the chip presented by Bordonali et al, which has the liquid and gas channels arranged on opposite sides of the membrane.

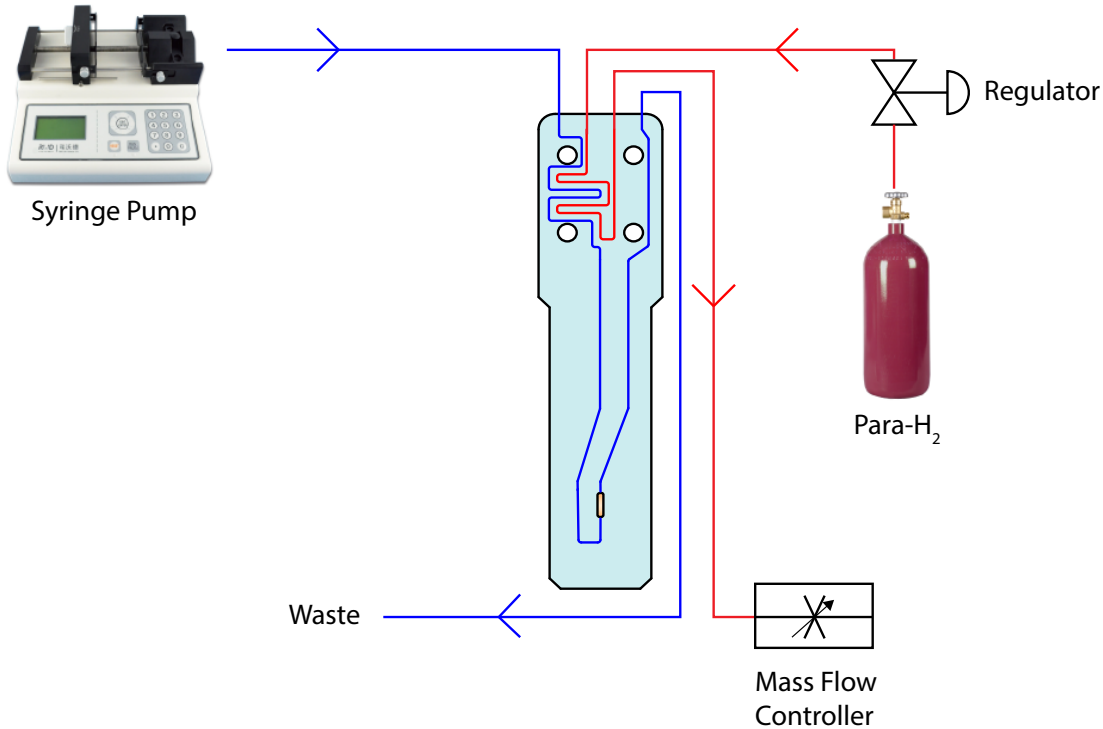


FIGURE 4.11: Drawing of PHIP@chip setup. It shows the solution (blue line) of propargyl acetate, catalyst and methanol being fed into the magnet via a syringe pump. Simultaneously, parahydrogen (red line) is fed in at the desired pressure and regulated by a mass flow controller to a flow rate of  $20 \text{ ml min}^{-1}$ . Both of these are fed into the microfluidic device depicted in Fig. 4.10

#### 4.6.5 Signal Analysis

Fig. 4.12a shows a single-scan proton NMR spectrum obtained from a steady-state PHIP@chip experiment (top trace), compared to the spectrum obtained without parahydrogen (bottom trace). The hyperpolarized spectrum is dominated by an antiphase doublet, centred at 5.17 ppm, and an antiphase multiplet at 5.92 ppm, corresponding to protons in the H<sup>a</sup> and H<sup>b</sup> positions of the hydrogenation product **4**. The PDMS membrane is equilibrated with para-enriched hydrogen gas, which is supplied from an aluminium storage tank at a regulated pressure of 5 bar. The gas flow rate is kept constant at  $20 \text{ mL min}^{-1}$  by means of a mass flow controller placed after the chip. This ensures that the gas channel always contains fresh para-enriched hydrogen gas at the design pressure of 5 bar. The fluid channel of the chip is pre-filled with a solution of 20 mM precursor **2** and 5 mM catalyst **3** in methanol-d<sub>4</sub>. NMR spectra are acquired every 30 s, using a  $\pi/4$  excitation pulse. The fluid channel is connected to a syringe pump situated outside the NMR magnet. The liquid flow is started by setting the target flow rate on the syringe pump to  $8 \text{ L min}^{-1}$  (marked by an arrow Fig. 4.12b). The NMR signal intensity begins to rise about 30 s later, and reaches a steady state after about two minutes.

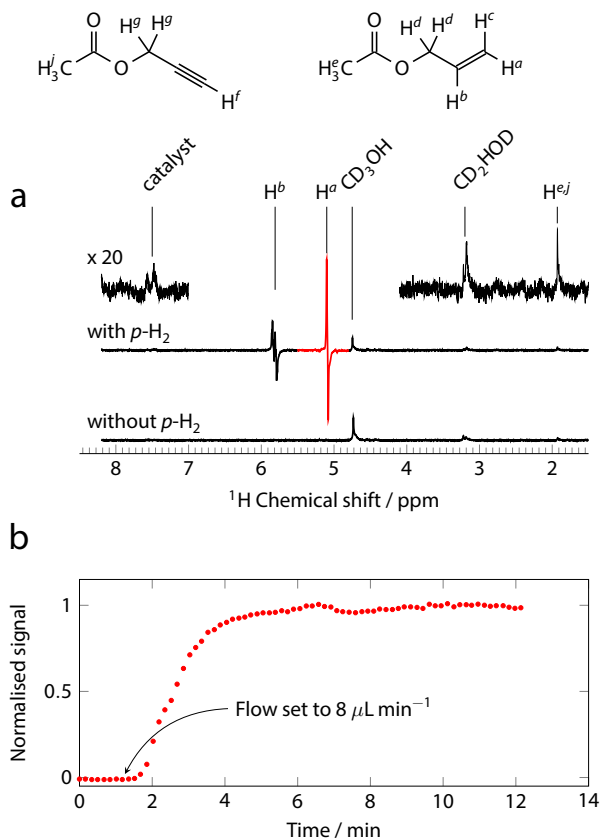


FIGURE 4.12: a: Single-scan proton NMR spectrum obtained with parahydrogen at 5 bar using the PHIP@chip setup at a continuous flow rate of  $8 \mu\text{L min}^{-1}$  (top trace with enlargement). Antiphase doublets from the two hyperpolarized protons H<sup>a</sup> and H<sup>b</sup> are clearly visible at 5.2 ppm and 5.9 ppm, respectively. Without parahydrogen, these signals are not observed (bottom trace). b: Buildup of the hyperpolarized signal (H<sup>a</sup>) after initiation of flow.

Using normal hydrogen gas, a fully labelled spectrum of the reaction mixture was obtained using a lower flow rates whilst maintaining the 5 bar of hydrogen pressure. This allowed the solution to saturate with methanol and facilitated the quantification of the product and dissolved hydrogen. A fully labelled spectrum obtained using a flow rate of  $2 \mu\text{L min}^{-1}$  is shown in Fig. 4.13

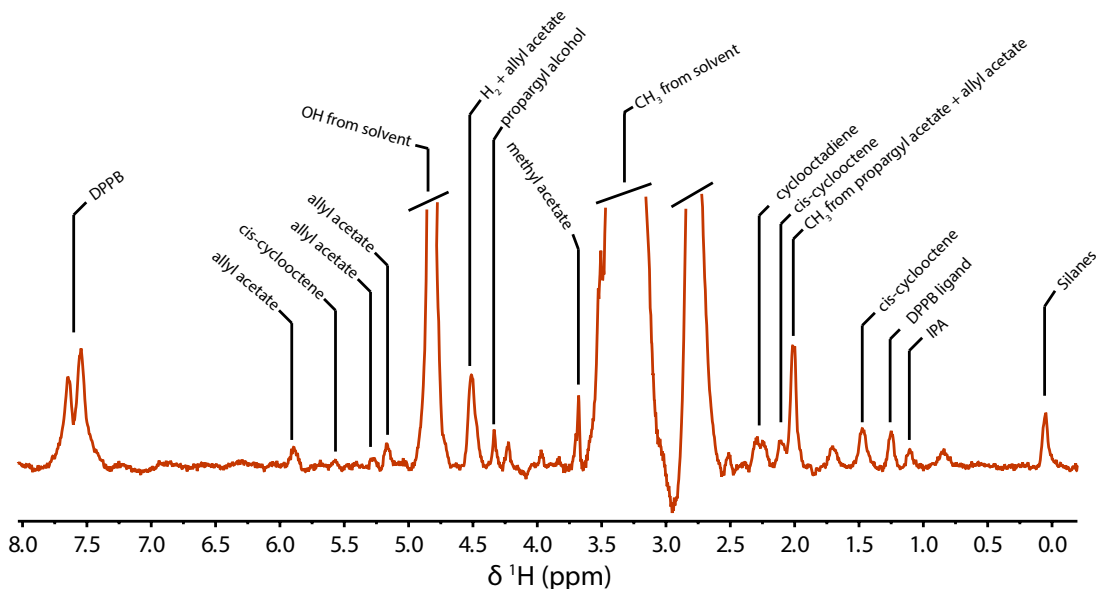


FIGURE 4.13: Labelled  $^1\text{H}$  spectrum acquired using a flow rate of  $2\mu \text{lmin}^{-1}$  and a normal hydrogen pressure of 5 bar. The spectrum was collected using 64 transients with a delay of 5 seconds.

#### 4.6.6 Hydrogen Transport

The hydrogen transport through the membrane and its uptake into the flowing liquid was simulated using two coupled finite element models: a dilute species diffusion model for hydrogen gas in the PDMS membrane, and a dilute species diffusion and convection model for hydrogen dissolved in the flowing liquid. The hydrogen partial pressures at the liquid/PMDS interface are constrained to be equal, and the hydrogen partial pressure at the gas/PDMS interface was set to a fixed value of 5 bar. Fig. 4.14a shows the diffusive flux of hydrogen through the PDMS membrane. Since the gas/PDMS interface acts as a source, and the liquid/PMDS interface as a sink for hydrogen, the flux is strongest where the two channels are in close proximity. At the lowest flow rate, significant transport only takes place in a very small area, and the liquid is saturated with hydrogen within the first few mm of the path which is in contact with the PDMS. The higher the flow rate, the further the area of significant flux extends downstream. At about  $10 \text{lmin}^{-1}$ , the hydrogen flux covers the entire length of the area between the liquid and gas channel interfaces. The finite element model also predicts the resulting concentration of hydrogen in the liquid (methanol) as a function of flow rate. This is shown by the solid line in Fig. 4.14b. The circles represent NMR measurements. At flow rates between 2 and  $10 \text{lmin}^{-1}$ , experimental results are in good agreement with the simulation. At higher flow rates, however, the experimentally observed hydrogen concentrations are significantly lower than the predictions. It is currently unclear what causes this discrepancy; possibly high flow rates lead to deformation of the PDMS layer over the liquid channel and thus change the uptake geometry. At flow rates below

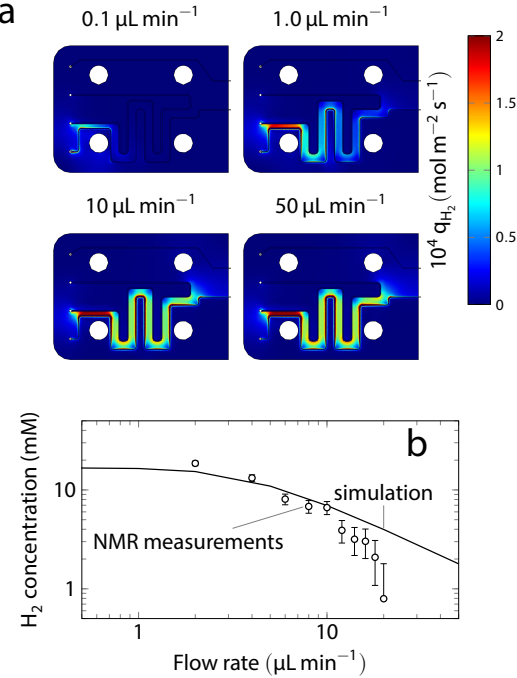


FIGURE 4.14: Finite element simulation of hydrogen uptake. a: Diffusive hydrogen flux in the PDMS membrane for different liquid flow rates; b: final hydrogen concentration in flowing methanol as a function of flow rate. Solid line: simulation, open circles: NMR measurements.

$10\text{ L min}^{-1}$ , the simulation and experiments both indicate that the flowing solvent is nearly saturated with hydrogen.

#### 4.6.7 Sensitivity and Limit of Detection

Clearly, the steady-state signals observed at constant flow rate are the result of a dynamic equilibrium between the rate of hydrogenation, the rate of transport of the hydrogenated product to the sample chamber and its removal from it, and spin-lattice relaxation. In order to probe the interplay of these factors, the NMR signal was suppressed by saturating the spin populations with a train of 512  $\pi/2$  pulses separated by  $100\ \mu\text{s}$  delays. The signal intensity was then measured as a function of the delay between the end of the saturation train and the NMR excitation pulse. Fig. 4.15a shows an example of the data thus obtained at a flow rate  $q = 8\ \text{L min}^{-1}$ . The signal increases rapidly after saturation, reaching steady-state levels after about 10 s.

The intensity of the steady-state NMR signal exhibits a clear maximum with flow rate (Fig. 4.15b), reflecting a balance between hydrogen uptake, reaction kinetics, and spin-lattice relaxation. The optimum, with the largest signal at saturation, is reached at a flow rate of  $8\ \text{L min}^{-1}$ . The nature of the stationary state established in the system at each flow rate becomes clearer if the saturation recovery data is plotted in terms of the volume displaced during the saturation recovery time  $q\tau$ , rather than the recovery time

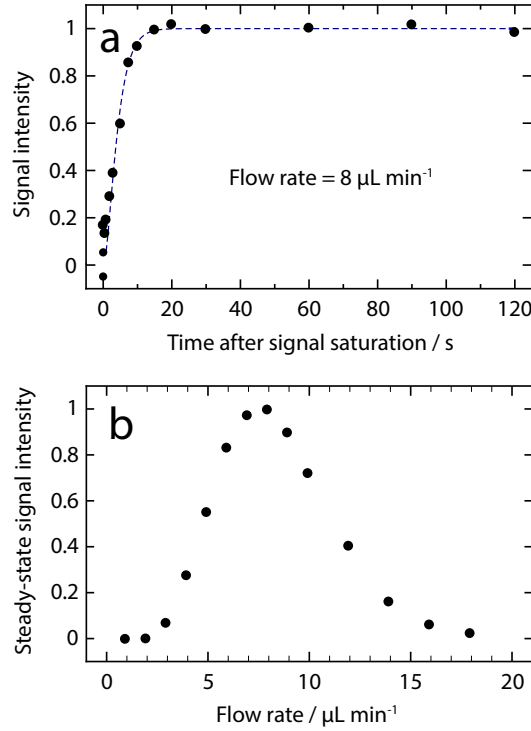


FIGURE 4.15: Saturation recovery results. a: Signal buildup at constant flow rate after saturation (solid dots: measured data points, the dashed line is a guide to the eye); b: Magnitude of the steady-state signal after full recovery (at least 100 s after saturation) as a function of flow rate. A clear maximum at  $8 \mu\text{L min}^{-1}$  is observed.

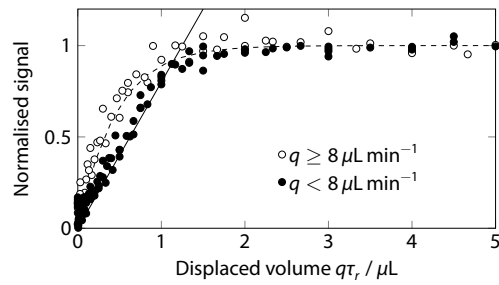


FIGURE 4.16: Signal recovery after saturation, normalised by the maximum signal observed at long recovery times. The horizontal axis is the volume moved through the chip during the recovery time  $\tau_r$ , i.e.,  $q\tau_r$ , where  $q$  is the flow rate. Filled circles correspond to flow rates below the optimum ( $q < 8 \mu\text{L min}^{-1}$ ), whereas open circles are obtained at flow rates  $q \geq 8 \mu\text{L min}^{-1}$ . The solid and dashed lines are guides to the eye for the solid and open circle data points, respectively.

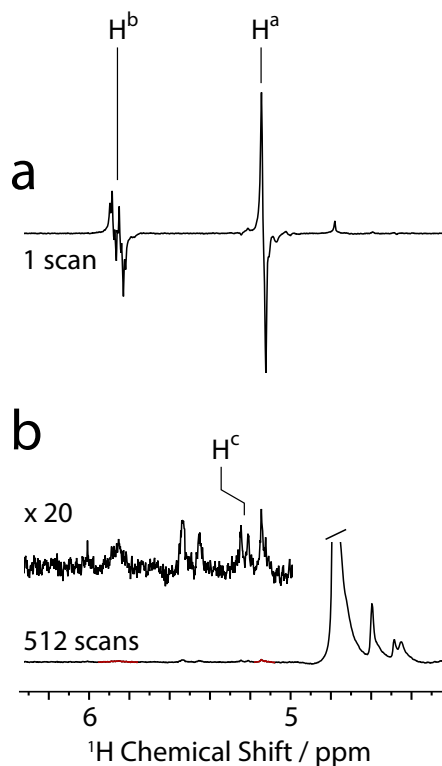


FIGURE 4.17: a: Single-scan steady-state spectrum obtained at the optimum flow rate with para-enriched  $\text{H}_2$ ; b: spectrum obtained at the same flow rate with hydrogen gas in thermal equilibrium. 512 transients have been averaged. Signal enhancement by PHIP was determined by comparing the integral of the positive lobe of the  $\text{H}^a$  signal in spectrum a to the integral of the corresponding (purely absorptive) peak in spectrum b.

itself, and normalised to the steady-state signal intensity at each flow rate, as shown in Fig. 4.16. At flow rates below the intensity maximum at  $q < 8 \text{ L min}^{-1}$  (solid circles), the data points collapse onto a curve that shows an initial linear increase up to a displaced volume of about  $1 \mu\text{L}$ , followed by rapid saturation to the steady-state value. This behaviour clearly indicates that the signal recovery in this regime is dominated by the convective fluid transport. At these flow rates, a constant concentration of hyperpolarized material is established in the flowing liquid upstream of the sample chamber, and is simply carried back into view of the NMR detector after the saturation pulses end. The maximum signal is reached after a volume of about  $1.5 \mu\text{L}$  has been displaced. This is less than the capacity of the sample chamber, reflecting the uneven velocity distribution inside it. At flow rates above the optimum ( $q \geq 8 \text{ L min}^{-1}$ ), a somewhat different behaviour is observed. The initial recovery rate is faster (Fig. 4.16, open circles), and appears to follow an exponential rather than linear shape. This suggests that at these flow rates, the stationary state is not yet established at the point where the liquid enters the sample chamber, and therefore, the observed recovery is dominated by the ongoing hydrogenation reaction.

In order to determine the sensitivity of detection of the hydrogenation product

at the optimum flow rate, the experiment was repeated using normal hydrogen. In this case, the signal from protons H<sup>a</sup> and H<sup>b</sup> of the hydrogenation product **4** are too weak to be observed above the noise in a single scan. Fig. 4.17 compares the hyperpolarized signal (a) to the averaged signal of 512 transients obtained with hydrogen in thermal equilibrium (b).

Since the methyl group in the precursor and the hydrogenation product contribute to the same signal at 2.05 ppm (signal labelled H<sup>e,j</sup> in Fig. 4.12a), this signal can be used as a calibration standard, with a concentration of 20 mM which is unaffected by the hydrogenation reaction. By comparing this integral to that of the signal from the H<sup>a</sup> protons, the concentration of hydrogenated product can be quantified. At a flow rate of 8 L min<sup>-1</sup>, an allyl acetate (product) concentration of (0.29 ± 0.05) mM was found, corresponding to a total of (0.725 ± 0.125) nmol in the 2.5 L sample volume.

This quantity can be used to determine the limit of detection of the hyperpolarized product. The signal/noise ratio (SNR) in the spectrum shown in Fig. 4.17a is 400(±10%), and the line width is 6 ± 0.5 Hz. The normalised limit of detection is given by Eqn. 2.235

$$\text{nLOD}_\omega = \frac{3n}{\text{SNR} \sqrt{\Delta f}},$$

where  $n$  is the amount of sample and  $\Delta f$  is the signal bandwidth. In the present case, one finds nLOD <sub>$\omega$</sub>  = (2.2 ± 0.4) pmol  $\sqrt{s}$ . Limits of detection in this range have so far only been reported in very limited circumstances, including chemically-induced dynamic nuclear polarization (CIDNP) [242], or by making use of unconventional low-field detection systems such as force-detected magnetic resonance or optical detection methods[173–183]. In the present case, conventional inductive detection is used, and the full resolution and specificity that make high-field NMR a useful analytical tool are retained.

The mass limit of detection (LOD) for protons at a magnetic field of 14.1 T (corresponding to a proton Larmor frequency of 600 MHz) in state-of-the-art commercial NMR probes with a conventional sample volume of 0.5 ml is approximately 100 nmol  $\sqrt{s}$ . Microfluidic NMR systems can make use of miniaturised NMR detectors, which benefit from a favourable scaling of the mass sensitivity with detection volume [90, 123, 156]. At a size scale of 2.5  $\mu$ l, a mass sensitivity around 1 nmol  $\sqrt{s}$  has been reported [2]. However, due to the limited volume in such systems, the *concentration* sensitivity is very poor, such that only compounds present at mM levels can be quantified in microfluidic NMR systems. This situation gets worse as the detector volume decreases. By contrast, many samples of interest, such as metabolites in microfluidic culture systems, are only present at  $\mu$ M levels.

In the present case, the concentration limit of detection from Eqn. 2.236 is

$$\text{cLOD}_\omega = \frac{\text{nLOD}_\omega}{V_s} = (0.88 \pm 0.16) \mu\text{M}\sqrt{s}. \quad (4.26)$$

From the ratio of the signal intensities in the thermal and hyperpolarized spectra shown in Fig. 4.17a and b, it is possible to estimate the  $^1\text{H}$  polarization levels. In the thermal spectrum, the SNR is about 5:1, whereas it is 400:1 in the hyperpolarized spectrum. The thermal spectrum is obtained from 512 transients, therefore the single transient thermal SNR would be  $5/\sqrt{512} \approx 0.22$ . This leads to a signal enhancement factor of  $\epsilon \approx 400/0.22 \approx 1800$ .

This can be compared to the expected signal enhancement given the enrichment level of para-hydrogen used in the experiment. The ideal enhancement factor is given by

$$\epsilon_{id} = \frac{4x_p - 1}{3\sqrt{2}} \frac{2k_B T}{\hbar\gamma B_0}, \quad (4.27)$$

where  $x_p$  is the mole fraction of parahydrogen in the feed gas,  $\gamma$  is the magnetogyric ratio,  $B_0$  is the magnetic field, and  $\hbar$  and  $k_B$  are Planck's and Boltzmann's constants, respectively. The factor  $\frac{1}{\sqrt{2}}$  reflects the use of a  $\pi/4$  pulse for the hyperpolarized experiment. At a temperature of  $T = 298$  K and a magnetic field of 11.7 T, and with  $x_p = 0.5$ , this yields  $\epsilon_{id} \approx 5900$ , which is a factor of 3.3 larger than the experimentally observed enhancement factor. Therefore, about 2/3 of the theoretically available spin order is lost to relaxation under the present experimental conditions.

#### 4.6.8 2D NMR

A great advantage of the continuously operating microfluidic PHIP system is the ability to acquire many transients in succession under virtually unchanged conditions. This is difficult to achieve with bubbling hydrogen through a solution. As a consequence, hyperpolarized multi-dimensional NMR spectra [205, 207–209, 243, 244] have been recorded either using automated reactors combined with NMR flow probes, [208, 209] or using ultrafast acquisition techniques [207, 243, 244].

The PHIP@chip setup allows straightforward acquisition of 2D spectra, using conventional  $t_1$  incrementation. To demonstrate this, 2D TOCSY (Total Correlation Spectroscopy) and HMQC (Heteronuclear Multiple Quantum Coherence) NMR spectra of the reaction mixture at a flow rate of  $8 \text{ L min}^{-1}$  have been performed. The conventional pulse sequences were modified by replacing the initial  $\pi/2$  pulse with a  $\pi/4$  pulse; these experiments are referred to as “PH-TOCSY” (parahydrogen TOCSY) and “PH-HMQC” (parahydrogen HMQC).

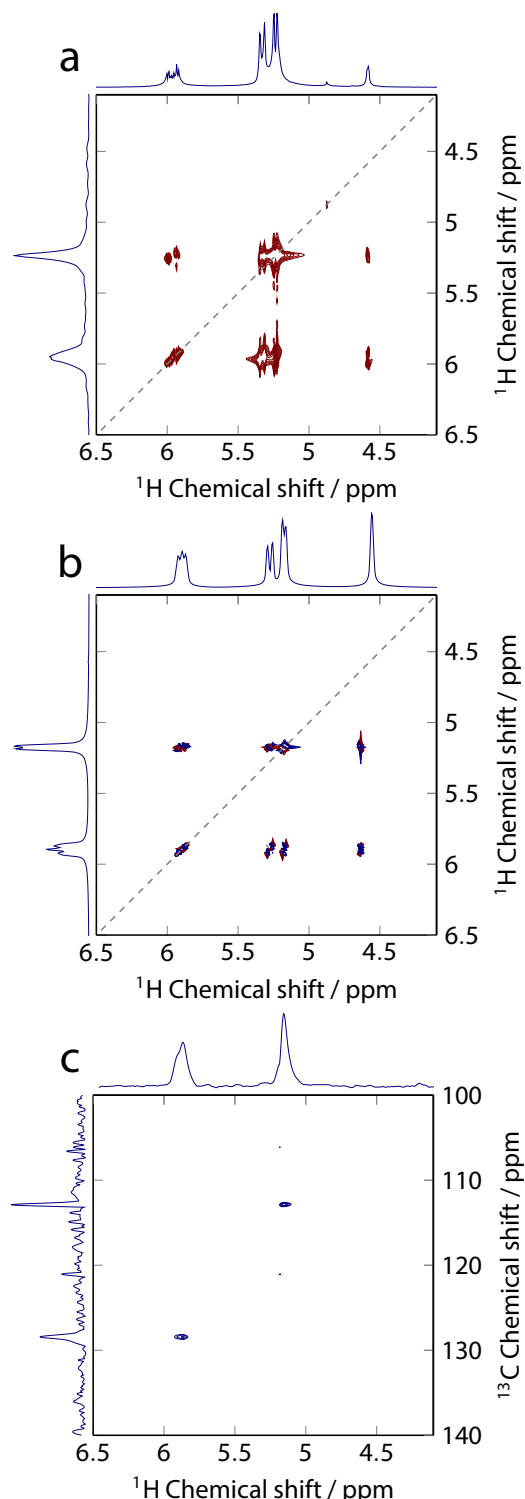


FIGURE 4.18: The continuous flow PHIP@chip approach allows acquisition of two-dimensional spectra with very high sensitivity. a: PH-TOCSY spectrum of the hyperpolarized reaction mixture, flowing at  $8 \mu\text{L min}^{-1}$ . b: Simulated PH-TOCSY spectrum. The diagonal in the spectrum is marked by a dashed grey line. Only the protons originating from parahydrogen give signals on the diagonal; the polarization is transferred to the other locations by the isotropic mixing sequence. Both PH-TOCSY spectra are plotted in magnitude mode. c:  $^1\text{H}-^{13}\text{C}$  PH-HMOC spectrum showing two separate multiplets, each correlating one of the two hyperpolarized protons with the directly bonded  $^{13}\text{C}$  spin.

A PH-TOCSY spectrum acquired in 20 min is shown in Fig. 4.18a. A *thermal equilibrium* TOCSY spectrum of this compound would be expected to contain diagonal peaks connecting the identical nuclear spins in the two acquisition dimensions, and off-diagonal peaks connecting  $J$ -coupled spins. In the PH-TOCSY experiment, the diagonal peaks only appear for the two parahydrogen proton signals, because they are the only spins significantly polarised in the indirect dimension. The other protons are only polarised during the isotropic spin-mixing step of the pulse sequence, and hence do not appear in the indirect dimension. These protons only produce off-diagonal peaks, connecting them to the parahydrogen pair. As shown in Fig. 4.18b, the simulated spectrum closely corresponds to the experimentally observed one.

A *thermal equilibrium* TOSCY spectrum of this compound would be expected to contain diagonal peaks connecting the identical nuclear spins in the two acquisition dimensions, and off-diagonal peaks connecting  $J$ -coupled spins. In this *hyperpolarized* experiment, the diagonal peaks only appear for the two parahydrogen proton signals, because they are the only spins significantly polarised in the direct detection dimension. The other protons are only polarised during the isotropic spin-mixing step of the pulse sequence, and hence don't appear in the direct dimension. These protons only produce off-diagonal peaks, connecting them to the parahydrogen pair.

A PH-HMQC spectrum acquired in 60 min is shown in Fig. 4.18c. It contains two peaks, linking the parahydrogen protons to the  $^{13}\text{C}$  spins to which they have a direct  $^1J_{\text{CH}}$  coupling. An experiment of this kind, in which signals are detected at full natural abundance of the  $^{13}\text{C}$  spins (about 1%) in a  $2.5 \mu\text{L}$  detection volume, is only possible due to both the high polarization levels and stability of the system.

The results in Fig. 4.18 show that the hyperpolarized spin order can be spread to other protons in the molecule by the application of the isotropic mixing sequence MLEV-17 [245, 246] prior to 1D signal acquisition. This simple trick allows one to hyperpolarize any protons that are  $J$ -coupled to the parahydrogen pair, which makes the technique more general.

Much ongoing research in the field of hyperpolarization is motivated by in-vivo applications, where hyperpolarized compounds are used as magnetic resonance imaging contrast agents [247]. Mostly, this involves transferring the nuclear spin polarization after hydrogenation to other nuclei ( $^{13}\text{C}$ ,  $^{15}\text{N}$ ,  $^{31}\text{P}$ ) with lower magnetogyric ratios, where spin-lattice relaxation times are longer. [202, 248, 249] Many of these approaches use zero or very low magnetic fields for hydrogenation and polarization transfer. This has the advantage that near magnetic equivalence between the two added protons is maintained through the reaction, leading to longer lifetimes [198–203, 250, 251]. The present work opens a complementary strategy, in that the hydrogenation is done at high field. Deleterious effects of relaxation are minimised by the proximity of the site of hydrogenation to the point of use. Arguably, this approach has advantages in the

context of microfluidic systems, where only small quantities of hyperpolarized agents are needed.

## 4.7 Conclusions

The combination of a highly efficient transmission-line NMR micro detector with parahydrogen induced hyperpolarization leads to an unprecedented sensitivity in inductively detected NMR, with a mass limit of detection around  $2.2 \text{ pmol} \sqrt{\text{s}}$ . This corresponds to a concentration sensitivity of less than  $1 \mu\text{M} \sqrt{\text{s}}$ , which, to our knowledge, has not previously been reached at the volume scale of  $2.5 \mu\text{L}$ . This opens the perspective to be able to study chemical processes involving low-abundance species in mass-limited samples. Obviously, such applications require preparation of a hyperpolarized reactant. As the foregoing study shows, the necessary chemistry can be integrated in a microfluidic system. It should be noted that parahydrogen enriched to 50% (compared to 25% at thermal equilibrium) has been used; the sensitivity could easily be boosted by a factor of three by using pure parahydrogen. Microfluidic systems hold great potential in combination with hyperpolarized NMR. All hyperpolarization techniques require co-ordinated manipulation of fluids and spin transformations. The results shown in the foregoing demonstrate that in the case of parahydrogen-induced polarization, this can be assisted considerably by integrating some of the necessary chemical steps on a microfluidic chip. Parahydrogen can be delivered to a reactive solution through a PDMS membrane at sufficient rate to achieve significant levels of hyperpolarization; dissolution and transport of hydrogen in PDMS does not appear to lead to significant ortho-para equilibration. The highly stable continuous operation of the PHIP@chip system allows quantitative studies of the hydrogenation kinetics, and the relevant relaxation processes. This is demonstrated by the dependence of the steady-state signal intensity on flow rate and the recovery of the hyperpolarized signal after saturation (Fig. 4.15).

The successful demonstration of PHIP on a chip opens important perspectives. Conditions can be optimised for continued production of hyperpolarized metabolites, which opens the possibility to conduct in-situ metabolic studies in microfluidic cultures of cells, tissues, and organisms. While the hyperpolarized compound used here, allyl acetate, is not a metabolite per se, the production of hyperpolarized metabolic species through PHIP has been demonstrated before [194, 201, 203, 250, 252, 253]. Some metabolites, such as fumarate, can be generated directly by hydrogenation of an unsaturated precursor [250]. Aime et al. have proposed a more generally applicable method [252], which relies on the metabolite bound to an alkyne sidearm through an ester linkage. After hydrogenation, the polarization is transferred to a  $^{13}\text{C}$  nucleus in the metabolic moiety, and the sidearm is cleaved. PHIP@chip opens the possibility of implementing these additional production steps on the same chip. While previous demonstrations of sidearm hydrogenation have been carried out at low magnetic field, it

may be possible to adapt recently developed efficient methods for heteronuclear polarization transfer at high field[204] to this purpose. In turn, this may enable integration of the hyperpolarized metabolite generation with an on-chip culture of cells or other biological systems. Thanks to its stability, the setup provides a convenient means to optimise pulse sequences and reaction conditions for producing hyperpolarized targets.

The successful demonstration of PHIP on a chip opens important perspectives. Conditions can be optimised for continued production of hyperpolarized metabolites, which opens the possibility to conduct in-situ metabolic studies in microfluidic cultures of cells, tissues, and organisms. While the hyperpolarized compound used here, allyl acetate, is not a metabolite per se, the production of hyperpolarized metabolic species through PHIP has been demonstrated before [201, 203, 247, 250, 252, 253]. Some metabolites, such as Fumarate [250], can be generated directly by hydrogenation of an unsaturated precursor. Aime et al. have proposed a more generally applicable method [252], which relies on the metabolite bound to an alkyne sidearm through an ester linkage. After hydrogenation, the polarization is transferred to a  $^{13}\text{C}$  nucleus in the metabolic moiety, and the sidearm is cleaved. PHIP@chip opens the possibility of implementing these additional production steps on the same chip. In turn, this may enable integration of the hyperpolarized metabolite generation with an on-chip culture of cells or other biological systems. Thanks to its stability, the setup provides a convenient means to optimise pulse sequences and reaction conditions for producing hyperpolarized targets.

# Chapter 5

## An NMR compatible on-chip Peristaltic Pump

### 5.1 Introduction

In this chapter, the design and implementation of an NMR compatible, low dead volume, microfluidic pump will be discussed. The goal is the development of a device that is capable of exchanging and mixing two fluids in a controlled manner, and acquiring high resolution NMR spectroscopy. Microfluidic pumping and mixing plays an integral role in many biological and chemical applications, such as DNA analysis [254, 255], protein folding [256], enzyme assays [257, 258], chemical synthesis [259, 260], and kinetic studies [3, 261]. These applications use a wide variety of techniques to detect and characterise samples, including fluorescence spectroscopy [255], mass spectrometry [259], and UV-vis spectroscopy [261]. In comparison to these techniques, NMR typically has a higher limit of detection, however, NMR can provide quantitative, system level information in a few scans and due to its non-invasive, non-destructive nature can give insight into living systems *in situ* and allows for longitudinal studies of them. However, in order to keep these systems alive, and truly replicate *in vivo* conditions, they need fresh supplies of oxygen and nutrients. One way of achieving this is by perfusion of liquid that has been exposed to fresh supplies of oxygen. Perfusion can be accomplished by pumping liquid through the microfluidic device and then out to a reservoir that is in contact with a supply of oxygen. This method would, however, dilute any metabolites given off by the living system that is under investigation within the device, and since the biggest limitation of NMR is sensitivity, it is pertinent to avoid this.

Many solutions to the challenge of pumping and mixing at small scales exist, these include 3D printed valves [262, 263], syringe pumps [264–266], pressure actuated valves [267–269], electrowetting (sometime referred to as digital microfluidics) [270, 271], piezoelectric pumps [272, 273], magnetic pumping [274, 275], and centrifugal forces [276–

[278]. However, in order to enable microfluidic pumping and mixing at high magnetic fields, and high-resolution NMR, a number of challenges must be overcome. Firstly, the dead volume of the device should be kept to a minimum, as any unnecessary dilution will affect the ability to collect NMR spectra. Secondly, the materials used should be compatible with a high magnetic field, clearly ruling out ferrous metals, this also rules out materials that have a significantly different magnetic susceptibility to that of the chosen fluid (in this case water). As described in chapter 3, susceptibility mismatches need to be carefully managed, or they will interfere with the homogeneity of the magnetic field which is essential for production high resolution spectra. Thirdly, the construction materials selected must be conducive to rapid prototyping, and as such, must be cheap and readily available, as well as be easily cut by a laser cutter and bonded using a simple method. Fourthly, when fully assembled the device must fit inside the bore of an NMR magnet, typically 38mm in diameter. The NMR sensitive area, should not be more than 1 mm in thickness, due to limitations imposed by the strip-line probe geometry [1]. Lastly, the device should be able to seal against gas and liquid pressures whilst in operation inside the magnet.

In summary, the device must meet the following criteria:

- Non-magnetic parts where possible, susceptibility matched.
- Easily fabricated using rapid prototyping.
- Low dead volume pump.
- Biocompatible materials.
- Geometry compatible with transmission line probe.
- Easily assembled and operated *in situ*.

Pumps that integrate pumping ‘on chip’ are key to minimising the dead volume within the device. Unger and co-workers [279], were amongst the first to do this by micro-fabricating PDMS valves using soft lithography. Fig. 5.1 shows the devices, these work by having a central fluid path that has various gas channels running perpendicular above it. By simply applying air pressure, the gas channel expands cutting off the flow in the fluid path beneath. When these valves are actuated in sequence, they produce a net movement of fluid and flow rates of 2.5 nL/s were achieved.

Leslie et al [280] had slightly different approach. In the ‘pump’ the PDMS forms a dome above a circular structure in the fluid channel that is depressed using air pressure. In order to control the flow they use so called fluidic diodes, these work analogously with electric diodes, by only allowing fluid flow above a certain pressure in one direction only. These diodes are formed by having a weir that separates two fluid channels covered by a compliant PDMS membrane. When the internal fluid pressure

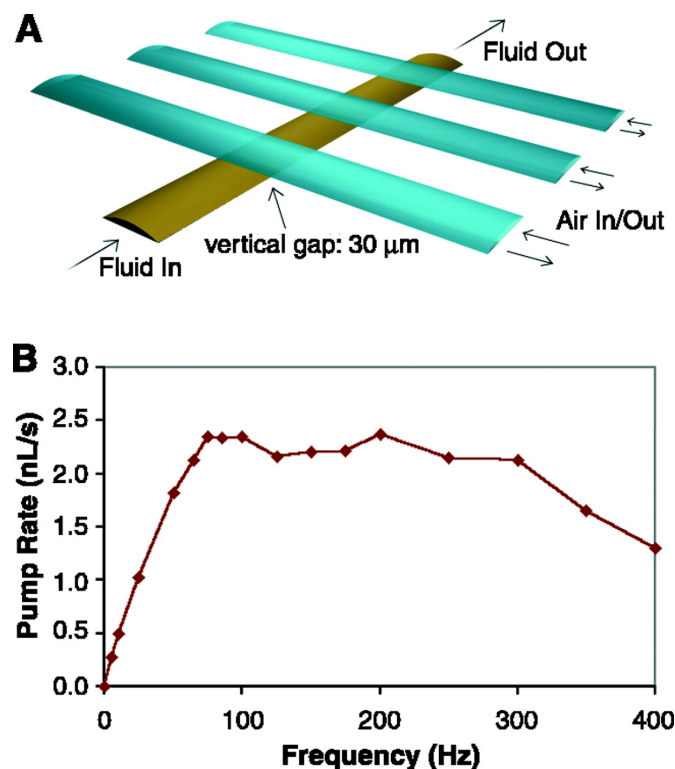
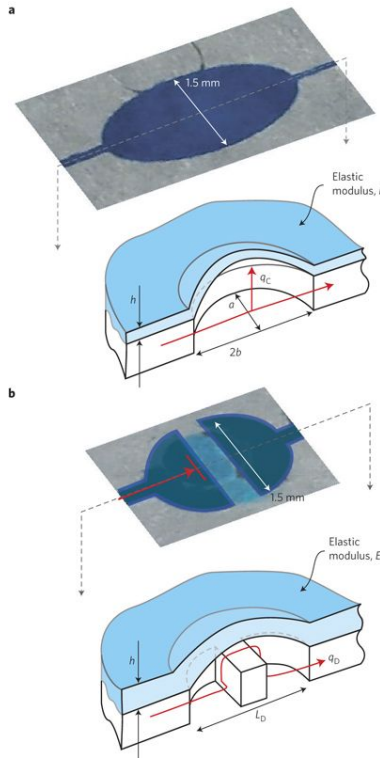


FIGURE 5.1: A) A 3D scale diagram of an elastomeric peristaltic pump. The channels are 100 m wide and 10 m high. Peristalsis was typically actuated by the pattern 101, 100, 110, 010, 011, 001, where 0 and 1 indicate “valve open” and “valve closed,” respectively. B) Pumping rate of a peristaltic micropump versus various driving frequencies.

This figure is reproduced from [279].

reaches the threshold, this pushes the PDMS membrane up and allows fluid connection over the weir. The pressure required to open the diode depends on the thickness of the PDMS ceiling and is predictable which allowed control of flow in the chip at large.

The solution employed here involves a multilayered poly(methylmethacrylate) PMMA device, with two PDMS membranes, sandwiched between two 3D printed holders held together with brass screws. The PMMA device houses the structures for the valves, as well as the fluid circuits, including an NMR sensitive sample chamber and on-chip reservoir. The PDMS layers have two separate functions, the top membrane forms the valves with the PMMA structures whilst the bottom membrane acts as an o-ring to seal against fluid leaks. The 3D printed holders are also multi purpose. The top holder forms the last part of the valves by sealing the PDMS-PMMA valve and allowing the delivery of pneumatic pressure through the bore of the magnet to the device. The bottom 3D printed holder allows the device to be filled and supplies external ports for fluid short circuiting. Together, they help seal the device against gas and liquid leaks. This device coupled with a bespoke, homebuilt probe enables pumping and observation by NMR in a microfluidic device.



**FIGURE 5.2:** **a**, Discrete fluidic capacitors are created by bonding deformable films (in this case, PDMS) over reservoirs placed in the network between fluidic channels (resistors) fabricated in glass. These features store and release fluid (volumetric flow rate,  $q_C$ ) in proportion to the time rate of change in pressure inside the network; the proportionality constant (capacitance,  $C$ ) depends on film thickness ( $h$ ), span (a, b) and elastic modulus ( $E$ ). **b**, Discrete fluidic diodes are created by bonding deformable films around weirs that separate two channels in the network. When the internal pressure is larger than the external pressure, the diode opens and exhibits nonlinear pressure–flow relationships (volumetric flow rate,  $q_D$ ) dictated by solid–fluid coupling. When the internal pressure is less than the external pressure, the diode pulls shut and prevents flow. Figure taken from [280].

For this work, the valves that are used for pumping are integrated in to the fluid path on the device itself. These valves are then actuated in sequence to produce a net flow of liquid around the device. Shown below in Fig. 5.3 is the basic principle behind the design.

In the device, there are valves cut into the layers of PMMA. These are formed by a hole in the top, and middle layer. The hole in top layer has a radius of  $500\mu\text{m}$  whilst the hole in the middle layer has a radius of  $100\mu\text{m}$ . The top layer has a channel (approx.  $150\mu\text{m}$  in width and depth) scored into it to deliver fluid to the top chamber whilst the middle layer has a similar channel scored on the under-side to carry fluid away. When covering the hard PMMA structure with the more compliant PDMS membrane of  $250\mu\text{m}$  thickness, applying air pressure from above seals the valve by covering the hole in the middle layer. A 3D rendering of a single valve is shown in Fig. 5.4 and shows the ratio of pump holder opening, top hole; and middle hole respectively. The key to

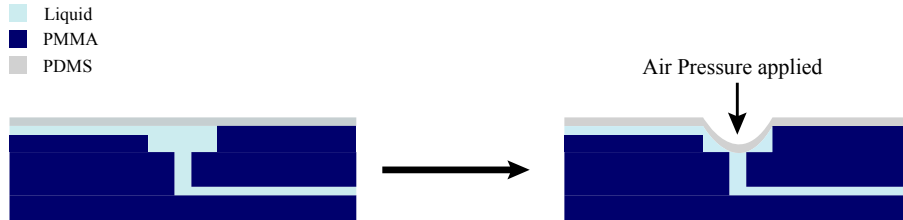


FIGURE 5.3: A cut-through view of the valves in the device showing how when air pressure is applied the PDMS membrane is pushed down and seals the small hole cut in the middle layer.

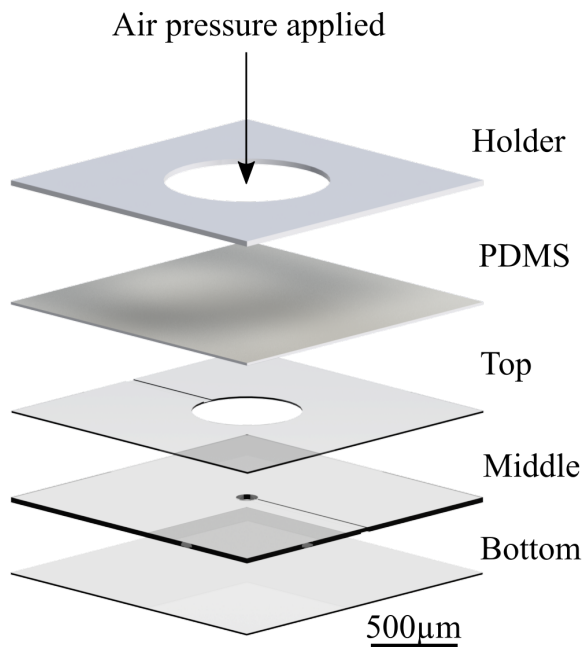


FIGURE 5.4: 3D render of a single valve with 3D printed layer shown too

these valves is that the scored channels are on opposing sides of the valve. In Fig. 5.5, micrographs of the chip outside the holders are shown, with the valves where one can see the fluid channels on opposing side of their respective layers. Also given, is side by side comparison of the same valve (valve 2 in Fig. 5.7) open (2) and closed (3) one can see the 'ring' formed by the PDMS as it seals against the middle layer.

PMMA was chosen for the main construction material as it is amenable to rapid prototyping, and can be reliably bonded using established methods [281]. The susceptibility of PMMA is similar to water, so high resolution spectroscopy is possible. It is biocompatible and optically transparent, which allows for future biological experiments that may also require fluorescent analysis. Poly(dimethylsiloxane) (PDMS) is used as

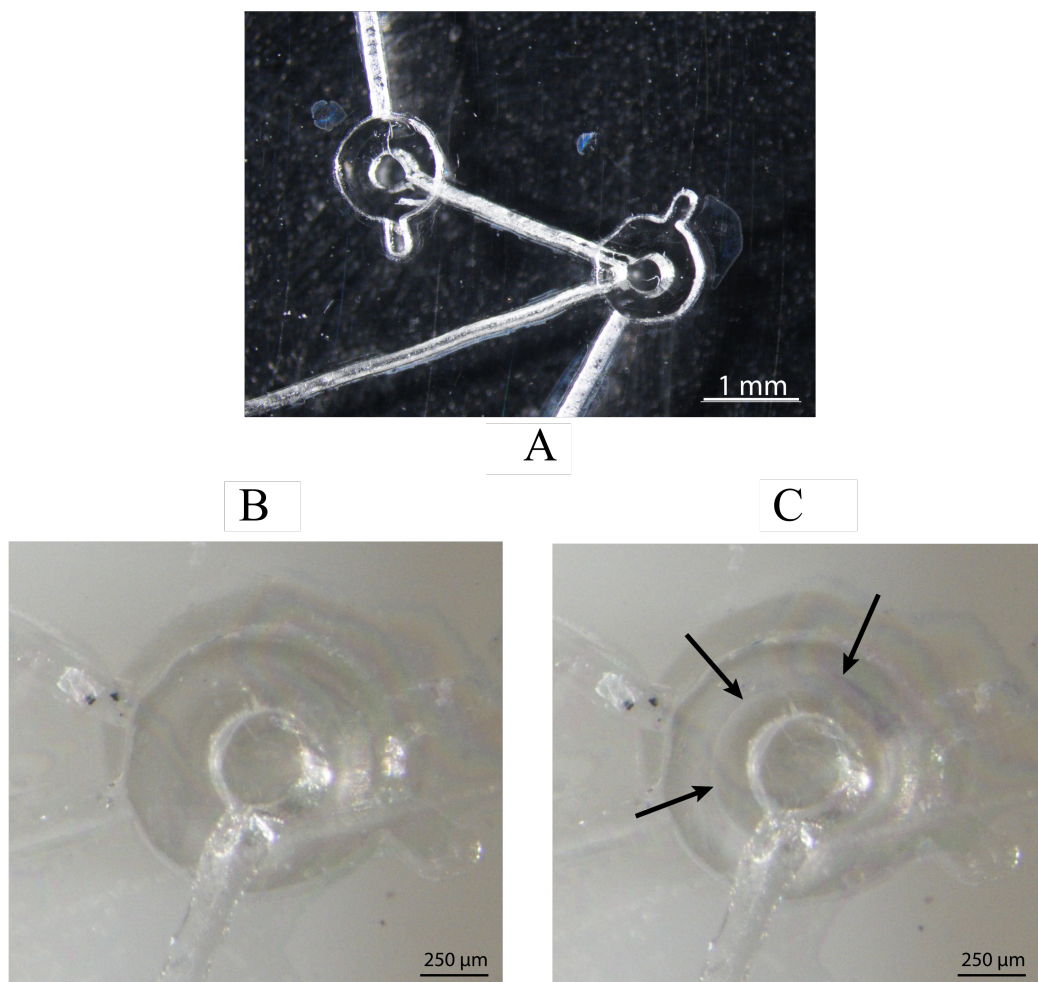


FIGURE 5.5: Micrographs of A: free chip showing two valves B: An assembled device with an open valve C: An assembled device with a closed valve, the arrows indicate the area where the PDMS is in contact with the PMMA and is sealing the hole.

the membrane in the valves due to its wide availability and bio-compatibility. However, when considering PDMS devices in NMR it is important to place it away from any NMR sensitive areas. Due to its amorphous structure, the  $^1\text{H}$  background signal from PDMS is large and broad across the range of ppm that the signals that are of interest appear. This broad background signal, makes it impractical to suppress and any suppression would also suppress the signals of interest, and could lead to difficulties in quantification of substances present in the sample under investigation.

In the design shown in Fig. 5.6, a PDMS layer is still used. However, it is removed from the sensitive area around the sample chamber so that it does not interfere with the signal collected from the device. The 3D printed part's role here is three-fold, firstly, it acts as a conduit for delivering liquids and transporting them around the device. Secondly, it allows for the pressurised air to be delivered which drives the pneumatic

valves and enables pumping. Lastly, when screwed together, the 3D printed parts form a seal against liquid and gas leaks.

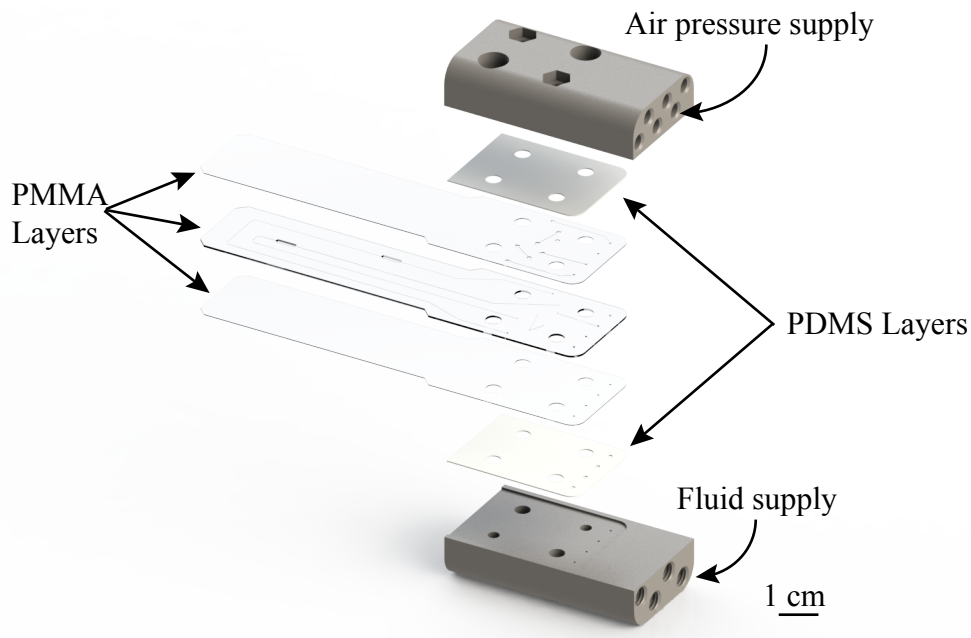


FIGURE 5.6: A 3D representation of the device with separate layers of chips and PDMS layers shown.

The fluidic path design is shown in Fig. 5.7. There are six valves that make up the pumping network, these are labelled **1-6**. Using the valves, it is possible to selectively pump around the inner circuit, shown in red, or the entire circuit formed of the blue and red liquid paths. To pump around the inner circuit, valves **3** and **5** are closed, and valves **2**, **4**, and **6** are actuated in sequence. To pump around the full circuit the ports (**A-D**) need to be linked by external tubing, the easiest way to do this is to join **A** to **B** and **C** to **D**. Valve **4** is closed, and valves **1**, **2**, and **3** actuated in sequence. The outer circuit also features an on-chip reservoir that is of the same size and shape of the sample chamber, this reservoir is used to balance the volumes of the two circuits, and provides a source of whichever reactant or chemical is to be introduced to the sample chamber.

The 6 valves are all individually addressable with air pressure which, when coupled with home-written Arduino firmware, can be actuated in sequence in order to move fluid in a given direction. The block diagram of the arduino set-up is shown in Fig. 5.8. By varying the frequency and lambda parameters, listed in the firmware, one can control the liquid pumped in a given time.

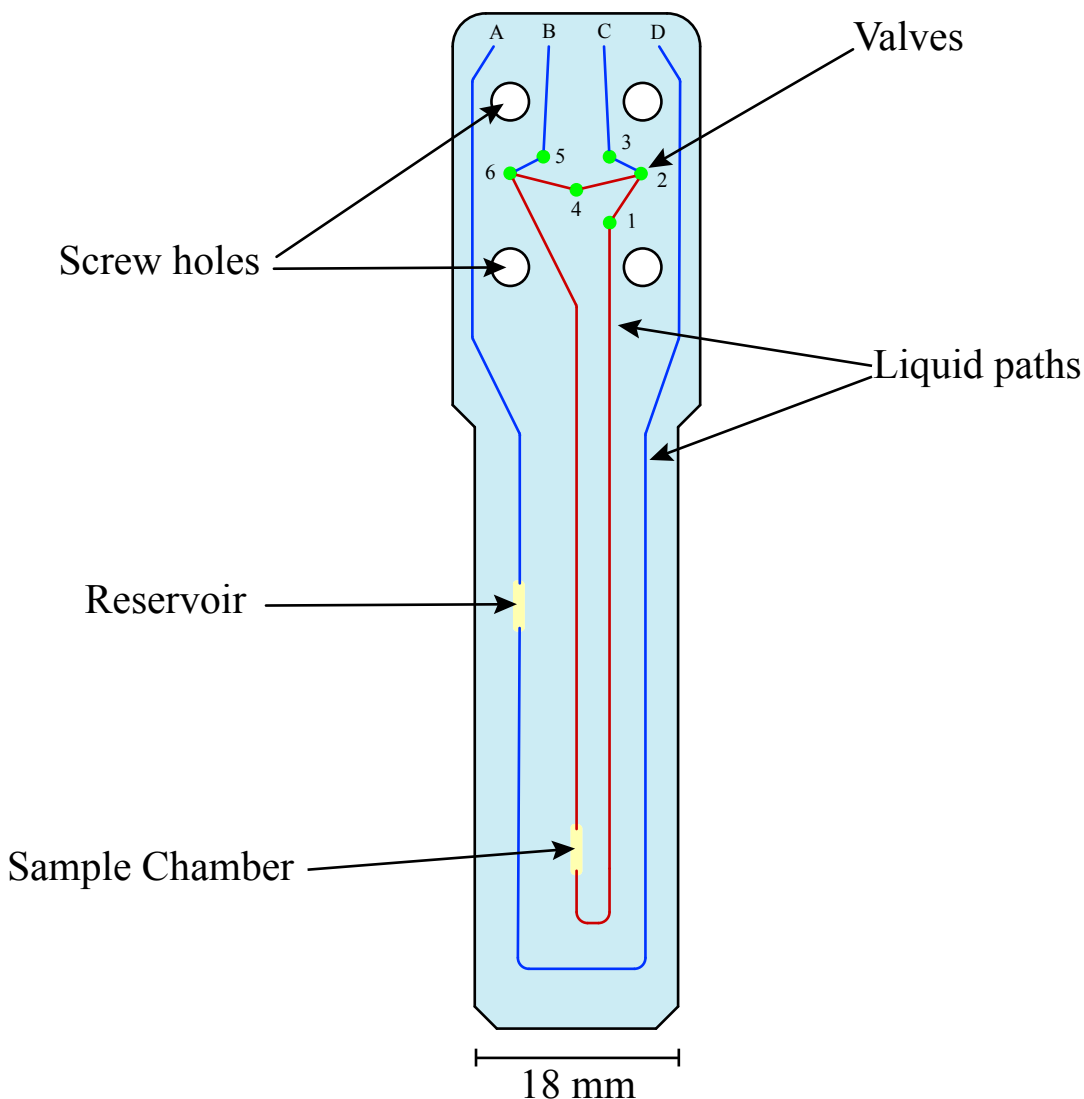


FIGURE 5.7: A CAD drawing of the chip designed for pumping and mixing. Inner (red) and outer (blue) liquid circuits; liquid ports (**A-D**) and valve positions (1-6) shown.

### 5.1.1 Materials and Methods

The devices are composed of three layers of cell cast poly(methyl methacrylate) (PMMA, Weatherall Equipment). The sheet thickness was 200  $\mu\text{m}$  for the top and bottom layers, and 500  $\mu\text{m}$  for the middle layer. The channels and sample chambers were designed in AutoCAD and cut using a CO<sub>2</sub> laser (HPC Laser Ltd.) to an approximate width and depth of 150  $\mu\text{m}$ . These layers were bonded together using plasticiser (2.5% v/v dibutyl phthalate in isopropyl alcohol) and subjected to heat and pressure (358 K, 18.6 MPa). To seal the devices, two poly(dimethylsiloxane) (PDMS, Shielding Solutions) were designed in AutoCAD and cut using the same laser as the PMMA layers.

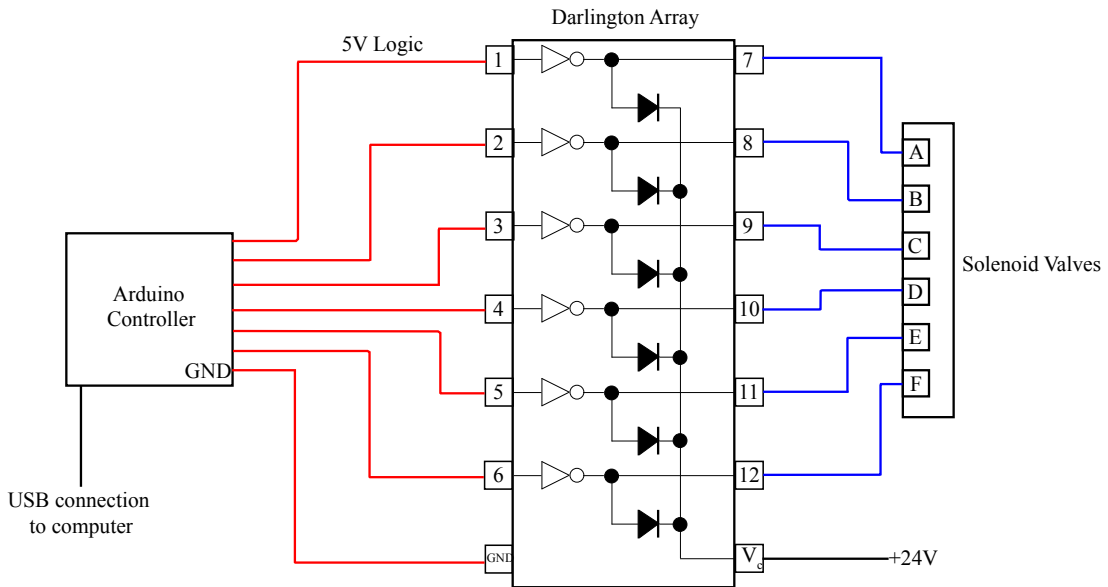


FIGURE 5.8: An arduino controller is connected to, and powered by, a laptop via USB. The controller is connected to a darlington array via six 5V logic connections (shown in red) when addressed, these allow the corresponding pin opposite to draw power from the +24V connected from an outside source. The blue lines indicate the the wires carrying 24V to the solenoid bank which are pneumatically connected to the valves in the chip as labelled.

The PMMA and PDMS were screwed together and held in place using 3D printed devices designed in SolidWorks (Acura Xtreme, ProtoLabs). These, as shown in Fig. 5.6, seal the device whilst enabling the filling of the device as well as delivering the pressurised air for the peristaltic pumping.

The hardware for controlling pumping comprised of a solenoid valve system with 8 individual valves (Festo, RS Components Ltd). These were connected to 3mm plastic tubes (Festo, RS Components Ltd) and all supplied from an in-lab air pressure source. This valve system was connected, via a solderless breadboard, to an arduino (Mega 2560, RS Components Ltd) controller allowing for individual control of each of the valves. The Solenoid valve system was powered using a 24V supply.

The device was put into a transmission line based home-built probe. In this, the device is held between two striplines with the inner sample chamber lining up with the constriction on the strip-lines. NMR measurements were performed on a bruker AVANCE III spectrometer and 11.7 T magnet. Spectra were collected using 64 scans using a 90 degree pulse length of 2.5 us at 50 W of power. Water suppression was achieved by using presaturation with  $5 \times 10^{-4}$  W.

100mM solutions of sodium acetate (Merck) and 3-(Trimethylsilyl)-1-propanesulfonic acid (DSS, Merck) by dissolving 82 mg and 196 mg in 10 ml of deionised water (ReAgent)

respectively. The two fluidic loops were then filled with these separately and the in/out ports short circuited.

Firmware for controlling the peristaltic pump was written in Arduino and is provided in the appendix. This has the ability to put the pump into 3 states “advance”, “mixing” and “quiet”. The “advance” state pumps from the outside loop of the device to the inside loop for a desired number of seconds; “mix” pumps around the inner loop for a desired number of seconds; and “quiet” stops all pumping and leaves all valves open indefinitely.

## 5.2 Results and Discussion

### 5.2.1 Characterisation of flow

Characterisation of flow experiments were performed with the device in an “open” configuration. This means that after the device was screwed together the two circuits shown in blue and red were joined together by fixing tubing between the **A** and **B** ports shown in Fig. 5.7. This leaves **C** as the “in” port and **D** to be the “out” port with valves 3, 2, and 1 being actuated in sequence to pump, and valve 4 sealed.

The device was connected to translucent polytetrafluoroethylene (PTFE) tubing (Outer diameter 1.6 mm, inner diameter 0.8 mm) with one end submerged in a 500 mL beaker containing filtered DI water (Reagent). Next to the device a ruler was secured to the bench top with the tubing fixed parallel to it. The pump was then switched on and the device allowed to draw water, and pump out the other side. When the water meniscus reached the tubing next to the ruler a timer was started and the distance along the ruler was recorded every minute for 10 minutes. This was repeated 3 times for frequencies from 0.25-1 keeping the lambda constant at 3, which had shown through trial and error to be the optimum number.

The graph shown in Fig. 5.9 is the result of plotting the cumulative volume pumped vs. time. All 4 frequencies show very little deviation from linearity in the long term and also show very small error bars (plotted as  $\pm 2\sigma$ ).

In Fig. 5.10, the flow rate of the pump at varying frequencies is plotted. This shows that the flow rate doesn’t linearly depend on frequency, and seems to level off at higher frequencies. When initially observing the gradient of the lines in Fig. 5.9, the non-linearity was attributed to inconsistencies in the tightening of the screws in the device. However, the small error bars associated with the flow rates across three separate experiments, each with at least one disassembly and reassembly of the device, it is now thought that the limit of the pump rate is related to the elasticity of the membrane, and how fast it’s able to ‘snap back’ and re prime itself to pump in each valve.

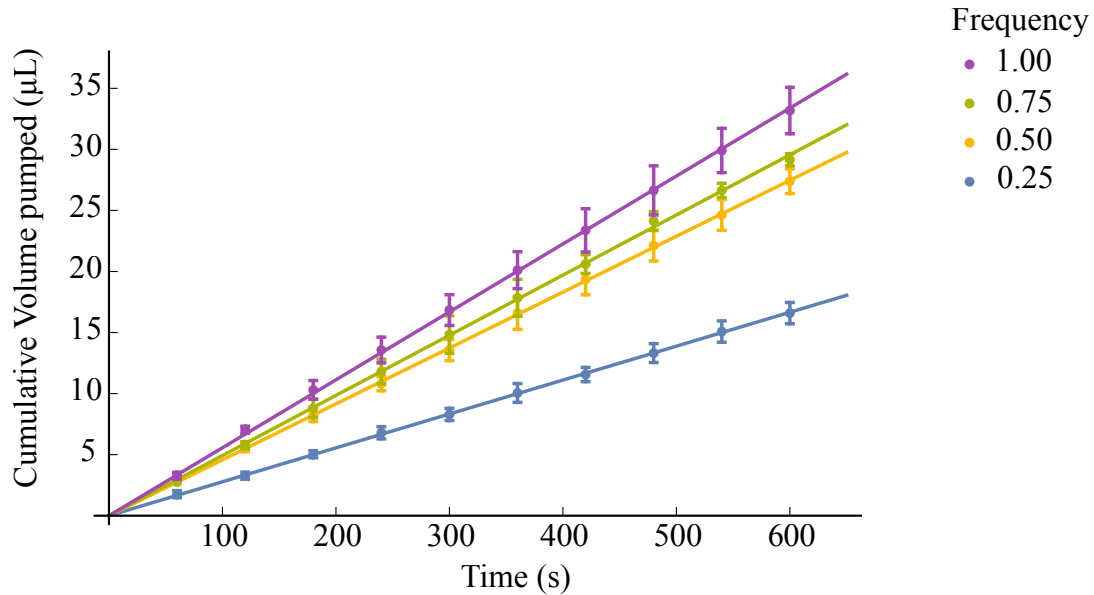


FIGURE 5.9: Plot of the total volume pumped vs time for a chip in the open configuration.

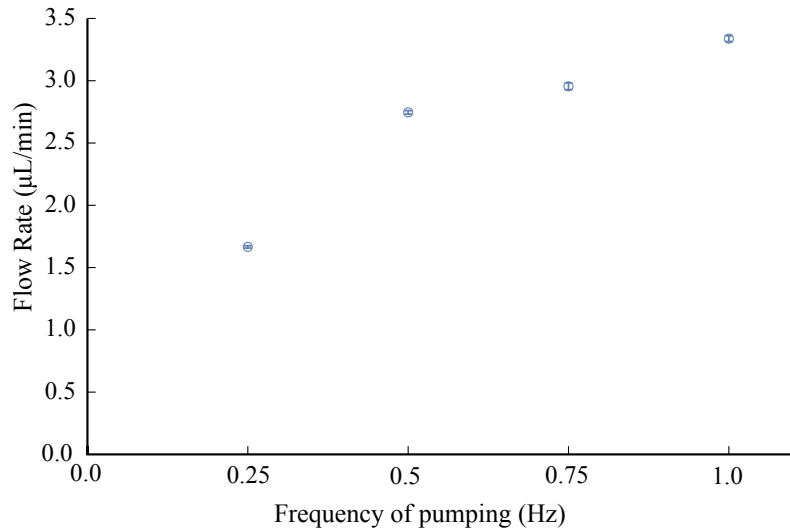


FIGURE 5.10: Flow rates produced by the pump at different frequencies.

### 5.2.2 *In situ* operation of the device

In order to validate the pumps compatibility with NMR, the device was placed into a home built transmission line probe inside a 500 MHz magnet. The arduino controller and solenoid valve bank were secured outside the magnet and the 6 pressurised air lines fed in through the top of the magnet. The device was then filled with 100mM sodium acetate in DI water (Sigma Aldrich) in the inner circuit by attaching a syringe to inlet

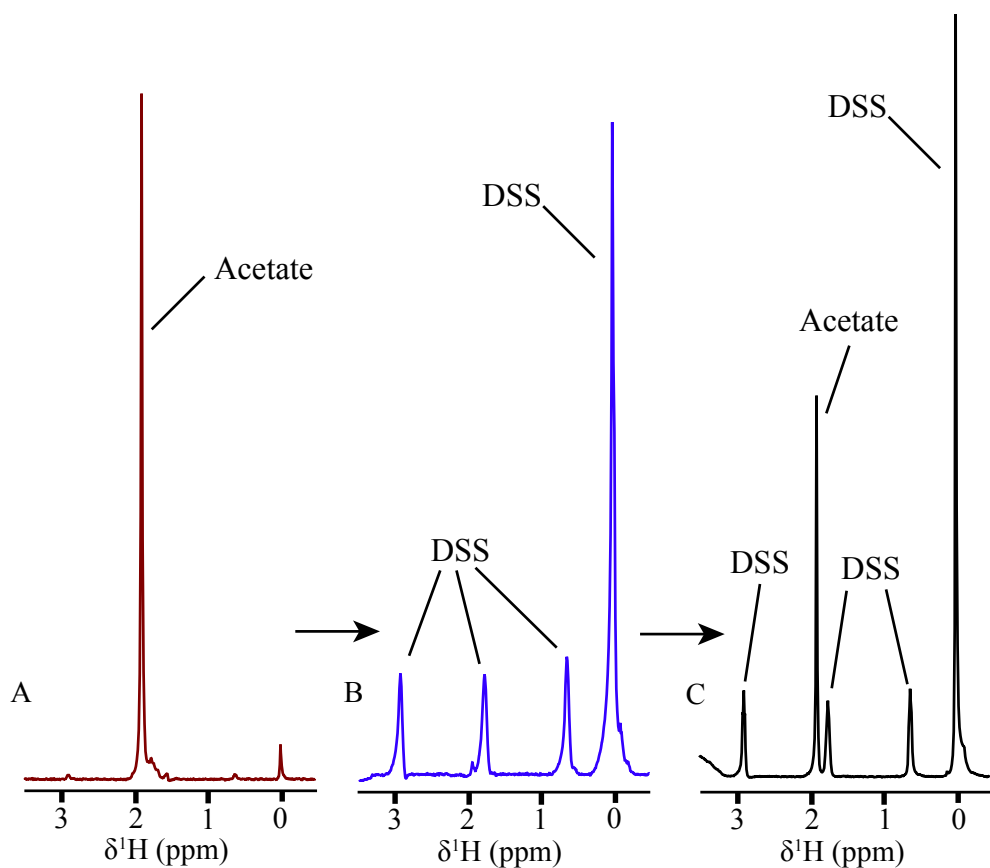


FIGURE 5.11: NMR spectra recorded with 16 transients on a device containing 100mM Sodium acetate in the inner circuit and 100mM DSS in the outer circuit.

**B** in Fig. 5.7. 100mM DSS in DI water (Sigma Aldrich) was added to the outer circuit by syringing into inlet **A**. The sample chamber then contained only sodium acetate and all the initial signal should arise from this. The two fluid networks were then connected using two short lengths of 1/16" outer diameter PTFE tubing by joining **A** to **B** and **C** to **D**.

First, a spectra was collected of the chip after filling, **A** in Fig. 5.11, using 16 transients and shows mainly the acetate signal at 1.9 ppm. The pump was then put into the 'advance' state for 120 seconds which mean the valves are actuated in order to pump liquid around both circuits. The pump then mixed in the inner circuit for 120 seconds and a second spectra was recorded, **B**. This shows the 4 signals typical of DSS at 2.91 ppm, 1.75 ppm, 0.63 ppm and 0 ppm and very little acetate signal. Indicating that the volume inside the NMR sensitive area has been almost entirely exchanged. Lastly the pump again advanced and mixed for the same time as before producing the spectra shown in **C**. Again, this spectrum is different. It shows all signals expected in abundance. This points to mixing of the two substances facilitated by the peristaltic pump and serves as proof, at least in principle, that an NMR compatible microfluidic

peristaltic pump capable of mixing liquids in a controllable manor has been presented here.

### 5.3 Conclusions

In conclusion, an NMR compatible; low dead volume microfluidic pump has been designed and manufactured that works inside the bore of a high field magnet. The pump has shown excellent linearity and stability in the long term as well as performing exchange, and mixing, of two substances within the device inside a high field magnet. The present limitations are that precise volume control has not yet been achieved. This is, however, thought to be linked with the varied tightening of the screws of the 3D holder as well as the presence of bubbles within the device. Another element that requires further probing is the non-linear dependence of flow rate on frequency. My intuition is that this depends on the thickness of the PDMS layer used however further experimentation with varying thicknesses is needed. Potential future applications of this pump include: microfluidic protein binding experiments; *in situ* liver slice culture and metabolomics; and hyperpolarization experiments.

# Chapter 6

## Conclusions

In this thesis efforts to combine microfluidics with micro-NMR are described.

Enabling microfluidic experiments to be compatible with NMR offers advantages of label-free, non-destructive and non-invasive analysis which can easily be combined with existing methods of investigation and used to enhance the information that can be gleaned from a system.

In chapter 3 a device capable of generating microfluidic droplets and performing high-resolution NMR is presented. The key to doing this is matching the susceptibilities of the fluids and materials used. This is done by cutting shim structures filled with air around the sample chamber and by doping the aqueous phase with chelated Eu<sup>3+</sup> ions to bring them inline with the susceptibility of the oil phase, in this case cyclohexane. The precise location and size of the shim structures was simulated and the exact concentration of europium measured in order to collect a high resolution spectrum of droplets containing glucose, comparable to the spectrum obtained by pure phase glucose and could pave the way for droplet NMR to be used in future.

An NMR experiment scaled down to micro-NMR is described in chapter 4, where parahydrogen induced polarisation (PHIP) reactions were performed on a device capable of bubble free hydrogenation. The PASADENA reaction presented in the chapter leads to enhancement factors of 1800 when compared with using normal hydrogen. The microfluidic aspect of the device allows the production of the hyperpolarised species in continuous flow, this stability allows for the collection of 2D hyperpolarised spectra. This device could provide a way to produce hyperpolarised metabolites continuously and either introduce them to cell culture or other living tissue *in situ* or for injection and *in vitro* imaging.

Finally, chapter 5 describes the design and manufacture of a peristaltic pump device capable of exchange and mixing of fluids within the device in a high field NMR magnet. The design couples together a PDMS membrane and structures cut into the

device to form valves which are individually addressable to perform the pumping and mixing routines, whilst keeping dead volume to a minimum. Operation of this device *in situ* is presented, with spectra shown, demonstrating the exchange and mixing of two fluids in the device.

These three examples of the successful combination microfluidics with high-field high resolution micro-NMR spectroscopy, show how the two fields can be used to enhance and compliment one another without compromise. The novelty and function of either part, microfluidic or NMR, are not sacrificed for the other. They make for exciting prospects, the droplets could be used to investigate and track oxygen concentrations in living tissue culture, the continuous PHIP device could provide new insights into the kinetics of the PASADENA reaction reported, as well as the formation of metabolites directly that could be introduced to a cell culture and the metabolomics tracked using NMR. The pump can be combined with microfluidic experiments that are mass limited for example, ligand binding studies of proteins or could be used in cell culture experiments to perfuse the culture with media and provide oxygen and nutrients whilst enabling the observation of the culture by NMR.

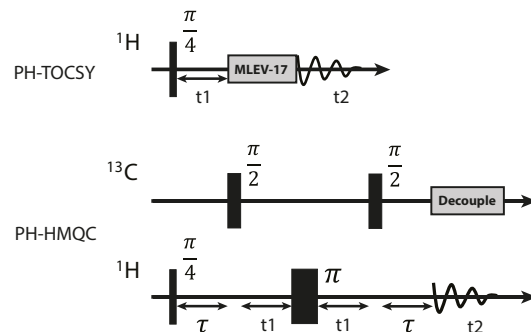
Overall, microfluidic NMR shows promise in challenging new problems and offers exciting possibilities when combined with existing techniques.

# Appendix A

## Appendix

### A.1 2D Pulse sequences for PH-TOCSY and PH-HMQC

The pulse sequences used for the PH-TOCSY and the PH-HMQC spectra are shown below.



### A.2 Arduino Firmware

Below the firmware for the operation of the peristaltic pump is given.

```
pump_driver_0.0.1

#define VALVE_A 3
#define VALVE_B 11
#define VALVE_C 2
#define VALVE_D 4
#define VALVE_E 5
#define VALVE_F 6
#define N_VALVES 6

int ValvePins[] = {VALVE_A, VALVE_B, VALVE_C, VALVE_D, VALVE_E, VALVE_F};
```

```
int AdvancePump[] = {VALVE_A, VALVE_B, VALVE_C};
int AdvanceValves[] = {LOW, LOW, LOW, HIGH, LOW, LOW};

int MixPump[] = {VALVE_F, VALVE_D, VALVE_B};
int MixValves[] = {HIGH, LOW, LOW, LOW, HIGH, LOW};

long bedTime = 0;

enum state {QUIET, MIX, ADVANCE};

String stateDesc[] = {"idling.", "mixing", "pumping"} ;

state currentState;
state lastState;

const int MaxParams = 5;
String command;
String params[MaxParams];
int nparam=0;

float freq = -1.0;
float lambda = 3.0;

void setup() {

    for(int k=0;k<N_VALVES;k++)
    {
        pinMode(ValvePins[k], OUTPUT);
        digitalWrite(ValvePins[k], LOW);
    }

    Serial.begin(115200);
    while(!Serial);
    Serial.println("Hello.");
}

void loop() {
    if( checkForCmd() ) processCmd() ;
    if( millis() > bedTime ) gotoState(QUIET);

    switch (currentState) {
        case MIX :
            startPump(MixPump,3,freq,lambda) ;
            break ;

        case ADVANCE :
            startPump(AdvancePump,3,freq,lambda) ;
            break;

        default:
            break;
    }

    delay(10);
}
```

```
void gotoState(state newState)
{
    if(currentState != newState) {
        lastState = currentState;
        currentState = newState;

        Serial.print(stateDesc[newState]);

        switch(newState) {
            case MIX:
                for(int k=0;k<N_VALVES;k++) digitalWrite(ValvePins[k],MixValves[k]);
                Serial.print(" for ");
                Serial.print((bedTime-millis())/1000.0);
                Serial.println(" seconds.");
                break;

            case ADVANCE:
                for(int k=0;k<N_VALVES;k++) digitalWrite(ValvePins[k],AdvanceValves[k]);
                Serial.print(" for ");
                Serial.print((bedTime-millis())/1000.0);
                Serial.println(" seconds.");
                break;

            case QUIET:
                for(int k=0;k<N_VALVES;k++) digitalWrite(ValvePins[k],LOW);
                Serial.println();
                break;
        }
    }

    bool checkForCmd()
    {
        if(!Serial.available()) return(false);

        command = Serial.readStringUntil('\n');
        command.trim();
        int k;
        do {
            k=command.indexOf(' ');
            params[nparam++] = command.substring(0,k);
            command=command.substring(k);
            command.trim();
        } while(k>0 && nparam < MaxParams) ;

        /* Serial.println("command read."); */

        return(true);
    }

    void processCmd()
    {

        command="";

        /* for(int k=0;k<nparam;k++) {
            Serial.println(params[k]);
        }*/
    }
}
```

```
    } */

    if(npParam>0) {

        if(params[0]==="mix") {
            bedTime = millis() + params[1].toFloat()*1000;
            gotoState(MIX);
        }

        else if (params[0]==="adv") {
            bedTime = millis() + params[1].toFloat()*1000;
            gotoState(ADVANCE);
        }

        else if(params[0]==="stop") {
            gotoState(QUIET);
            bedTime = millis();
        }

    }

    npParam=0;
}

void startPump(int *valves, int npins, float freq, float lambda)
{
    float psi;
    for(int k=0;k<npins;k++) {
        psi=cos( 2*PI*(k/lambda-freq*millis()/1000.) );
        if(psi>0)
            digitalWrite(valves[k],HIGH) ;
        else
            digitalWrite(valves[k],LOW);
    }
}

void stopPump(int *valves, int npins)
{
    for(int k=0;k<npins;k++)
        digitalWrite(valves[k],LOW);
}
```

---

# Bibliography

- [1] M. Sharma and M. Utz, *Journal of Magnetic Resonance*, 2019, **303**, 75–81.
- [2] G. Finch, A. Yilmaz and M. Utz, *Journal of Magnetic Resonance*, 2016, **262**, 73–80.
- [3] H. Fang, Y. Sun, X. Wang, M. Sharma, Z. Chen, X. Cao, M. Utz and Z. Tian, *Science China Chemistry*, 2018, **61**, 1460–1464.
- [4] S. Terry, J. Jerman and J. Angell, *IEEE Transactions Electron Devices*, 1979, **26**, 1880.
- [5] D. R. Reyes, D. Iossifidis, P.-A. Auroux and A. Manz, *Analytical Chemistry*, 2002, **74**, 2623–2636.
- [6] H. Van Lintel, F. Van de Pol and S. Bouwstra, *Sensors and Actuators*, 1988, **15**, 153–167.
- [7] F. Van De Pol, D. Wonnink, M. Elwenspoek and J. Fluitman, *Sensors and Actuators*, 1989, **17**, 139–143.
- [8] S. Shoji, M. Esashi and T. Matsuo, *Sensors and Actuators*, 1988, **14**, 101–107.
- [9] A. Manz, Y. Miyahara, J. Miura, Y. Watanabe, H. Miyagi and K. Sato, *Sensors and Actuators B: Chemical*, 1990, **1**, 249–255.
- [10] A. Manz, N. Gruber and H. Widmer, *Sensors and Actuators B: Chemical*, 1990, **1**, 244–248.
- [11] A. Manz, D. Harrison, J. Fettinger, E. Verpoorte, H. Ludi and H. Widmer, TRANSDUCERS'91: 1991 International Conference on Solid-State Sensors and Actuators. Digest of Technical Papers, 1991, pp. 939–941.
- [12] D. J. Harrison, A. Manz, Z. Fan, H. Luedi and H. M. Widmer, *Analytical Chemistry*, 1992, **64**, 1926–1932.
- [13] K. Seiler, D. J. Harrison and A. Manz, *Analytical Chemistry*, 1993, **65**, 1481–1488.
- [14] A. T. Woolley, D. Hadley, P. Landre, A. J. deMello, R. A. Mathies and M. A. Northrup, *Analytical Chemistry*, 1996, **68**, 4081–4086.

- [15] L. Bousse, R. McReynolds, G. Kirk, T. Dawes, P. Lam, W. Bemiss and J. Parce, *Sensors and Actuators B: Chemical*, 1994, **20**, 145–150.
- [16] G. M. Whitesides, *Nature*, 2006, **442**, 368–73.
- [17] J. M. Ng, I. Gitlin, A. D. Stroock and G. M. Whitesides, *Electrophoresis*, 2002, **23**, 3461–3473.
- [18] G. M. Whitesides and A. D. Stroock, *Physics Today*, 2001, **54**, 42–48.
- [19] J. C. McDonald, D. C. Duffy, J. R. Anderson, D. T. Chiu, H. Wu, O. J. Schueller and G. M. Whitesides, *ELECTROPHORESIS: An International Journal*, 2000, **21**, 27–40.
- [20] D. B. Weibel, M. Kruithof, S. Potenta, S. K. Sia, A. Lee and G. M. Whitesides, *Analytical Chemistry*, 2005, **77**, 4726–4733.
- [21] A. Günther, M. Jhunjhunwala, M. Thalmann, M. A. Schmidt and K. F. Jensen, *Langmuir*, 2005, **21**, 1547–1555.
- [22] D. J. Laser and J. G. Santiago, *Journal of micromechanics and microengineering*, 2004, **14**, R35.
- [23] C. L. Hansen, E. Skordalakes, J. M. Berger and S. R. Quake, *Proceedings of the National Academy of Sciences*, 2002, **99**, 16531–16536.
- [24] R. Ramsey and J. Ramsey, *Analytical Chemistry*, 1997, **69**, 1174–1178.
- [25] A. R. Wheeler, W. R. Throndset, R. J. Whelan, A. M. Leach, R. N. Zare, Y. H. Liao, K. Farrell, I. D. Manger and A. Daridon, *Analytical Chemistry*, 2003, **75**, 3581–3586.
- [26] C.-C. Lee, G. Sui, A. Elizarov, C. J. Shu, Y.-S. Shin, A. N. Dooley, J. Huang, A. Daridon, P. Wyatt, D. Stout *et al.*, *Science*, 2005, **310**, 1793–1796.
- [27] T. Thorsen, R. W. Roberts, F. H. Arnold and S. R. Quake, *Physical review letters*, 2001, **86**, 4163.
- [28] D. Link, S. L. Anna, D. Weitz and H. Stone, *Physical review letters*, 2004, **92**, 054503.
- [29] Y.-C. Tan, J. S. Fisher, A. I. Lee, V. Cristini and A. P. Lee, *Lab on a Chip*, 2004, **4**, 292–298.
- [30] Z. Nie, S. Xu, M. Seo, P. C. Lewis and E. Kumacheva, *Journal of the American Chemical Society*, 2005, **127**, 8058–8063.
- [31] T. Nisisako and T. Torii, *Advanced materials*, 2007, **19**, 1489–1493.

- [32] A. Utada, E. Lorenceau, D. Link, P. Kaplan, H. Stone and D. Weitz, *Science*, 2005, **308**, 537–541.
- [33] A. Huebner, M. Srisa-Art, D. Holt, C. Abell, F. Hollfelder, J. Edel *et al.*, *Chemical communications*, 2007, 1218–1220.
- [34] T. Thorsen, R. W. Roberts, F. H. Arnold and S. R. Quake, *Physical review letters*, 2001, **86**, 4163.
- [35] F. K. Balagaddé, L. You, C. L. Hansen, F. H. Arnold and S. R. Quake, *Science*, 2005, **309**, 137–140.
- [36] P. J. Hung, P. J. Lee, P. Sabourchi, R. Lin and L. P. Lee, *Biotechnology and bioengineering*, 2005, **89**, 1–8.
- [37] S. Takayama, E. Ostuni, P. LeDuc, K. Naruse, D. E. Ingber and G. M. Whitesides, *Nature*, 2001, **411**, 1016.
- [38] J. Voldman, M. Gray, M. Toner and M. Schmidt, *Analytical Chemistry*, 2002, **74**, 3984–3990.
- [39] Z. Wang, J. El-Ali, M. Engelund, T. Gotsaed, I. Perch-Nielsen, K. B. Mogensen, D. Snakenborg, J. P. Kutter and A. Wolff, *Lab on a Chip*, 2004, **4**, 372–377.
- [40] D. Di Carlo, K.-H. Jeong and L. P. Lee, *Lab on a Chip*, 2003, **3**, 287–291.
- [41] S.-W. Lee and Y.-C. Tai, *Sensors and Actuators A: Physical*, 1999, **73**, 74–79.
- [42] H. Lu, S. Gaudet, M. A. Schmidt and K. F. Jensen, *Analytical Chemistry*, 2004, **76**, 5705–5712.
- [43] Y. Li, J. S. Buch, F. Rosenberger, D. L. DeVoe and C. S. Lee, *Analytical Chemistry*, 2004, **76**, 742–748.
- [44] K. Sato, M. Yamanaka, H. Takahashi, M. Tokeshi, H. Kimura and T. Kitamori, *Electrophoresis*, 2002, **23**, 734–739.
- [45] T. P. Burg and S. R. Manalis, *Applied Physics Letters*, 2003, **83**, 2698–2700.
- [46] J. El-Ali, P. K. Sorger and K. F. Jensen, *Nature*, 2006, **442**, 403.
- [47] A. Folch, A. Ayon, O. Hurtado, M. Schmidt and M. Toner, *Journal of biomechanical engineering*, 1999, **121**, 28–34.
- [48] A. Folch and M. Toner, *Annual review of biomedical engineering*, 2000, **2**, 227–256.
- [49] V. L. Tsang and S. N. Bhatia, *Advanced drug delivery reviews*, 2004, **56**, 1635–1647.
- [50] A. Sivaraman, J. Leach, S. Townsend, T. Iida, B. Hogan, D. B. Stoltz, R. Fry, L. Samson, S. Tannenbaum and L. Griffith, *Current drug metabolism*, 2005, **6**, 569–591.

- [51] M. J. Powers, K. Domansky, M. R. Kaazempur-Mofrad, A. Kalezi, A. Capitano, A. Upadhyaya, P. Kurzawski, K. E. Wack, D. B. Stolz, R. Kamm *et al.*, *Biotechnology and bioengineering*, 2002, **78**, 257–269.
- [52] C. Guguen-Guillouzo, B. Clément, G. Baffet, C. Beaumont, E. Morel-Chany, D. Glaise and A. Guillouzo, *Experimental cell research*, 1983, **143**, 47–54.
- [53] C. S. Chen, M. Mrksich, S. Huang, G. M. Whitesides and D. E. Ingber, *Science*, 1997, **276**, 1425–1428.
- [54] S. Bhatia, U. Balis, M. Yarmush and M. Toner, *The FASEB journal*, 1999, **13**, 1883–1900.
- [55] Y. Nakao, H. Kimura, Y. Sakai and T. Fujii, *Biomicrofluidics*, 2011, **5**, 022212.
- [56] D. Huh, B. D. Matthews, A. Mammoto, M. Montoya-Zavala, H. Y. Hsin and D. E. Ingber, *Science*, 2010, **328**, 1662–1668.
- [57] M. Esch, T. King and M. Shuler, *Annual review of biomedical engineering*, 2011, **13**, 55–72.
- [58] A. Skardal, T. Shupe and A. Atala, *Drug discovery today*, 2016, **21**, 1399–1411.
- [59] K.-J. Jang and K.-Y. Suh, *Lab on a Chip*, 2010, **10**, 36–42.
- [60] J. H. Sung and M. L. Shuler, *Lab on a Chip*, 2009, **9**, 1385–1394.
- [61] D. Huh, Y.-s. Torisawa, G. A. Hamilton, H. J. Kim and D. E. Ingber, *Lab on a Chip*, 2012, **12**, 2156–2164.
- [62] J. Wang, *Biosensors and Bioelectronics*, 2006, **21**, 1887–1892.
- [63] R. Raiteri, M. Grattarola, H.-J. Butt and P. Skládal, *Sensors and Actuators B: Chemical*, 2001, **79**, 115–126.
- [64] B. Kuswandi, J. Huskens, W. Verboom *et al.*, *Analytica chimica acta*, 2007, **601**, 141–155.
- [65] N. Pires, T. Dong, U. Hanke and N. Hoivik, *Sensors*, 2014, **14**, 15458–15479.
- [66] R. J. Flanagan, D. Perrett and R. Whelpton, *Electrochemical detection in HPLC: Analysis of drugs and poisons*, Royal Society of Chemistry, 2005, vol. 10.
- [67] P. S. Waggoner and H. G. Craighead, *Lab on a Chip*, 2007, **7**, 1238–1255.
- [68] M. Ferrari, *Nature reviews cancer*, 2005, **5**, 161.
- [69] H. Hou, X. Bai, C. Xing, N. Gu, B. Zhang and J. Tang, *Analytical Chemistry*, 2013, **85**, 2010–2014.

- [70] J. F. Rusling, C. V. Kumar, J. S. Gutkind and V. Patel, *Analyst*, 2010, **135**, 2496–2511.
- [71] A. M. Foudeh, T. F. Didar, T. Veres and M. Tabrizian, *Lab on a Chip*, 2012, **12**, 3249–3266.
- [72] S. Wang, X. Zhao, I. Khimji, R. Akbas, W. Qiu, D. Edwards, D. W. Cramer, B. Ye and U. Demirci, *Lab on a Chip*, 2011, **11**, 3411–3418.
- [73] J. R. Wojciechowski, L. C. Shriver-Lake, M. Y. Yamaguchi, E. Füreder, R. Pieler, M. Schamesberger, C. Winder, H. J. Prall, M. Sonnleitner and F. S. Ligler, *Analytical Chemistry*, 2009, **81**, 3455–3461.
- [74] N. Yildirim, F. Long, C. Gao, M. He, H.-C. Shi and A. Z. Gu, *Environmental science & technology*, 2012, **46**, 3288–3294.
- [75] A. M. Foudeh, J. T. Daoud, S. P. Faucher, T. Veres and M. Tabrizian, *Biosensors and Bioelectronics*, 2014, **52**, 129–135.
- [76] M. Swanson and B. Hammer, *Annual Reviews in Microbiology*, 2000, **54**, 567–613.
- [77] I. S. Kinstlinger and J. S. Miller, *Lab on a Chip*, 2016, **16**, 2025–2043.
- [78] P. C. Gach, K. Iwai, P. W. Kim, N. J. Hillson and A. K. Singh, *Lab on a Chip*, 2017, **17**, 3388–3400.
- [79] B. Bao, J. Riordon, F. Mostowfi and D. Sinton, *Lab on a Chip*, 2017, **17**, 2740–2759.
- [80] S. Giulitti, M. Pellegrini, I. Zorzan, P. Martini, O. Gagliano, M. Mutarelli, M. J. Ziller, D. Cacchiarelli, C. Romualdi, N. Elvassore *et al.*, *Nature cell biology*, 2019, **21**, 275–286.
- [81] J. Reboud, G. Xu, A. Garrett, M. Adriko, Z. Yang, E. M. Tukahebwa, C. Rowell and J. M. Cooper, *Proceedings of the National Academy of Sciences*, 2019, **116**, 4834–4842.
- [82] P. A. M. Dirac, *Mathematical Proceedings of the Cambridge Philosophical Society*, 1939, **35**, 416–418.
- [83] J. von Neumann, *Mathematical Foundations of Quantum Mechanics*, Princeton University Press, new edn, 2018.
- [84] F. Bloch, *Physical Review*, 1946, **70**, 460–474.
- [85] D. I. Hoult and R. E. Richards, *Journal of Magnetic Resonance (1969)*, 1976, **24**, 71–85.
- [86] A. Abragam, *The Principles of Nuclear Magnetism*, Oxford University Press, 1961.

- [87] P. J. M. van Bentum, J. W. G. Janssen, A. P. M. Kentgens, J. Bart and J. G. E. Gardeniers, *Journal of Magnetic Resonance*, 2007, **189**, 104–113.
- [88] H. Nyquist, *Physical review*, 1928, **32**, 110.
- [89] J. B. Johnson, *Physical review*, 1928, **32**, 97.
- [90] V. Badilita, R. C. Meier, N. Spengler, U. Wallrabe, M. Utz and J. G. Korvink, *Soft Matter*, 2012, **8**, 10583–10597.
- [91] N. Spengler, A. Moazenzadeh, R. C. Meier, V. Badilita, J. Korvink and U. Wallrabe, *Journal of Micromechanics and Microengineering*, 2014, **24**, 034004.
- [92] N. Spengler, J. Höfflin, A. Moazenzadeh, D. Mager, N. MacKinnon, V. Badilita, U. Wallrabe and J. G. Korvink, *PloS one*, 2016, **11**, e0146384.
- [93] I. Swyer, S. von der Ecken, B. Wu, A. Jenne, R. Soong, F. Vincent, D. Schmidig, T. Frei, F. Busse and H. J. Stronks, *Lab on a Chip*, 2019, **19**, 641–653.
- [94] R. C. Meier, J. Höfflin, V. Badilita, U. Wallrabe and J. G. Korvink, *Journal of Micromechanics and Microengineering*, 2014, **24**, 045021.
- [95] W. Hale, G. Rossetto, R. Greenhalgh, G. Finch and M. Utz, *Lab on a Chip*, 2018, **18**, 3018–3024.
- [96] I. Kobayashi, Y. Wada, K. Uemura and M. Nakajima, *Microfluidics and Nanofluidics*, 2010, **8**, 255–262.
- [97] J. Zhang, R. J. Coulston, S. T. Jones, J. Geng, O. A. Scherman and C. Abell, *Science*, 2012, **335**, 690–694.
- [98] J. Ju, C. Zeng, L. Zhang and N. Xu, *Chemical Engineering Journal*, 2006, **116**, 115–121.
- [99] J. Kobayashi, Y. Mori, K. Okamoto, R. Akiyama, M. Ueno, T. Kitamori and S. Kobayashi, *Science*, 2004, **304**, 1305–1308.
- [100] U. Demirci and G. Montesano, *Lab on a Chip*, 2007, **7**, 1428–1433.
- [101] L. Mazutis, J. Gilbert, W. L. Ung, D. A. Weitz, A. D. Griffiths and J. A. Heyman, *Nature protocols*, 2013, **8**, 870.
- [102] W. Shi, J. Qin, N. Ye and B. Lin, *Lab on a Chip*, 2008, **8**, 1432–1435.
- [103] F. Schuler, M. Trotter, M. Geltman, F. Schwemmer, S. Wadle, E. Domínguez-Garrido, M. López, C. Cervera-Acedo, P. Santibáñez and F. von Stetten, *Lab on a Chip*, 2016, **16**, 208–216.
- [104] S. C. Kim, I. C. Clark, P. Shahi and A. R. Abate, *Analytical Chemistry*, 2018, **90**, 1273–1279.

- [105] M. Y. Tang and H. C. Shum, *Lab on a Chip*, 2016, **16**, 4359–4365.
- [106] K. T. Kotz, Y. Gu and G. W. Faris, *Journal of the American Chemical Society*, 2005, **127**, 5736–5737.
- [107] S.-Y. Teh, R. Lin, L.-H. Hung and A. P. Lee, *Lab on a Chip*, 2008, **8**, 198–220.
- [108] M. He, J. S. Kuo and D. T. Chiu, *Applied Physics Letters*, 2005, **87**, 031916.
- [109] S.-H. Tan, N.-T. Nguyen, L. Yobas and T. G. Kang, *Journal of Micromechanics and Microengineering*, 2010, **20**, 045004.
- [110] B. Dura, M. M. Servos, R. M. Barry, H. L. Ploegh, S. K. Dougan and J. Voldman, *Proceedings of the National Academy of Sciences*, 2016, **113**, E3599–E3608.
- [111] W. Hale, G. Rossetto, R. Greenhalgh, G. Finch and M. Utz, *Lab on a Chip*, 2018.
- [112] P. Garstecki, I. Gitlin, W. DiLuzio, G. M. Whitesides, E. Kumacheva and H. A. Stone, *Applied Physics Letters*, 2004, **85**, 2649–2651.
- [113] P. Umbanhower, V. Prasad and D. A. Weitz, *Langmuir*, 2000, **16**, 347–351.
- [114] P. Zhu, T. Kong, Z. Kang, X. Tian and L. Wang, *Scientific reports*, 2015, **5**, 11102.
- [115] P. Zhu and L. Wang, *Lab on a Chip*, 2017, **17**, 34–75.
- [116] J. L. Markley, R. Brüschweiler, A. S. Edison, H. R. Eghbalnia, R. Powers, D. Raftery and D. S. Wishart, *Current opinion in biotechnology*, 2017, **43**, 34–40.
- [117] R. Powers, *Magnetic Resonance in Chemistry*, 2009, **47**, S2–S11.
- [118] V. Kasivisvanathan, A. S. Rannikko, M. Borghi, V. Panebianco, L. A. Mynderse, M. H. Vaarala, A. Briganti, L. Budäus, G. Hellawell and R. G. Hindley, *New England Journal of Medicine*, 2018, **378**, 1767–1777.
- [119] M. H. Horrocks, L. Tosatto, A. J. Dear, G. A. Garcia, M. Iljina, N. Cremades, M. Dalla Serra, T. P. Knowles, C. M. Dobson and D. Klenerman, *Analytical Chemistry*, 2015, **87**, 8818–8826.
- [120] S. Schlimpert, K. Flärdh and M. J. Buttner, *JoVE (Journal of Visualized Experiments)*, 2016, e53863.
- [121] E. A. Redman, J. S. Mellors, J. A. Starkey and J. M. Ramsey, *Analytical Chemistry*, 2016, **88**, 2220–2226.
- [122] K. Choi, E. Boyacı, J. Kim, B. Seale, L. Barrera-Arbelaez, J. Pawliszyn and A. R. Wheeler, *Journal of Chromatography A*, 2016, **1444**, 1–7.
- [123] S. S. Zalesskiy, E. Danieli, B. Blümich and V. P. Ananikov, *Chemical Reviews*, 2014, **114**, 5641–5694.

- [124] N. Spengler, J. Höfflin, A. Moazenzadeh, D. Mager, N. MacKinnon, V. Badilita, U. Wallrabe and J. G. Korvink, *Plos One*, 2016, **11**, e0146384.
- [125] P. W. Kuchel, B. E. Chapman, W. A. Bubb, P. E. Hansen, C. J. Durrant and M. P. Hertzberg, *Concepts in Magnetic Resonance Part A*, 2003, **18A**, 56–71.
- [126] C. J. Durrant, M. P. Hertzberg and P. W. Kuchel, *Concepts in Magnetic Resonance*, 2003, **18A**, 72–95.
- [127] H. Ryan, A. Smith and M. Utz, *Lab on a Chip*, 2014, **14**, 1678–1685.
- [128] J. D. Jackson, *Classical Electrodynamics*, John Wiley & Sons, 3rd edn, 2007.
- [129] M. H. Levitt, *Concepts in Magnetic Resonance*, 1996, **8**, 77–103.
- [130] J. C. Vandenenden, D. Waddington, H. Vanaalst, C. G. Vankralingen and K. J. Packer, *Journal of Colloid and Interface Science*, 1990, **140**, 105–113.
- [131] I. Fourel, J. Guillement and D. Le Botlan, *Journal of colloid and interface science*, 1994, **164**, 48–53.
- [132] K. G. Hollingsworth, A. J. Sederman, C. Buckley, L. F. Gladden and M. L. Johns, *Journal of Colloid and Interface Science*, 2004, **274**, 244–250.
- [133] J. P. Hindmarsh, J. H. Su, J. Flanagan and H. Singh, *Langmuir*, 2005, **21**, 9076–9084.
- [134] M. L. Johns, *Current Opinion in Colloid & Interface Science*, 2009, **14**, 178–183.
- [135] R. Bernewitz, G. Guthausen and H. P. Schuchmann, *Magnetic Resonance in Chemistry*, 2011, **49**, S93–S104.
- [136] I. A. Lingwood, T. C. Chandrasekera, J. Kolz, E. O. Fridjonsson and M. L. Johns, *Journal of Magnetic Resonance*, 2012, **214**, 281–288.
- [137] M. E. Fabry and R. C. San George, *Biochemistry*, 1983, **22**, 4119–4125.
- [138] A. J. Lennon, N. R. Scott, B. E. Chapman and P. W. Kuchel, *Biophysical journal*, 1994, **67**, 2096–2109.
- [139] J. A. Peters, J. Huskens and D. J. Raber, *Progress in Nuclear Magnetic Resonance Spectroscopy*, 1996, **28**, 283–350.
- [140] *CRC Handbook of Chemistry and Physics*, ed. J. Rumble, 2017, pp. 1–4.
- [141] M. C. Wapler, J. Leupold, I. Dragonu, D. von Elverfeld, M. Zaitsev and U. Wallrabe, *Journal of Magnetic Resonance*, 2014, **242**, 233–242.
- [142] C. J. G. Bakker and R. de Roos, *Magnetic Resonance in Medicine*, 2006, **56**, 1107–1113.

- [143] H. Ryan, A. Smith and M. Utz, *Lab on a Chip*, 2014, **14**, 1678–1685.
- [144] A. Yilmaz and M. Utz, *Lab on a Chip*, 2016, **16**, 2079–2085.
- [145] G. R. Finch, *PhD thesis*, University of Southampton, Southampton, 2017.
- [146] J. Bezanson, A. Edelman, S. Karpinski and V. B. Shah, *SIAM Review*, 2017, **59**, 65–98.
- [147] COMSOL Inc., *COMSOL Multiphysics®*, <https://www.comsol.com>.
- [148] Y. Takikawa, S. Ebisu and S. Nagata, *Journal of Physics and Chemistry of Solids*, 2010, **71**, 1592–1598.
- [149] J. Eills, W. Hale, M. Sharma, M. Rossetto, M. H. Levitt and M. Utz, *Journal of the American Chemical Society*, 0, **0**, null.
- [150] M. Maiwald, H. H. Fischer, Y.-K. Kim, K. Albert and H. Hasse, *Journal of Magnetic Resonance*, 2004, **166**, 135–146.
- [151] D. A. Foley, E. Bez, A. Codina, K. L. Colson, M. Fey, R. Krull, D. Piroli, M. T. Zell and B. L. Marquez, *Analytical Chemistry*, 2014, **86**, 12008–12013.
- [152] D. S. Wishart, *TrAC Trends in Analytical Chemistry*, 2008, **27**, 228–237.
- [153] M. Gottschalk, G. Ivanova, D. M. Collins, A. Eustace, R. O'Connor and D. F. Brougham, *NMR in Biomedicine*, 2008, **21**, 809–819.
- [154] M. Cuperlovic-Culf, D. A. Barnett, A. S. Culf and I. Chute, *Drug Discovery Today*, 2010, **15**, 610–621.
- [155] L. Shintu, R. Baudoin, V. Navratil, J. M. Prot, C. Pontoizeau, M. Defernez, B. J. Blaise, C. Domange, A. R. R. Péry and P. Toulhoat, *Analytical Chemistry*, 2012.
- [156] D. Olson, T. Peck, A. Webb, R. Magin and J. Sweedler, *Science*, 1995, **270**, 1967–1970.
- [157] J. Bart, A. J. Kolkman, A. J. Oosthoek-de Vries, K. Koch, P. J. Nieuwland, H. J. W. G. Janssen, P. J. M. van Bentum, K. A. M. Ampt, F. P. J. T. Rutjes, S. S. Wijmenga, H. J. G. E. Gardeniers and A. P. M. Kentgens, *Journal of the American Chemical Society*, 2009, **131**, 5014–5015.
- [158] J. Wang, G. Sui, V. P. Mocharla, R. J. Lin, M. E. Phelps, H. C. Kolb and H.-R. Tseng, *Angew. Chem.*, 2006, **118**, 5402–5407.
- [159] A. B. Theberge, E. Mayot, A. El Harrak, F. Kleinschmidt, W. T. S. Huck and A. D. Griffiths, *Lab on a Chip*, 2012, **12**, 1320–1326.
- [160] P. H. Hoang, C. T. Nguyen, J. Perumal and D.-P. Kim, *Lab on a Chip*, 2011, **11**, 329–335.

- [161] K. i. Ohno, K. Tachikawa and A. Manz, *Electrophoresis*, 2008, **29**, 4443–4453.
- [162] X. Zhou, S. Cai, A. Hong, Q. You, P. Yu, N. Sheng, O. Srivannavit, S. Muranjan, J. M. Rouillard and Y. Xia, *Nucleic acids research*, 2004, **32**, 5409–5417.
- [163] H. Fang, Y. Sun, X. Wang, M. Sharma, Z. Chen, X. Cao, M. Utz and Z. Tian, *Science China Chemistry*, 2018, **61**, 1460–1464.
- [164] P. H. Hoang, H. Park and D.-P. Kim, *Journal of the American Chemical Society*, 2011, **133**, 14765–14770.
- [165] A. Günther and K. Jensen, *Lab on a Chip*, 2006, **6**, 1487–1503.
- [166] G. M. Whitesides, *Nature*, 2006, **442**, 368–373.
- [167] J. El-Ali, P. K. Sorger and K. F. Jensen, *Nature*, 2006, **442**, 403–411.
- [168] J. West, M. Becker, S. Tombrink and A. Manz, *Analytical Chemistry*, 2008, **80**, 4403–4419.
- [169] P. Neužil, S. Giselbrecht, K. Länge, T. J. Huang and A. Manz, *Nature Reviews Drug Discovery*, 2012, **11**, 620–632.
- [170] A. D. Gracz, I. A. Williamson, K. C. Roche, M. J. Johnston, F. Wang, Y. Wang, P. J. Attayek, J. Balowski, X. F. Liu, R. J. Laurens, L. T. Gaynor, C. E. Sims, J. A. Galanko, L. Li, N. L. Allbritton and S. T. Magness, *Nature Cell Biology*, 2015, **17**, 340–349.
- [171] H. Ryan, S.-H. Song, A. Zaß, J. Korvink and M. Utz, *Analytical Chemistry*, 2012, **84**, 3696–3702.
- [172] N. Spengler, A. Moazenzadeh, R. C. Meier, V. Badilita, J. G. Korvink and U. Wallrabe, *Journal of Micromechanics and Microengineering*, 2014, **24**, 034004.
- [173] D. Rugar, C. S. Yannoni and J. Sidles, *Nature*, 1992, **360**, 563–566.
- [174] D. Rugar, R. Budakian, H. J. Mamin and B. W. Chui, *Nature*, 2004, **430**, 329–332.
- [175] H. J. Mamin, M. Poggio, C. L. Degen and D. Rugar, *Nature Nanotech*, 2007, **2**, 301–306.
- [176] M. Poggio and C. L. Degen, *Nanotechnology*, 2010, **21**, 342001.
- [177] J. R. Maze, P. L. Stanwix, J. S. Hodges, S. Hong, J. M. Taylor, P. Cappellaro, L. Jiang, M. V. G. Dutt, E. Togan, A. S. Zibrov, A. Yacoby, R. L. Walsworth and M. D. Lukin, *Nature*, 2008, **455**, 644–647.
- [178] T. Staudacher, F. Shi, S. Pezzagna, J. Meijer, J. Du, C. A. Meriles, F. Reinhard and J. Wrachtrup, *Science*, 2013, **339**, 561–563.

- [179] D. Rugar, H. J. Mamin, M. H. Sherwood, M. Kim, C. T. Rettner, K. Ohno and D. D. Awschalom, *Nature Nanotech*, 2015, **10**, 120–124.
- [180] R. McDermott, A. H. Trabesinger, M. Mück, E. L. Hahn, A. Pines and J. Clarke, *Science*, 2002, **295**, 2247–2249.
- [181] D. Budker and M. Romalis, *Nature physics*, 2007, **3**, 227.
- [182] S. Xu, V. V. Yashchuk, M. H. Donaldson, S. M. Rochester, D. Budker and A. Pines, *Proceedings of the National Academy of Sciences*, 2006, **103**, 12668–12671.
- [183] J. W. Blanchard, M. P. Ledbetter, T. Theis, M. C. Butler, D. Budker and A. Pines, *Journal of the American Chemical Society*, 2013, **135**, 3607–3612.
- [184] D. R. Glenn, D. B. Bucher, J. Lee, M. D. Lukin, H. Park and R. L. Walsworth, *Nature*, 2018, **555**, 351–354.
- [185] K. Münnemann and H. W. Spiess, *Nature Physics*, 2011, **7**, 522.
- [186] E. McDonnell, S. Han, C. Hilty, K. Pierce and A. Pines, *Analytical Chemistry*, 2005, **77**, 8109–8114.
- [187] H. Desvaux, D. J. Y. Marion, G. Huber and P. Berthault, *Angewandte Chemie International Edition*, 2009, **48**, 4341–4343.
- [188] V.-V. Telkki, V. V. Zhivonitko, S. Ahola, K. V. Kovtunov, J. Jokisaari and I. V. Koptyug, *Angewandte Chemie International Edition*, 2010, **49**, 8363–8366.
- [189] E. Paciok and B. Blümich, *Angewandte Chemie International Edition*, 2011, **50**, 5258–5260.
- [190] R. Jiménez-Martínez, D. J. Kennedy, M. Rosenbluh, E. A. Donley, S. Knappe, S. J. Seltzer, H. L. Ring, V. S. Bajaj and J. Kitching, *Nature Communications*, 2014, **5**, 3908.
- [191] A. Causier, G. Carret, C. Boutin, T. Berthelot and P. Berthault, *Lab on a Chip*, 2015, **15**, 2049–2054.
- [192] W. Hale, J. Eills, M. Rossetto, M. Levitt and M. Utz, Oral presentation, Euromar conference, Nantes, 2018.
- [193] L. Bordonali, N. Nordin, E. Fuhrer, N. MacKinnon and J. G. Korvink, *Lab on a Chip*, 2019, **19**, 503–512.
- [194] J.-B. Hövener, A. N. Pravdivtsev, B. Kidd, C. R. Bowers, S. Glöggler, K. V. Kovtunov, M. Plaumann, R. Katz-Brull, K. Buckenmaier and A. Jerschow, *Angewandte Chemie International Edition*, 2018, **57**, 11140–11162.

- [195] S. B. Duckett and R. E. Mewis, *Accounts of chemical research*, 2012, **45**, 1247–1257.
- [196] S. Glöggler, J. Colell and S. Appelt, *Journal of Magnetic Resonance*, 2013, **235**, 130–142.
- [197] R. A. Green, R. W. Adams, S. B. Duckett, R. E. Mewis, D. C. Williamson and G. G. Green, *Progress in nuclear magnetic resonance spectroscopy*, 2012, 1–48.
- [198] P. Bhattacharya, E. Y. Chekmenev, W. H. Perman, K. C. Harris, A. P. Lin, V. A. Norton, C. T. Tan, B. D. Ross and D. P. Weitekamp, *Journal of magnetic resonance*, 2007, **186**, 150–155.
- [199] E. Y. Chekmenev, J. Hövener, V. A. Norton, K. Harris, L. S. Batchelder, P. Bhattacharya, B. D. Ross and D. P. Weitekamp, *Journal of the American Chemical Society*, 2008, **130**, 4212–4213.
- [200] E. Y. Chekmenev, V. A. Norton, D. P. Weitekamp and P. Bhattacharya, *Journal of the American Chemical Society*, 2009, **131**, 3164–3165.
- [201] R. V. Shchepin, A. M. Coffey, K. W. Waddell and E. Y. Chekmenev, *Analytical Chemistry*, 2014, **86**, 5601–5605.
- [202] F. Reineri, T. Boi and S. Aime, *Nature Communications*, 2015, **6**, 5858.
- [203] E. Cavallari, C. Carrera, M. Sorge, G. Bonne, A. Muchir, S. Aime and F. Reineri, *Scientific reports*, 2018, **8**, 8366.
- [204] J. Eills, G. Stevanato, C. Bengs, S. Glöggler, S. J. Elliott, J. Alonso-Valdesueiro, G. Pileio and M. H. Levitt, *Journal of Magnetic Resonance*, 2017, **274**, 163–172.
- [205] M. Roth, P. Kindervater, H. P. Raich, J. Bargon, H. W. Spiess and K. Münnemann, *Angew. Chem.*, 2010, **122**, 8536–8540.
- [206] S. Lehmkuhl, M. Wiese, L. Schubert, M. Held, M. Küppers, M. Wessling and B. Blümich, *Journal of Magnetic Resonance*, 2018, **291**, 8–13.
- [207] P. Giraudeau, Y. Shrot and L. Frydman, *Journal of the American Chemical Society*, 2009, **131**, 13902–13903.
- [208] L. S. Lloyd, R. W. Adams, M. Bernstein, S. Coombes, S. B. Duckett, G. G. R. Green, R. J. Lewis, R. E. Mewis and C. J. Sleigh, *Journal of the American Chemical Society*, 2012, **134**, 12904–12907.
- [209] N. Eshuis, R. L. E. G. Aspers, B. J. A. van Weerdenburg, M. C. Feiters, F. P. J. T. Rutjes, S. S. Wijmenga and M. Tessari, *Angew. Chem.*, 2015, **127**, 14735–14738.
- [210] M. E. Halse, *TrAC Trends in Analytical Chemistry*, 2016, **83**, 76–83.

- [211] L. Schröder, T. J. Lowery, C. Hilty, D. E. Wemmer and A. Pines, *Science*, 2006, **314**, 446–449.
- [212] K. Golman and M. Thaning, *Proceedings of the National Academy of Sciences*, 2006, **103**, 11270–11275.
- [213] K. Ruppert, K. Qing, J. T. Patrie, T. A. Altes and J. P. Mugler III, *Academic radiology*, 2019, **26**, 355–366.
- [214] W. Zha, S. K. Nagle, R. V. Cadman, M. L. Schiebler and S. B. Fain, *Radiology*, 2018, **290**, 229–237.
- [215] Q. Chappuis, J. Milani, B. Vuichoud, A. Bornet, A. D. Gossert, G. Bodenhausen and S. Jannin, *The journal of physical chemistry letters*, 2015, **6**, 1674–1678.
- [216] Y. Kim, M. Liu and C. Hilty, *Analytical Chemistry*, 2016, **88**, 11178–11183.
- [217] H. Allouche-Arnon, A. Gamliel, C. M. Barzilay, R. Nalbandian, J. M. Gomori, M. Karlsson, M. H. Lerche and R. Katz-Brull, *Contrast media molecular imaging*, 2011, **6**, 139–147.
- [218] Y. Lee, G. S. Heo, H. Zeng, K. L. Wooley and C. Hilty, *Journal of the American Chemical Society*, 2013, **135**, 4636–4639.
- [219] M. Duewel, N. Vogel, C. K. Weiss, K. Landfester, H.-W. Spiess and K. Münnemann, *Macromolecules*, 2012, **45**, 1839–1846.
- [220] A. Bornet, M. Maucourt, C. Deborde, D. Jacob, J. Milani, B. Vuichoud, X. Ji, J.-N. Dumez, A. Moing and G. Bodenhausen, *Analytical Chemistry*, 2016, **88**, 6179–6183.
- [221] N. Zacharias, J. Lee, S. Ramachandran, S. Shanmugavelandy, J. McHenry, P. Dutta, S. Millward, S. Gammon, E. Efstatihou and P. Troncoso, *Molecular Imaging and Biology*, 2019, **21**, 86–94.
- [222] I. Romanenko, D. Gajan, R. Sayah, D. Crozet, E. Jeanneau, C. Lucas, L. Leroux, L. Veyre, A. Lesage and L. Emsley, *Angewandte Chemie International Edition*, 2015, **54**, 12937–12941.
- [223] T. Ong, W. Liao, V. Mougel, D. Gajan, A. Lesage, L. Emsley and C. Copéret, *Angewandte Chemie International Edition*, 2016, **55**, 4743–4747.
- [224] Y. Geiger, H. E. Gottlieb, U. Akbey, H. Oschkinat and G. Goobes, *Journal of the American Chemical Society*, 2016, **138**, 5561–5567.
- [225] L. Piveteau, T.-C. Ong, A. J. Rossini, L. Emsley, C. Coperet and M. V. Kovalenko, *Journal of the American Chemical Society*, 2015, **137**, 13964–13971.

- [226] Z. J. Berkson, R. J. Messinger, K. Na, Y. Seo, R. Ryoo and B. F. Chmelka, *Angewandte Chemie*, 2017, **129**, 5246–5251.
- [227] M. L. Hirsch, N. Kalechofsky, A. Belzer, M. Rosay and J. G. Kempf, *Journal of the American Chemical Society*, 2015, **137**, 8428–8434.
- [228] D. T. Peat, M. L. Hirsch, D. G. Gadian, A. J. Horsewill, J. R. Owers-Bradley and J. G. Kempf, *Physical Chemistry Chemical Physics*, 2016, **18**, 19173–19182.
- [229] G. Liu, M. Levien, N. Karschin, G. Parigi, C. Luchinat and M. Bennati, *Nature chemistry*, 2017, **9**, 676.
- [230] K. J. Pike, T. F. Kemp, H. Takahashi, R. Day, A. P. Howes, E. V. Kryukov, J. F. MacDonald, A. E. Collis, D. R. Bolton and R. J. Wylde, *Journal of Magnetic Resonance*, 2012, **215**, 1–9.
- [231] M. Sharma, G. Janssen, J. Leggett, A. Kentgens and P. van Bentum, *Journal of Magnetic Resonance*, 2015, **258**, 40–48.
- [232] J. H. Ardenkjær-Larsen, B. Fridlund, A. Gram, G. Hansson, L. Hansson, M. H. Lerche, R. Servin, M. Thaning and K. Golman, *Proceedings of the National Academy of Sciences*, 2003, **100**, 10158–10163.
- [233] D. A. Barskiy, A. M. Coffey, P. Nikolaou, D. M. Mikhaylov, B. M. Goodson, R. T. Branca, G. J. Lu, M. G. Shapiro, V.-V. Telkki, V. V. Zhivonitko *et al.*, *Chemistry—A European Journal*, 2017, **23**, 725–751.
- [234] R. A. Green, R. W. Adams, S. B. Duckett, R. E. Mewis, D. C. Williamson and G. G. Green, *Progress in Nuclear Magnetic Resonance Spectroscopy*, 2012, **67**, 1 – 48.
- [235] A. Gamliel, H. Allouche-Arnon, R. Nalbandian, C. M. Barzilay, J. M. Gomori and R. Katz-Bruhl, *Applied Magnetic Resonance*, 2010, **39**, 329–345.
- [236] B. Feng, A. M. Coffey, R. D. Colon, E. Y. Chekmenev and K. W. Waddell, *Journal of Magnetic Resonance*, 2012, **214**, 258–262.
- [237] C. R. Bowers and D. P. Weitekamp, *Journal of the American Chemical Society*, 1987, **109**, 5541–5542.
- [238] M. G. Pravica and D. P. Weitekamp, *Chemical Physics Letters*, 1988, **145**, 255–258.
- [239] R. Zhou, W. Cheng, L. M. Neal, E. W. Zhao, K. Ludden, H. E. Hagelin-Weaver and C. R. Bowers, *Physical Chemistry Chemical Physics*, 2015, **17**, 26121–26129.
- [240] E. Cavallari, C. Carrera, T. Boi, S. Aime and F. Reineri, *The Journal of Physical Chemistry B*, 2015, **119**, 10035–10041.

- [241] L. Bordonali, N. Nordin, E. Fuhrer, N. MacKinnon and J. G. Korvink, *Lab on a Chip*, 2019, **19**, 503–512.
- [242] M. Mompeán, R. M. Sánchez-Donoso, A. Hoz, V. Saggiomo, A. H. Velders and M. V. Gomez, *Nature communications*, 2018, **9**, 108.
- [243] M. Mishkovsky and L. Frydman, *ChemPhysChem*, 2008, **9**, 2340–2348.
- [244] A. S. Kiryutin, G. Sauer, D. Tietze, M. Brodrecht, S. Knecht, A. V. Yurkovskaya, K. L. Ivanov, O. Avrutina, H. Kolmar and G. Buntkowsky, *Chemistry - A European Journal*, 2019, **32**, 211–7.
- [245] M. H. Levitt, R. Freeman and T. Frenkiel, *Journal of Magnetic Resonance (1969)*, 1982, **50**, 157–160.
- [246] A. Bax and D. G. Davis, *Journal of Magnetic Resonance (1969)*, 1985, **65**, 355–360.
- [247] J. Hovener, A. N. Pravdivtsev, B. Kidd, C. R. Bowers, S. Glöggler, K. V. Kovtunov, M. Plaumann, R. Katz-Brull, K. Buckenmaier, A. Jerschow, F. Reineri, T. Theis, R. V. Shchepin, S. Wagner, N. M. M. Zacharias, P. Bhattacharya and E. Y. Chekmenev, *Angew. Chem.*, 2018.
- [248] M. Goldman, H. Johannesson, O. Axelsson and M. Karlsson, *Magn Reson Imaging*, 2005, **23**, 153–157.
- [249] M. Goldman, H. Johannesson, O. Axelsson and M. Karlsson, *Comptes Rendus Chimie*, 2006, **9**, 357–363.
- [250] B. Ripka, J. Eills, H. Kouřilová, M. Leutzsch, M. H. Levitt and K. Münnemann, *Chem. Commun.*, 2018, **54**, 12246–12249.
- [251] S. S. Roy, K. M. Appleby, E. J. Fear and S. B. Duckett, *The journal of physical chemistry letters*, 2018, **9**, 1112–1117.
- [252] F. Reineri, T. Boi and S. Aime, *Nature communications*, 2015, **6**, 5858.
- [253] S. Korchak, S. Yang, S. Mamone and S. Glöggler, *ChemistryOpen*, 2018, **7**, 344–348.
- [254] J. Liu, B. A. Williams, R. M. Gwirtz, B. J. Wold and S. Quake, *Angewandte Chemie International Edition*, 2006, **45**, 3618–3623.
- [255] S. Huang, C. Li, B. Lin and J. Qin, *Lab on a Chip*, 2010, **10**, 2925–2931.
- [256] L. Jiang, Y. Zeng, Q. Sun, Y. Sun, Z. Guo, J. Y. Qu and S. Yao, *Analytical Chemistry*, 2015, **87**, 5589–5595.
- [257] I. N. Kefala, V. E. Papadopoulos, G. Karpou, G. Kokkoris, G. Papadakis and A. Tserepi, *Microfluidics and Nanofluidics*, 2015, **19**, 1047–1059.

- [258] A. G. Hadd, D. E. Raymond, J. W. Halliwell, S. C. Jacobson and J. M. Ramsey, *Analytical Chemistry*, 1997, **69**, 3407–3412.
- [259] M. C. Mitchell, V. Spikmans and A. J. de Mello, *Analyst*, 2001, **126**, 24–27.
- [260] H. Kim, K.-I. Min, K. Inoue, D.-P. Kim and J.-i. Yoshida, *Science*, 2016, **352**, 691–694.
- [261] A.-L. Liu, Z.-Q. Li, Z.-Q. Wu and X.-H. Xia, *Talanta*, 2018, **182**, 544–548.
- [262] H. Gong, A. T. Woolley and G. P. Nordin, *Lab on a Chip*, 2016, **16**, 2450–2458.
- [263] A. K. Au, N. Bhattacharjee, L. F. Horowitz, T. C. Chang and A. Folch, *Lab on a Chip*, 2015, **15**, 1934–1941.
- [264] A. Terray, J. Oakey and D. W. Marr, *Science*, 2002, **296**, 1841–1844.
- [265] Z. Li, S. Y. Mak, A. Sauret and H. C. Shum, *Lab on a Chip*, 2014, **14**, 744–749.
- [266] T. Ward, M. Faivre, M. Abkarian and H. A. Stone, *Electrophoresis*, 2005, **26**, 3716–3724.
- [267] M. A. Unger, H.-P. Chou, T. Thorsen, A. Scherer and S. R. Quake, *Science*, 2000, **288**, 113–116.
- [268] V. Studer, G. Hang, A. Pandolfi, M. Ortiz, W. French Anderson and S. R. Quake, *Journal of applied physics*, 2004, **95**, 393–398.
- [269] C. Vicider, O. Ohman and H. Elderstig, Proceedings of the International Solid-State Sensors and Actuators Conference-TRANSDUCERS'95, pp. 284–286.
- [270] A. R. Wheeler, *Science*, 2008, **322**, 539–540.
- [271] W. Cui, M. Zhang, X. Duan, W. Pang, D. Zhang and H. Zhang, *Micromachines*, 2015, **6**, 778–789.
- [272] Y. Oda, H. Oshima, M. Nakatani and M. Hashimoto, *Electrophoresis*, 2019, **40**, 414–418.
- [273] C. H. Chen, S. H. Cho, F. Tsai, A. Erten and Y.-H. Lo, *Biomedical microdevices*, 2009, **11**, 1223.
- [274] A. Hatch, A. E. Kamholz, G. Holman, P. Yager and K. F. Bohringer, *Journal of Microelectromechanical systems*, 2001, **10**, 215–221.
- [275] J. Belardi, N. Schorr, O. Prucker and J. Rühe, *Advanced Functional Materials*, 2011, **21**, 3314–3320.
- [276] B. S. Lee, Y. U. Lee, H.-S. Kim, T.-H. Kim, J. Park, J.-G. Lee, J. Kim, H. Kim, W. G. Lee and Y.-K. Cho, *Lab on a Chip*, 2011, **11**, 70–78.

- [277] S. T. Krauss, T. P. Remcho, S. M. Lipes, R. Aranda IV, H. P. Maynard III, N. Shukla, J. Li, R. E. Tontarski Jr and J. P. Landers, *Analytical Chemistry*, 2016, **88**, 8689–8697.
- [278] B. S. Lee, J.-N. Lee, J.-M. Park, J.-G. Lee, S. Kim, Y.-K. Cho and C. Ko, *Lab on a Chip*, 2009, **9**, 1548–1555.
- [279] M. A. Unger, H.-P. Chou, T. Thorsen, A. Scherer and S. R. Quake, *Science*, 2000, **288**, 113–116.
- [280] D. C. Leslie, C. J. Easley, E. Seker, J. M. Karlinsey, M. Utz, M. R. Begley and J. P. Landers, *Nature Physics*, 2009, **5**, 231.
- [281] A. Yilmaz and M. Utz, *Lab on a Chip*, 2016, **16**, 2079–85.